Cardiac Electrophysiological Changes during High Intensity Focused Ultrasound Ablation

by

Ziqi Wu

A dissertation submitted in partial fulfillment
of the requirements for the degree of
Doctor of Philosophy
(Biomedical Engineering)
in the University of Michigan
2013

Doctoral Committee:

Professor Cheri X. Deng, Chair
Associate Professor Omer Berenfeld
Associate Professor Aman Chugh
Professor J. Brian Fowlkes
Assistant Professor Zhen Xu

To my wife and parents,
for their endless love and support

Acknowledgments

First and foremost, I would like to express my deepest gratitude to my advisor, Dr. Cheri Deng. Over the past four years at the ultrasound lab, she has been continuously supportive and her enthusiasm for my projects encouraged me to keep growing in the research field. Cheri is always patient and positive, and she has strong confidence in me especially when I encountered obstacles in my research. Cheri is not only my advisor in research, but also a great mentor in my life. I deeply appreciate the opportunity of learning from her.

I would also like to thank my dissertation committee, who provided me tremendous suggestions and help during my PhD years. I appreciate Dr. Berenfeld for providing deep insight from an electrophysiologist perspective and also for giving me my first "Langendorff" experience. I have benefitted greatly from my discussions with Dr. Chugh, who has given me valuable insight from the clinical aspect and always reminded me the significance of my research. Dr. Fowlkes will always be my idol. His broad ultrasound knowledge motivated me to keep growing. I also want to thank Dr. Xu for her consistent encouragements over past several years. Her curiosity and passion about research always keep me motivated.

I would also like to deeply thank our collaborators from Washington University at St. Louis: Dr. Igor Efimov and Dr. Jacob Laughner. Thanks for opening the door of cardiac electrophysiology for me. Without their help, I would not set up the whole "Langendorff" and optical mapping system. I

appreciate the hands-on lessons on animal surgery from Dr. Kim Ives from the Radiology lab. Also thank Dr. Robert for sharing dog hearts for my dog project and Dr. Kripfgans for allowing me use the machine room. Thanks Brady Okura for showing me the MiCAM optical mapping system.

Many thanks go to my previous labmates, for their help and most important their friendship: Drs. Yun Zhou for helping me start during my first year at U of M, Ronald Kumon for helping me on my paper, Zhenzhen Fan for her consistent mental support, Congxian Jia for helping me with the perfusion system, Juyoung Park, and Kun Yang. Special thanks go to my dear labmates and friends: Dr. Madhu, Dr. Di Chen, and Tina. I greatly appreciate the working experience with them, their willingness to help each other, whether it's research or personal lives, makes my PhD enjoyable. Without them, I will not survive those tough days. Thank the members from the histotripsy lab: Tzu-Yin, Yohan, Adam, Ryan, Kuang-Wei, Alex, Simone, Eli, Steven, and Xi for all the help. Thank my basketball team, without them, this dissertation would have come out earlier. Thank Gary Yi and Xinyang for always being supportive.

Most of all, thanks to all my family, especially my parents, Wu Jiang and Zhang Lin, who showed their unconditional love, support and encouragement over the past 26 years. Final thank goes to my dear wife, Anruo, who is the loveliest woman and also cook the best food in the world. Thank you for keeping my life full of joy.

Table of Contents

List of Figures

List of Tables

List of Abbreviations

HIFU:	High-Intensity Focused Ultrasound
EP:	Electrophysiological/Electrophysiology
AF:	Atrial Fibrillation
ECG:	Electrocardiogram
SA:	Sinoatrial
AV:	Atrioventricular
PV/PVs:	Pulmonary Veins
BPM:	Beat Per Minute
DC:	Direct Current
PVI:	Pulmonary Vein Isolation
LSPV:	Left Superior Pulmonary Vein
RSPV:	Right Superior Pulmonary Vein
LIPV:	Left Inferior Pulmonary Vein
RIPV:	Right Inferior Pulmonary Vein
SVC:	Superior Vena Cava
IVC:	Inferior Vena Cava
RFA:	Radiofrequency Ablation
RF:	Radiofrequency
FDA:	U.S. Food and Drug Administration
AEF:	Atrial Esophageal Fistula

VSD:	Voltage Sensitive Dye
UCUCA:	University Committee on the Use and Care of Animals
BDM:	2, 3-butanedione monoxime
CAD:	Computer Aided Design
FOPH:	Fiber Optic Probe Hydrophone
Isppa:	Spatial-Peak Pulse-Average Intensity
CMOS:	Complementary Metal-Oxide-Semiconductor
FPGA:	Field-Programmable Gate-Array
OAP/OAPs:	Optical Action Potential/Potentials
TTC:	Triphenyltetrazolium
MT:	Masson's Trichrome
AP:	Action Potential
APA:	Action Potential Amplitude
APD_{50}:	Action Potential at 50 % of repolarization
APD_{80}:	Action Potential at 80 % of repolarization
CV/CVs:	Conduction Velocity/Velocities
ROI:	Region of Interest
IR:	Infrared
RA:	Right Atrium
LA:	Left Atrium
RV:	Right Ventricle
LV:	Left Ventricle
AIVS:	Anterior Inter-Ventricular Sulcus
ROC:	Receiver-Operating Characteristic
AUC:	Area Under Curve

LOOCV:	Leave-one-out Cross-validation
ANOVA:	Analysis of Variance
SEM:	Standard Error of Mean
RMSE:	Root Mean Square Error
RD:	Reversible Damage
ID:	Irreversible Damage
LAD:	Lateral Anterior Descending
CFAEs:	Complex Fractionated Atrial Electrograms
RMP:	Resting Membrane Potential
MI:	Mitral Isthmus
MRI:	Magnetic Resonance Imaging
ICE:	Intracardiac Echocardiography
OCT:	Optical Coherence Tomography
ARFI:	Acoustic Radiation Force Impulse
CL:	Cycle Length
FOV:	Field of View
FIR:	Finite Impulse Response
EPI:	Epicardium
ENDO:	Endocardium
GS:	Gray-scale
IBS:	Integrated Backscatter
MLE:	Maximum Likelihood Estimates
MRF:	Markov Random Field
TPX:	Polymethylpentene
STBM:	Short Time B-mode

SEM:	Scanning Electron Microscope
TEE:	Transesophageal Echocardiography
PVC:	Premature Ventricular Contraction
STICK:	Soft Tissue Impact Characterization Kit
PVA:	Premature Ventricular Arrhythmias
DMSO:	Dimethyl Sulfoxide

Abstract

Atrial fibrillation (AF), the most common cardiac arrhythmia, is characterized by disorganized electrical activities that cause atrial quivering and uncoordinated contraction. AF significantly affects the quality of life for patients and increases the risk of stroke. Ultrasound ablation surgery has been proposed a decade ago as a treatment for AF. By focusing ultrasound energy at a narrow spot, rapid temperature rises along with tissue necrosis are generated. In this thesis, we investigated high-intensity focused ultrasound (HIFU), an ablation technology being used to eliminate arrhythmogenic foci for treatment of AF.

During HIFU ablation, little is known regarding the detailed characteristics of cellular electrophysiological (EP) changes. The first part of the thesis aims to characterize EP changes during HIFU corresponding with temperature increases. Langendorff-perfused intact rabbit heart model stained with di-4-ANEPPS, a fluorescent dye sensitive to the membrane voltage changes, was used. Simultaneous optical mapping and infrared imaging were employed to measure epicardial EP and temperature during HIFU application. The results revealed the temperature-dependent spatiotemporal characteristics of HIFU-induced EP changes including changes of action potential (AP) amplitude, duration, and electrical activation. Temperature dosage criterion for generating irreversible tissue physical and AP changes were obtained.

Intra-procedural imaging is important for guiding cardiac ablation for AF. However, it is difficult to obtain intra-procedural correlation of thermal lesion

with AP changes in tissue transmural plane. The second part is to develop parametric ultrasound imaging techniques for transmural lesion and AP detection during ablation. Perfused canine ventricular wedge was used. Simultaneous optical mapping and high frequency ultrasound imaging of the same tissue trasnsmural plane were performed during HIFU. Tissue transmural EP changes were characterized and the AP changes were spatiotemporally correlated between optical and ultrasound images. The results show that parametric ultrasound imaging using cumulative extrema of ultrasound parameters (log-normal and Rayleigh) can detect HIFU lesions and surrounding AP amplitude changes.

Overall, the information obtained from this thesis enhances our understanding of the EP mechanisms of HIFU ablation and can help promote the development of effective HIFU ablation strategies. Ultrasound parametric imaging provides a promising technique to identify lesion transmurality which is important in clinical ablations.

CHAPTER 1

Introduction

The objective of this dissertation is to investigate the thermal effect of high-intensity focused ultrasound (HIFU) in changing cellular electrophysiology (EP) of cardiac tissue. The research primarily focuses on two different aspects: characterization of EP properties and their correlations with temperature changes during HIFU ablation, and the development of imaging technology to monitor HIFU induced tissue physical and EP changes. The detailed information of EP and histopathological responses upon HIFU and the imaging feedback scheme can help improve the safety and efficacy of current HIFU techniques in clinical cardiac ablations.

1.1 Atrial Fibrillation

Atrial fibrillation (AF) is the most common sustained cardiac arrhythmia, characterized by abnormal or unsynchronized supraventricular electrical activities.[1] An estimate of 2.2 million adults in U.S. have been affected by AF, and the prevalence of AF, increasing with ages, has kept growing by 160,000 annually.[2] Patients with AF often complain of palpitations, weakness, fatigue,

chest pain, and impaired exercise tolerance. The long-term risks of stroke, heart failure and all-cause mortality increase substantially for AF patients[3].

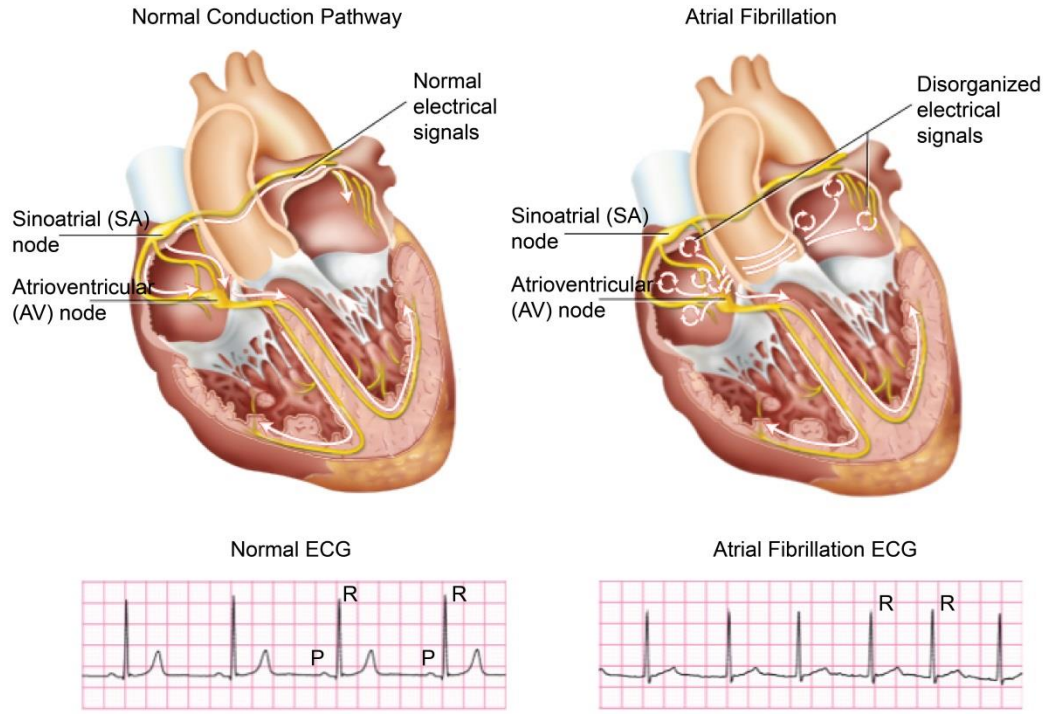

Figure 1.1 Illustration of the electrical system for a normal heart (top left) and an atrial fibrillation (AF) heart (top right). Corresponding electrocardiogram (ECG) for the normal heart (bottom left) shows regular R-R interval and apparent P waves, and for the AF heart shows irregular R-R intervals and no discernible P waves. Copyright © 2008 Atrial Fibrillation Teaching File, Department of Medicine, University of Toronto.

During normal sinus rhythm, the electrical activity (typically, 50 – 80 bpm at rest) is initiated by the sinoatrial (SA) node, the natural pacemaker in the high right atrium. This is followed by organized electrical activation across both atria, generating mechanical contraction, which propels blood into the corresponding ventricular chambers after a physiologic delay at the atrioventricular (AV) node. During AF, the electrical activity in the atria is seemingly uncoordinated with activation rates exceeding 400 bpm. Although the conduction decremented at the AV node, among other factors, prevents transmission of rapid rates into the

ventricles, the pulse rate may approach 180 bpm as compared to the normal rate of 60 – 80 bpm at rest. During AF, localized reentrant activity or rapid focal discharge are assumed to be responsible for driving the fibrillatory process.[4] And the SA node is of course overdriven by their rapid activity. Mechanically, there is no longer coordinated mechanical atrial activity, and AV synchrony is lost. This leads to diminution of cardiac output responsible for various symptoms during AF. Figure 1.1 shows the electrical sequences of a normal heart and an AF heart.

On the surface electrocardiogram (ECG) recording, AF is characterized by rapid, low-amplitude and pleomorphic "f" waves and irregular R-R intervals[5] (Figure 1.1). AF may be classified into three categories: paroxysmal AF, persistent AF, and longstanding persistent AF[6], and they are not mutually exclusive. In paroxysmal AF, multiple AF episodes occur but terminate spontaneously within less than a week, typically lasting for several hours. Persistent AF refers to AF episodes which last for more than 7 days or those require pharmacologic or electrical cardioversion. Longstanding persistent AF is defined when AF is continuous for more than one year.[7] These classifications are prognostically important in that patients with paroxysmal AF tend to have less structural remodeling and are more likely to respond to catheter ablation as opposed to patients with longstanding persistent AF who demonstrate much more structural abnormalities and are less likely to respond to ablation. In a recent worldwide survey from 9816 AF patients who had at least 1 AF episode in the last 12 months or current documented AF, with roughly 30 % of them received at least 1 admission of hospitalization and 90 % of them received antiarrhythmic drugs, 26.5 % had paroxysmal AF, 23.8 % had persistent AF, and 49.6 % had longstanding persistent AF.[8] As the burden of AF episodes increases, the risks of thrombus ("blood clot") formation also increase, leading to increased occurrence of stroke. It has been shown that the stroke incidence can increase

more than fivefold when AF is presented.[9] Epidemiology studies suggested that AF and heart failure often co-exist and the prevalence of AF in heart failure patients can exacerbate the severity of the disease.[10,11] Therefore, timely treatment of AF becomes critically important.

1.2 Treatment of Atrial Fibrillation

Generally, patients with AF can be treated through two approaches, rate control and rhythm control, depending on the severity of AF.[12] Rate control is achieved by slowing the ventricular rate to allow sufficient time for blood filling into ventricles. After rate control therapy, patients with AF suffer fewer symptoms but irregular heart rhythm still persists. The goal in rhythm control is to restore to its normal sinus rhythm, which helps restore AV synchrony and eliminate the rapid and irregular pulse rate. Rhythm control is preferable but may be challenging to achieve for various reasons. Under either approach, anticoagulant medications are recommended to prevent clot formation and reduce the risks of stroke.[13]

Heart rate control can be achieved pharmacologically or by targeted destruction of the AV node by catheter ablation.[14] The latter requires simultaneous implantation of a permanent pacemaker since AV node ablation renders the patients pacemaker dependent. Rate-controlling agents, including beta blockers, nondihydropyridine calcium channel antagonists, digoxin, and others, which prolong the refractory period of AV node, and are effective in most patients in achieving rate control.[15-17] However, bradycardia and AV block may develop in some patients.[18] When pharmacotherapy fails, AV nodal ablation combined with pacemaker implantation is an option for patients who are not

considered to be good candidates for a sinus rhythm strategy such as the elderly or those with multiple comorbidities. A meta-analysis demonstrated significant improvement of quality of life, ventricular function, exercise tolerance and reduced AF symptoms as well as healthcare for AF patients who received ablation and pacing therapy.[19] However, lifelong anticoagulation and pacemaker dependence, with its attendant complications, are important considerations.

Patients chosen for a thythm strategy are treated with antiarrhythmic medications. Pharmacotherapy has been very effective when AF lasts less than 48 hours, but with a significant decrease in conversion rate when duration of AF is beyond 48 hours.[13] Antiarrhythmic drugs such as flecainide, propafenone, sotalol, amiodarone, and dofetilide are options for daily suppressive therapy depending on the patient's clinical age and status.[20-24] However, the overall antiarrhythmic efficacy is modest.[25] The other limitation is their proclivity to prolong ventricular repolarization or slow conduction velocity, which may result in ventricular tachycardia or fibrillation, and lead to adverse clinical outcomes, including death. Amiodarone, for example, although probably the safest with respect to proarrhythmia, may result in end organ toxicity such as pulmonary fibrosis and may increase mortality rates.

Pharmacotherapy is often inadequate to achieve and maintain normal sinus rhythm especially for patients with persistent AF. Transthoracic direct-current (DC) electrical cardioversion is extremely effective in restoring sinus rhythm and allows for introduction of the aforementioned antiarrhythmic medications to decrease the likelihood of recurrence.[26] However, at one year follow-up, 63 % of patients had relapsed AF[27] which again speaks to the modest effectiveness of medical therapy for AF[28,29].

Given the limitations of medical therapy, interventional approaches were sought in an effort to more definitively eliminate AF. To this end, Cox and colleagues pioneered a surgical ablation procedure, called the Maze procedure, in the early 1990s.[30] In this procedure, a series of incisions and sutures are made at strategic locations in the atria. Simultaneously, the left atrial appendage, the major source of thromboemboli, was ligated, which was associated with a significant decrease in stroke at long-term follow up. During initial clinical practices, approximately 90 % of AF patients were rendered arrhythmia free.[31] As the technique evolved, Cox maze III procedure has become the gold-standard for patients undergoing catheter or surgical ablation of AF.[32] However, the procedure usually requires open-heart surgery, cardiopulmonary bypass, which greatly limits its widespread use in patients who otherwise may not have other indications for cardiac surgery. The invasiveness and the complexity of the cut-and-sew maze procedure has ushered the age of minimally invasive arrhythmia which attempts to mimic the clinical results of the classic procedure via small incisions or thorascopitcally. However, the results of minimally invasive arrhythmia surgery on the beating heart do not approach those of the cut-and-sew maze.[33]

1.3 Current Ablation Techniques

The invasiveness and morbidity of the surgical approach spurred the age of catheter ablation. The original catheter-based approach attempted to mimic surgical lesions place during maze procedure. This procedure, pioneered by Dr. Swartz[34], was associated with modest success rates by today's standards but was abandoned due to the relatively high rates of complications.

The development of current ablation techniques stem from better understanding of the mechanisms of the initiation and perpetuation of AF. Two major theories, multiple wavelet hypothesis and localized trigger and/or reentry hypothesis, were proposed. Moe and colleagues conceptualized AF as being due to multiple randomly meandering wavelets.[35] Clinically, paroxysmal AF has been shown to be triggered and perhaps maintained ectopic reentry in the pulmonary veins (PV) located in the posterior left atrium. Haissaguerre *et al*. showed in 1998 that these focal discharges may be eliminated by catheter ablation within the PVs, leading to improved outcomes in patients who had not responded to medical therapy.[36] The atria are connected to the PV via myocardial sleeves which are electrically disconnected during a PV isolation procedure. Histological examination of the PV-LA junction shows evidence of anisotropy which may serve as a substrate for reentry. Other triggers were proposed to be originating at ganglionic plexus and axons, vein and ligament of Marshall, and superior and inferior vena cava, and are shown in Figure 1.2.[36-40] Focal activity can generate high frequency reentrant wavelets (rotors) which further fragment into daughter rotors as they propagate across heterogeneous atrial substrates, and maintain fibrillatory atria.[41,42] To ablate these focal discharges, several currently available energy sources are illustrated and compared as following.

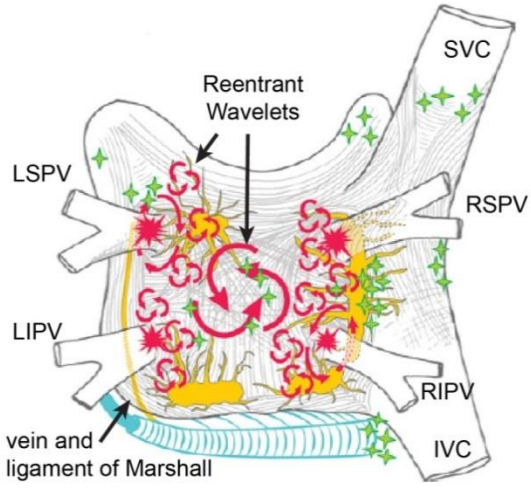

Figure 1.2 Mechanisms of initiation and perpetuation of AF. Focal foci generated from ganglionic plexus (yellow), junction of pulmonary veins and left atrium (red stars), vein of Marshall (blue), and others (green). Large and small reentrant wavelets can sustain AF. LSPV/RSPV = left/right superior pulmonary vein; LIPV/RIPV = left/right inferior pulmonary vein; SVC/IVC = superior/inferior vena cava. (Copyright © Heart Rhythm[43])

1.3.1 Radiofrequency Ablation (RFA)

Radiofrequency ablation (RFA) is achieved by applying alternating electrical current within the frequency range of 100 – 1000 kHz on myocardial tissue, which acts as a resistive medium. Tissue resistivity turns the electrical RF energy into heat, which is then absorbed by myocardial tissue and dissipated passively along the radial direction to surrounding tissue layers. When tissue temperature reaches 50 °C or higher for certain duration (usually 60 – 90 seconds for RF ablation), tissue necrosis occurs and becomes non-conductive.[44] RF energy is the first approved energy source for cardiac ablation by U.S. Food and Drug Administration (FDA). Over the past two decades, catheter-based RFA has been the cornerstone for treating different types of arrhythmias including AF. Comparing with antiarrhythmic pharmacotherapy, PVI using RFA greatly reduced the recurrence of AF and improved the quality of life of AF patients.[20] In a recent report, 79.5 % patients with paroxysmal AF restored sinus rhythm after

receiving 1 – 3 PVI using RF ablation at a 4.6 years follow up.[45] However, the success rate after PVI via RFA for patients with persistent AF remains low.[46] Significant complications were observed during RF ablation of AF including PV stenosis, thromboembolism, phrenic nerve injury, and possibly life-threatening esophagus injury.[47-51] These limitations compounded by poor monitoring ability increase the chance for procedural failure. In addition, PVI using RFA is often performed in a point-by-point ablation fashion which significantly prolongs the operation during (e.g. > 100 min)[52].

1.3.2 Cryoablation

Cryoablation is another FDA approved energy source for treating AF. During cryoablation, liquid nitrogen or compressed argon gas undergoes phase transition (liquid to gas) which significantly decreases the surrounding temperature. Typically, two different modes are performed during cryoablation: temperature ≥ – 30 °C (duration ≤ 80 seconds) for pre-ablation cryomapping and temperature ≤ – 68 °C (duration up to 4 mins) for cryoablation to generate complete irreversible tissue damage.[53] Therefore, average procedural time using cryoablation is lengthy (206 mins); however, procedural times do improve with experience.[54] Seventy three percent of the patients with paroxysmal AF were free from AF at 1-year follow up,[54] comparable to RF ablation[55]. Fewer complications were seen under cryoablation with the major complication being phrenic nerve paralysis while majority patients recovered completely 12 months after the procedure.[56] Although no atrioesophageal fistula (AEF) was observed during the early cryoablation experience[54], more recent data with the larger 28 mm balloon suggest esophageal injury and death are also possible complications of cryoballoon therapy.[57]

1.3.3 High Intensity Focused Ultrasound (HIFU)

With the unique capability of inducing intramural ablations at various depths without damaging intervening tissue, high-intensity focused ultrasound (HIFU) ablation has been widely used to treat different diseases especially for tumors (e.g. prostate cancer, breast cancer).[58,59] As high frequency acoustic wave propagate across tissue, tissue medium absorbs the acoustic energy and dissipates it as heat. Using electrical focusing or acoustical lens technique, ultrasound energy can be concentrated at a narrow spot (> 500 W/cm^2), where rapid temperature rises (up to 80 °C within seconds[60]) and tissue modifications (e.g. protein denaturation, tissue coagulation, and necrosis) are generated within confined volume without direct tissue-probe contact.

HIFU ablation has been successfully tested both *in vitro* and *in vivo* on cardiac tissue such as AV node, PVI, ventricular septum, and mitral valve.[61-64] Positive results have been reported of using HIFU energy for treating AF.[65,66] Multicenter trails involving 5 European centers reported 85 % of patients with paroxysmal AF were free from AF at six-month follow up using a HIFU balloon system for PVI.[66] Despite the initial success, the clinical application of HIFU ablation in treating AF is significantly limited due to incomplete understanding of physiological mechanism of HIFU energy deposition in the heart. Severe complications including pulmonary embolism, phrenic nerve damage, AEF, and even mortality occurred at a relatively high rate comparing to RFA and cryoablation,[67-70] leading to HIFU technology being withdrawn from the market.

Unlike RFA and cryoablation, HIFU technique in ablation of AF is relatively new. In ultrasound surgery, tissue changes are generally achieved through two different mechanisms: thermal effect mainly due to tissue

absorption (HIFU) and mechanical effect induced by acoustic cavitation (e.g. histotripsy[71]), whereas thermal effect is more desirable for ablation of AF. The development of HIFU technology mainly focused on the correlation between HIFU parameters (e.g. acoustic power, duration) and the sizes of HIFU lesions.[72,73] "Surrogate" parameters such as tissue temperature and thermal dose were also used to monitor HIFU ablation and predict lesion formation.[74,75] However, whether HIFU-induced tissue necrosis shows comparable EP changes as RF or cryoablation lesions is unknown. The relationship between HIFU lesions and regional EP property changes has not yet been characterized. The missing knowledge can be beneficial to understand the mechanisms of HIFU ablation on changing cardiac EP and to develop safer and more effective HIFU metrics for generating sustained cardiac EP changes in treating AF.

1.4 Dissertation Outline

This dissertation consists five chapters. In CHAPTER 1, an overall background of atrial fibrillation (AF), treatment methods for AF and ablation techniques including HIFU are reviewed with a brief description of the general motivation in the end. In CHAPTER 2, the technique of using optical mapping to monitor HIFU ablation in Langendorff-perfused intact rabbit heart is presented. HIFU generated cellular electrophysiological (EP) changes are qualitatively investigated. In CHAPTER 3, HIFU induced EP changes are quantitatively characterized using the methodology described in the previous chapter, and the corresponding EP changes are correlated spatiotemporally with HIFU induced tissue temperature rise. Temperature criterions for generating reversible and irreversible tissue physical and EP changes are found in the end. CHAPTER 4

presents the correlation between HIFU generated lesion and EP changes along the tissue depth direction. Ultrasound parametric imaging techniques are developed to image the HIFU lesions and surrounding irreversible action potential changes. Finally, conclusions of this work and several suggestions regarding future study are summarized in CHAPTER 5.

1.5 References

1. O'Neill MD, Jais P, Hocini M, Sacher F, Klein GJ, *et al.* Catheter ablation for atrial fibrillation. *Circulation*. 2007;116:1515-1523
2. Gillinov AM, Blackstone EH, McCarthy PM. Atrial fibrillation: Current surgical options and their assessment. *Ann Thorac Surg*. 2002;74:2210-2217
3. Waktare JE. Cardiology patient page. Atrial fibrillation. *Circulation*. 2002;106:14-16
4. Narayan SM, Krummen DE, Shivkumar K, Clopton P, Rappel WJ, Miller JM. Treatment of atrial fibrillation by the ablation of localized sources: Confirm (conventional ablation for atrial fibrillation with or without focal impulse and rotor modulation) trial. *J Am Coll Cardiol*. 2012;60:628-636
5. Camm AJ, Kirchhof P, Lip GY, Schotten U, Savelieva I, *et al.* Guidelines for the management of atrial fibrillation: The task force for the management of atrial fibrillation of the european society of cardiology (esc). *Eur Heart J*. 2010;31:2369-2429
6. Wann LS, Curtis AB, January CT, Ellenbogen KA, Lowe JE, *et al.* 2011 accf/aha/hrs focused update on the management of patients with atrial fibrillation (updating the 2006 guideline): A report of the american college of cardiology foundation/american heart association task force on practice guidelines. *Heart Rhythm*. 2011;8:157-176
7. Calkins H, Brugada J, Packer DL, Cappato R, Chen SA, *et al.* Hrs/ehra/ecas expert consensus statement on catheter and surgical ablation of atrial fibrillation: Recommendations for personnel, policy, procedures and follow-

up. A report of the heart rhythm society (hrs) task force on catheter and surgical ablation of atrial fibrillation. *Heart Rhythm*. 2007;4:816-861

8. Chiang CE, Naditch-Brule L, Murin J, Goethals M, Inoue H, *et al.* Distribution and risk profile of paroxysmal, persistent, and permanent atrial fibrillation in routine clinical practice: Insight from the real-life global survey evaluating patients with atrial fibrillation international registry. *Circ Arrhythm Electrophysiol*. 2012;5:632-639

9. Wolf PA, Abbott RD, Kannel WB. Atrial fibrillation as an independent risk factor for stroke: The framingham study. *Stroke*. 1991;22:983-988

10. Anter E, Jessup M, Callans DJ. Atrial fibrillation and heart failure: Treatment considerations for a dual epidemic. *Circulation*. 2009;119:2516-2525

11. Maisel WH, Stevenson LW. Atrial fibrillation in heart failure: Epidemiology, pathophysiology, and rationale for therapy. *Am J Cardiol*. 2003;91:2D-8D

12. Gutierrez C, Blanchard DG. Atrial fibrillation: Diagnosis and treatment. *Am Fam Physician*. 2011;83:61-68

13. Wyse DG, Waldo AL, DiMarco JP, Domanski MJ, Rosenberg Y, *et al.* A comparison of rate control and rhythm control in patients with atrial fibrillation. *N Engl J Med*. 2002;347:1825-1833

14. Levy S, Breithardt G, Campbell RW, Camm AJ, Daubert JC, *et al.* Atrial fibrillation: Current knowledge and recommendations for management. Working group on arrhythmias of the european society of cardiology. *Eur Heart J*. 1998;19:1294-1320

15. Roberts SA, Diaz C, Nolan PE, Salerno DM, Stapczynski JS, *et al.* Effectiveness and costs of digoxin treatment for atrial fibrillation and flutter. *Am J Cardiol*. 1993;72:567-573

16. Olshansky B, Rosenfeld LE, Warner AL, Solomon AJ, O'Neill G, *et al.* The atrial fibrillation follow-up investigation of rhythm management (affirm) study: Approaches to control rate in atrial fibrillation. *J Am Coll Cardiol*. 2004;43:1201-1208

17. Weerasooriya R, Davis M, Powell A, Szili-Torok T, Shah C, *et al.* The australian intervention randomized control of rate in atrial fibrillation trial (aircraft). *J Am Coll Cardiol*. 2003;41:1697-1702

18. Fuster V, Ryden LE, Cannom DS, Crijns HJ, Curtis AB, *et al.* 2011 accf/aha/hrs focused updates incorporated into the acc/aha/esc 2006 guidelines for the management of patients with atrial fibrillation: A report of the american college of cardiology foundation/american heart association task force on practice guidelines. *Circulation*. 2011;123:e269-367

19. Wood MA, Brown-Mahoney C, Kay GN, Ellenbogen KA. Clinical outcomes after ablation and pacing therapy for atrial fibrillation : A meta-analysis. *Circulation*. 2000;101:1138-1144

20. Wazni OM, Marrouche NF, Martin DO, Verma A, Bhargava M, *et al.* Radiofrequency ablation vs antiarrhythmic drugs as first-line treatment of symptomatic atrial fibrillation: A randomized trial. *JAMA*. 2005;293:2634-2640

21. Aliot E, Denjoy I. Comparison of the safety and efficacy of flecainide versus propafenone in hospital out-patients with symptomatic paroxysmal atrial fibrillation/flutter. The flecainide af french study group. *Am J Cardiol*. 1996;77:66A-71A

22. Reimold SC, Cantillon CO, Friedman PL, Antman EM. Propafenone versus sotalol for suppression of recurrent symptomatic atrial fibrillation. *Am J Cardiol*. 1993;71:558-563

23. Roy D, Pratt CM, Torp-Pedersen C, Wyse DG, Toft E, *et al.* Vernakalant hydrochloride for rapid conversion of atrial fibrillation: A phase 3, randomized, placebo-controlled trial. *Circulation*. 2008;117:1518-1525

24. Arya A, Silberbauer J, Teichman SL, Milner P, Sulke N, Camm AJ. A preliminary assessment of the effects of ati-2042 in subjects with paroxysmal atrial fibrillation using implanted pacemaker methodology. *Europace*. 2009;11:458-464

25. Zimetbaum P. Antiarrhythmic drug therapy for atrial fibrillation. *Circulation*. 2012;125:381-389

26. Lown B. Electrical reversion of cardiac arrhythmias. *Br Heart J*. 1967;29:469-489

27. Levy S, Lauribe P, Dolla E, Kou W, Kadish A, *et al.* A randomized comparison of external and internal cardioversion of chronic atrial fibrillation. *Circulation*. 1992;86:1415-1420

28. Bjerkelund CJ, Orning OM. The efficacy of anticoagulant therapy in preventing embolism related to d.C. Electrical conversion of atrial fibrillation. *Am J Cardiol*. 1969;23:208-216

29. Arnold AZ, Mick MJ, Mazurek RP, Loop FD, Trohman RG. Role of prophylactic anticoagulation for direct current cardioversion in patients with atrial fibrillation or atrial flutter. *J Am Coll Cardiol*. 1992;19:851-855

30. Cox JL, Schuessler RB, D'Agostino HJ, Jr., Stone CM, Chang BC, *et al.* The surgical treatment of atrial fibrillation. Iii. Development of a definitive surgical procedure. *J Thorac Cardiovasc Surg*. 1991;101:569-583

31. Cox JL, Schuessler RB, Lappas DG, Boineau JP. An 8 1/2-year clinical experience with surgery for atrial fibrillation. *Ann Surg*. 1996;224:267-273; discussion 273-265

32. Prasad SM, Maniar HS, Camillo CJ, Schuessler RB, Boineau JP, *et al.* The cox maze iii procedure for atrial fibrillation: Long-term efficacy in patients undergoing lone versus concomitant procedures. *J Thorac Cardiovasc Surg*. 2003;126:1822-1828

33. Stulak JM, Sundt TM, 3rd, Dearani JA, Daly RC, Orsulak TA, Schaff HV. Ten-year experience with the cox-maze procedure for atrial fibrillation: How do we define success? *Ann Thorac Surg*. 2007;83:1319-1324

34. Swartz JF, Pellersels G, J S. A catheter-based curative approach to atrial fibrillation in humans. *Circulation*. 1993;88:I-335

35. Moe GK, Abildskov JA. Atrial fibrillation as a self-sustaining arrhythmia independent of focal discharge. *Am Heart J*. 1959;58:59-70

36. Haissaguerre M, Jais P, Shah DC, Takahashi A, Hocini M, *et al.* Spontaneous initiation of atrial fibrillation by ectopic beats originating in the pulmonary veins. *N Engl J Med*. 1998;339:659-666

37. Pappone C, Santinelli V. Atrial fibrillation ablation: State of the art. *Am J Cardiol*. 2005;96:59L-64L

38. Hwang C, Wu TJ, Doshi RN, Peter CT, Chen PS. Vein of marshall cannulation for the analysis of electrical activity in patients with focal atrial fibrillation. *Circulation*. 2000;101:1503-1505

39. Tsai CF, Tai CT, Hsieh MH, Lin WS, Yu WC, *et al.* Initiation of atrial fibrillation by ectopic beats originating from the superior vena cava:

Electrophysiological characteristics and results of radiofrequency ablation. *Circulation*. 2000;102:67-74

40. Cosio FG, Lopez-Gil M, Goicolea A, Arribas F, Barroso JL. Radiofrequency ablation of the inferior vena cava-tricuspid valve isthmus in common atrial flutter. *Am J Cardiol*. 1993;71:705-709

41. Jalife J, Berenfeld O, Mansour M. Mother rotors and fibrillatory conduction: A mechanism of atrial fibrillation. *Cardiovasc Res*. 2002;54:204-216

42. Berenfeld O, Mandapati R, Dixit S, Skanes AC, Chen J, *et al.* Spatially distributed dominant excitation frequencies reveal hidden organization in atrial fibrillation in the langendorff-perfused sheep heart. *J Cardiovasc Electrophysiol*. 2000;11:869-879

43. Calkins H, Kuck KH, Cappato R, Brugada J, Camm AJ, *et al.* 2012 hrs/ehra/ecas expert consensus statement on catheter and surgical ablation of atrial fibrillation: Recommendations for patient selection, procedural techniques, patient management and follow-up, definitions, endpoints, and research trial design. *Heart Rhythm*. 2012;9:632-696 e621

44. Haines DE. Biophysics and pathophysiology of lesion formation by transcatheter radiofrequency ablation. *Catheter ablation of cardiac arrhythmias*. Blackwell Publishing Ltd; 2008:20-34.

45. Ouyang F, Tilz R, Chun J, Schmidt B, Wissner E, *et al.* Long-term results of catheter ablation in paroxysmal atrial fibrillation: Lessons from a 5-year follow-up. *Circulation*. 2010;122:2368-2377

46. Oral H, Knight BP, Tada H, Ozaydin M, Chugh A, *et al.* Pulmonary vein isolation for paroxysmal and persistent atrial fibrillation. *Circulation*. 2002;105:1077-1081

47. Sacher F, Monahan KH, Thomas SP, Davidson N, Adragao P, *et al.* Phrenic nerve injury after atrial fibrillation catheter ablation: Characterization and outcome in a multicenter study. *J Am Coll Cardiol*. 2006;47:2498-2503

48. Sanchez-Quintana D, Cabrera JA, Climent V, Farre J, Mendonca MC, Ho SY. Anatomic relations between the esophagus and left atrium and relevance for ablation of atrial fibrillation. *Circulation*. 2005;112:1400-1405

49. Saad EB, Rossillo A, Saad CP, Martin DO, Bhargava M, *et al.* Pulmonary vein stenosis after radiofrequency ablation of atrial fibrillation: Functional

characterization, evolution, and influence of the ablation strategy. *Circulation*. 2003;108:3102-3107

50. Khairy P, Chauvet P, Lehmann J, Lambert J, Macle L, *et al.* Lower incidence of thrombus formation with cryoenergy versus radiofrequency catheter ablation. *Circulation*. 2003;107:2045-2050

51. Oral H, Chugh A, Ozaydin M, Good E, Fortino J, *et al.* Risk of thromboembolic events after percutaneous left atrial radiofrequency ablation of atrial fibrillation. *Circulation*. 2006;114:759-765

52. Pappone C, Rosanio S, Oreto G, Tocchi M, Gugliotta F, *et al.* Circumferential radiofrequency ablation of pulmonary vein ostia: A new anatomic approach for curing atrial fibrillation. *Circulation*. 2000;102:2619-2628

53. Friedman PL, Dubuc M, Green MS, Jackman WM, Keane DT, *et al.* Catheter cryoablation of supraventricular tachycardia: Results of the multicenter prospective "frosty" trial. *Heart Rhythm*. 2004;1:129-138

54. Andrade JG, Khairy P, Guerra PG, Deyell MW, Rivard L, *et al.* Efficacy and safety of cryoballoon ablation for atrial fibrillation: A systematic review of published studies. *Heart Rhythm*. 2011;8:1444-1451

55. Kuhne M, Suter Y, Altmann D, Ammann P, Schaer B, *et al.* Cryoballoon versus radiofrequency catheter ablation of paroxysmal atrial fibrillation: Biomarkers of myocardial injury, recurrence rates, and pulmonary vein reconnection patterns. *Heart Rhythm*. 2010;7:1770-1776

56. Packer DL, Kowal RC, Wheelan KR, Irwin JM, Champagne J, *et al.* Cryoballoon ablation of pulmonary veins for paroxysmal atrial fibrillation: First results of the north american arctic front (stop af) pivotal trial. *J Am Coll Cardiol*. 2013;61:1713-1723

57. Ahmed H, Neuzil P, d'Avila A, Cha YM, Laragy M, *et al.* The esophageal effects of cryoenergy during cryoablation for atrial fibrillation. *Heart Rhythm*. 2009;6:962-969

58. Thuroff S, Chaussy C, Vallancien G, Wieland W, Kiel HJ, *et al.* High-intensity focused ultrasound and localized prostate cancer: Efficacy results from the european multicentric study. *J Endourol*. 2003;17:673-677

59. Wu F, Wang ZB, Chen WZ, Wang W, Gui Y, *et al.* Extracorporeal high intensity focused ultrasound ablation in the treatment of 1038 patients with solid carcinomas in china: An overview. *Ultrason Sonochem*. 2004;11:149-154

60. Chen L, ter Haar G, Hill CR. Influence of ablated tissue on the formation of high-intensity focused ultrasound lesions. *Ultrasound Med Biol*. 1997;23:921-931

61. Natale A, Pisano E, Shewchik J, Bash D, Fanelli R, *et al.* First human experience with pulmonary vein isolation using a through-the-balloon circumferential ultrasound ablation system for recurrent atrial fibrillation. *Circulation*. 2000;102:1879-1882

62. Strickberger SA, Tokano T, Kluiwstra JU, Morady F, Cain C. Extracardiac ablation of the canine atrioventricular junction by use of high-intensity focused ultrasound. *Circulation*. 1999;100:203-208

63. Otsuka R, Fujikura K, Abe Y, Okajima K, Pulerwitz T, *et al.* Extracardiac ablation of the left ventricular septum in beating canine hearts using high-intensity focused ultrasound. *J Am Soc Echocardiogr*. 2007;20:1400-1406

64. Otsuka R, Fujikura K, Hirata K, Pulerwitz T, Oe Y, *et al.* In vitro ablation of cardiac valves using high-intensity focused ultrasound. *Ultrasound Med Biol*. 2005;31:109-114

65. Mitnovetski S, Almeida AA, Goldstein J, Pick AW, Smith JA. Epicardial high-intensity focused ultrasound cardiac ablation for surgical treatment of atrial fibrillation. *Heart Lung Circ*. 2009;18:28-31

66. Ninet J, Roques X, Seitelberger R, Deville C, Pomar JL, *et al.* Surgical ablation of atrial fibrillation with off-pump, epicardial, high-intensity focused ultrasound: Results of a multicenter trial. *J Thorac Cardiovasc Surg*. 2005;130:803-809

67. Borchert B, Lawrenz T, Hansky B, Stellbrink C. Lethal atrioesophageal fistula after pulmonary vein isolation using high-intensity focused ultrasound (hifu). *Heart Rhythm*. 2008;5:145-148

68. Neven K, Schmidt B, Metzner A, Otomo K, Nuyens D, *et al.* Fatal end of a safety algorithm for pulmonary vein isolation with use of high-intensity focused ultrasound. *Circ Arrhythm Electrophysiol*. 2010;3:260-265

69. Neven K, Metzner A, Schmidt B, Ouyang F, Kuck KH. Two-year clinical follow-up after pulmonary vein isolation using high-intensity focused ultrasound (hifu) and an esophageal temperature-guided safety algorithm. *Heart Rhythm*. 2012;9:407-413

70. Okumura Y, Kolasa MW, Johnson SB, Bunch TJ, Henz BD, *et al.* Mechanism of tissue heating during high intensity focused ultrasound pulmonary vein isolation: Implications for atrial fibrillation ablation efficacy and phrenic nerve protection. *J Cardiovasc Electrophysiol*. 2008;19:945-951

71. Xu Z, Owens G, Gordon D, Cain C, Ludomirsky A. Noninvasive creation of an atrial septal defect by histotripsy in a canine model. *Circulation*. 2010;121:742-749

72. Fujikura K, Otsuka R, Kalisz A, Ketterling JA, Jin Z, *et al.* Effects of ultrasonic exposure parameters on myocardial lesions induced by high-intensity focused ultrasound. *J Ultrasound Med*. 2006;25:1375-1386

73. Engel DJ, Muratore R, Hirata K, Otsuka R, Fujikura K, *et al.* Myocardial lesion formation using high-intensity focused ultrasound. *J Am Soc Echocardiogr*. 2006;19:932-937

74. Rivens I, Shaw A, Civale J, Morris H. Treatment monitoring and thermometry for therapeutic focused ultrasound. *Int J Hyperthermia*. 2007;23:121-139

75. Hsiao Y-S, Kumon RE, Deng CX. Characterization of lesion formation and bubble activities during high-intensity focused ultrasound ablation using temperature-derived parameters. *Infrared Physics & Technology*. 2013;60:108-117

CHAPTER 2

Optical Mapping of Intact Heart during HIFU

In this chapter, the feasibility of using optical mapping, which has been used extensively in EP experimental laboratories, to measure EP changes during HIFU ablation in real time is tested. Since EP parameters cannot be measured in *in vitro* non-perfused tissue specimens, a Langendorff-perfused intact rabbit heart model is employed for the ablation and the detailed methodology of the heart preparation is described. A method of processing optical mapping data is standardized for the rest chapters. HIFU induced EP changes are qualitatively investigated along with tissue histopathological changes. Finally, a real-time mapping-ablation system is established and the results provide useful tissue electrophysiological information about HIFU cardiac ablation.

2.1 Overview

Cellular electrophysiological and tissue histopathological changes have been well documented for RF ablation using either microelectrodes or optical

mapping techniques.[1-4] These results provided important knowledge for understanding the mechanism of RF ablation and advanced the technology in cardiac ablation. Compare to RF technique, although the feasibility of HIFU application in cardiac ablation has been demonstrated experimentally[5-8], much work needs to be done to successfully translate the technology into clinical practice. While most researches of HIFU ablation focused on determining the correlation between lesion volumes with HIFU parameters[9,10], few studies have elucidated the HIFU thermal effects on cellular electrophysiology during and after HIFU ablation.

Optical mapping and development of fast fluorescent voltage-sensitive dyes (VSD) have significantly enriched the research in cardiac EP field. By using VSD, cellular transmembrane action potentials can be measured at high spatiotemporal resolution non-invasively which was not possible and inconvenient using conventional electrodes.[11] This advanced technique allows us to measure cardiac EP changes remotely in real time without interfering the HIFU acoustic field during HIFU ablation, therefore, providing useful methodology to study HIFU ablation. Evidences of HIFU generated cardiac EP modifications can be acquired directly and enhance our understanding about HIFU effects on cellular EP as well as help us optimize HIFU cardiac ablation.

Compare to previous HIFU studies using *in vitro* tissue, the Langendorff-perfused rabbit heart provides the physiological and EP properties more relevant to *in vivo* heart condition. For example, as most experimental studies of HIFU have been performed in degassed saline, the oxygenated Tyrode's solution in Langendorff system replicates the gaseous condition in human body. The increased gas nucleus may increase the risk of HIFU related cavitation. The constant perfusion in Langendorff system acts similar as blood cooling which

may be beneficial to study HIFU effect in *in vivo* condition. Furthermore, the EP characteristics derived from rabbit hearts can be proportionally scaled and extrapolated into human hearts.

2.2 Method

2.2.1 Langendorff-perfused Intact Rabbit Heart Preparation

Five New Zealand white rabbits (either sex, 2 – 3 kg) were used in this study according to a protocol approved by the University Committee on the Use and Care of Animals (UCUCA) at University of Michigan. The rabbits were anesthetized by intramuscular injection of ketamine (35 mg/kg) and xylanzine (5 mg/kg). Heparin (1000 Unit/kg) was administered through a marginal ear vein to prevent blood clotting and the rabbit was euthanized by bolus injection of sodium pentobarbital (100 mg/kg). Each heart was harvested by median sternotomy and rapidly transported to a Langendorff perfusion system using warm Tyrode's solution[12] (128.2 mM NaCl, 1.3 mM $CaCl_2$, 4.7 mM KCl, 1.19 mM NaH_2PO_4, 1.05 mM $MgCl_2$, 20.0 mM $NaHCO_3$, and 11.1 mM glucose). Details of solution preparation are described in APPENDIX. The isolated heart was then quickly placed in the Langendorff apparatus and peripheral tissues (e.g. thyroid, trachea) were trimmed off while the heart was retrogradely perfused with oxygenated Tyrode's solution (pH = 7.35 ± 0.05; 37 °C; 95 % O_2/5 % CO_2) via aorta at constant pressure of 60 – 80 mmHg.[13] After tissue cleaning, the heart was mounted on a tissue holder (Figure 2.1) and bathed in the same Tyrode's solution within the temperature range of 35 – 37 °C for superfusion. Excitation-contraction decoupler, 2,3-butanedione monoxime (BDM, 15 mM, Fisher

Scientific, Fair Lawn, NJ, USA) was used in both perfusion and superfusion solution to suppress motion artifacts during whole heart optical mapping due to heart contraction. To prevent motion induced by fluid streaming and maximize heart surface for optical mapping, the heart was pushed gently between two acoustic transparent (polycarbonate film) screens.

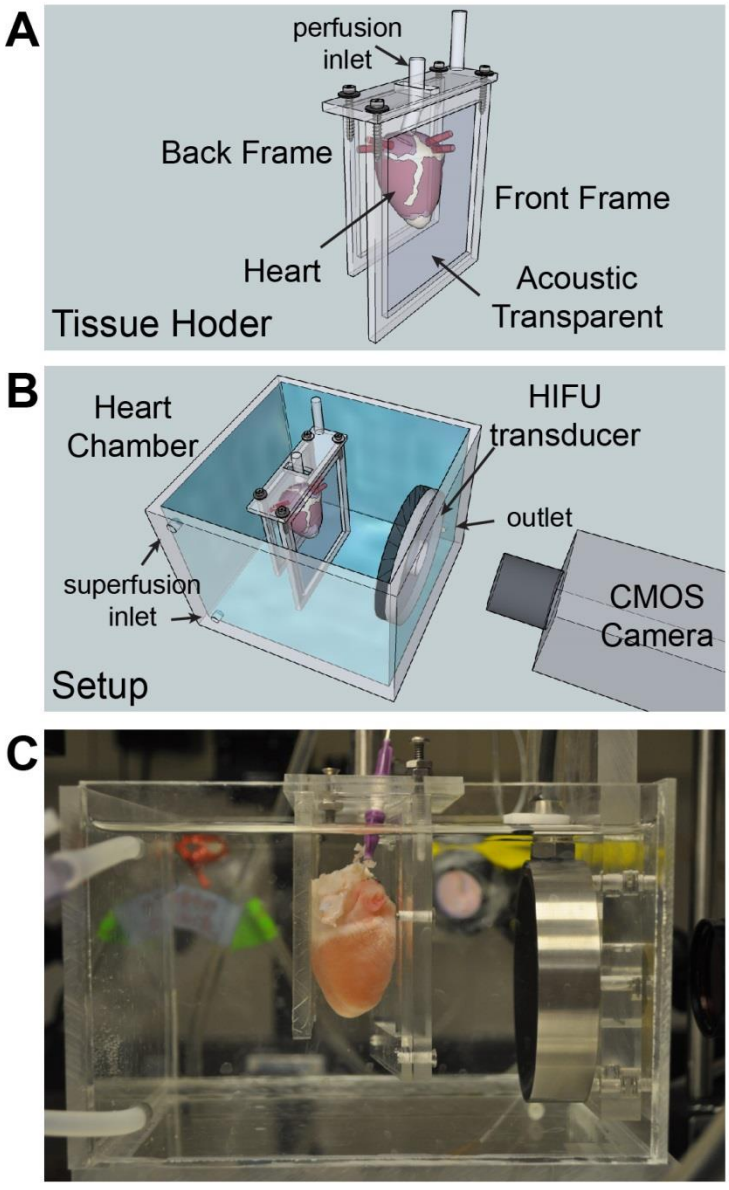

Figure 2.1 Tissue holder and experiment setup. (A) CAD of the heart holder used to stabilize the heart and reduce motion artifact. Acoustic transparent screens are

positioned in the front and the back to clamp the heart. (B) CAD of the experimental setup. Optical mapping and HIFU ablation are co-axial aligned from the same direction. The transducer is a ring shape with a round window in the center allowing simultaneous optical mapping. (C) Photograph of the experimental setup.

The electrocardiogram (ECG) was monitored via two floating needle electrodes. The ECG signals were filtered (0.5 – 50 Hz), amplified, and recorded via a digitizer (PowerLab 26T, ADInstruments, Colorado Springs, CO, USA). Aortic perfusion pressure was also monitored by a pressure transducer (BLPR2, World Precision Instruments, Sarasota, FL, USA). The ECG, aortic pressure, perfusion temperature, and pH value were monitored continuously throughout entire experimentation to ensure physiological stability of the heart. The heart typically remained healthy for 3 – 4 hours while experimentation was completed within the first 1.5 hours.

2.2.2 HIFU Ablation System

The HIFU transducer (H-148, Sonic Concepts, Bothell, WA, USA) was a ring-shaped single element transducer with a geometrical focal length of 63.2 mm, F-number of 0.98, and a center frequency of 2.0 MHz. It was fixed at the side of the superfusion tank with its focus placed at the proximal sub-epicardium of the heart. The HIFU transducer was driven by a signal generator (33250A, Agilent Technologies, Palo Alto, CA, USA) and a power amplifier (75A250, Amplifier Research, Souderton, PA, USA). Electrical power output was monitored by a power meter (PM-1, JJ&A Instruments, Duvall, WA, USA).

The acoustic field of the HIFU transducer was measured using a custom fiber optic probe hydrophone (FOPH) system with active element size of 125 μm.[14] The output of FOPH was digitized by an oscilloscope (Infiniium 54830B, Agilent Technologies, Palo Alto, CA, USA) and transferred to a PC for offline

pressure analysis. A deconvolution algorithm was employed to reduce system error. Based on the measured pressure waveforms (Figure 2.2), HIFU 6-dB beam size was confirmed to be 0.9 mm in the lateral direction and 7.2 mm in axial direction. The focal intensities (I_{sppa}: spatial-peak pulse-average) were measured between 700 and 4000 W/cm^2 with approximately 10 % uncertainty.

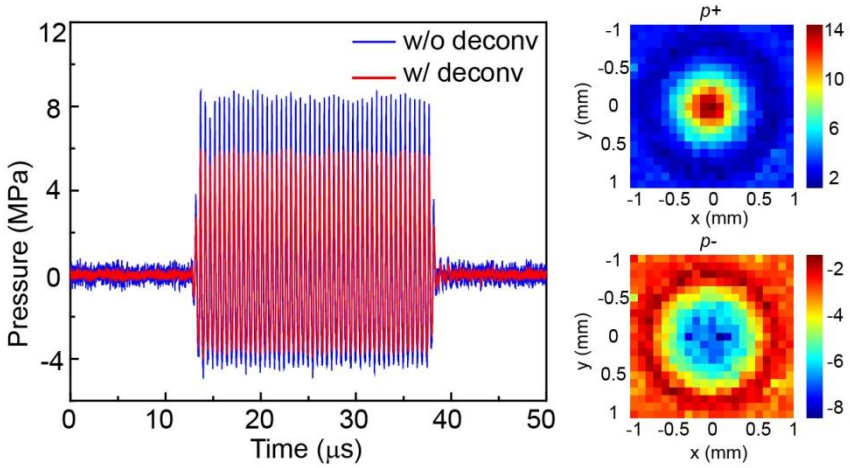

Figure 2.2 Pressure waveforms of HIFU pulses at the focus of the transducer with and without waveform deconvolution (left). Transverse two-dimensional acoustic beam of the transducer for the peak positive (top right) and peak negative (bottom right) pressure with waveform deconvolution.

2.2.3 Mapping-Ablation Procedure

Fifteen minutes after ECG signal stabilized (periodic R-wave intervals), the heart was stained with a fluorescent voltage-sensitive dye (VSD) di-4-ANEPPS (Invitrogen, Carlsbad, CA, USA) at 10 μM concentrations by bolus injection into the perfusate for 10 – 15 mins. Excitation light was generated by two green-filtered light-emitting diodes (531 ± 45 nm, 5G Illumination, SciMedia USA Ltd., Costa Mesa, CA, USA). The emitted fluorescence was long-pass

filtered (> 630 nm) and detected by a high-speed CMOS camera system (MiCAM Ultima-L, SciMedia USA Ltd., Costa Mesa, CA, USA) at a frame rate of 1000 frames/s and spatial resolution roughly 420 − 460 μm/pixel (100 × 100 pixels). Entire optical mapping was performed in a dark room.

Optical mapping was synchronized with the HIFU pulses via a custom-designed field-programmable gate-array board (FPGA) (Cyclone® II, Altera Corp., San Jose, CA, USA), which first triggered optical CMOS camera for 4 s baseline recording and followed by triggering 10 s continuous-wave HIFU exposure. To maximize the signal-noise-ratio for the optical mapping, the excitation light intensity was adjusted before data acquisition by setting the highest pixel intensity to be about 80 % of the saturation value estimated over several cardiac cycles. In order to generate lesion on a perfused heart, the intensity of the HIFU was set relatively higher at 3000 W/cm^2 (Figure 2.2) (typically > 1000 W/cm^2 for *in vitro* experiments) in a 10 s tone-burst mode. Optical mapping recorded optical action potentials (OAPs) in real time continuously for 32 s.

After each experiment, the heart was photographed and followed by triphenyltetrazolium (TTC, Sigma Aldrich, St. Louis, MO, USA) staining, where tissue necrosis was stained as white/yellow and viable tissue was stained as dark red. Details of performing TTC staining are described in APPENDIX. The TTC stained heart was photographed again and HIFU lesion area was chopped and stored in 10 % formalin for > 48 hours. The lesion section was then paraffin embedded, and sectioned with 100 μm step size across the lesion mid-line. Masson's trichrome (MT) staining was performed and the stained slides were scanned with a scanner (CanoScan 8800F, Canon USA, Inc., Melville, NY, USA) and imaged again under microscope.

2.2.4 Data Analysis of Optical Mapping Data

Optical mapping recorded signals were analyzed using customed Matlab algorithms (v. 2011b, Mathworks, Natick, MA, USA) as described in literature[15]. Spatial averaging (3 × 3) and a band-pass (0 – 100 Hz) FIR filter were applied for spatiotemporal smoothing of the VSD images. The effects of photo-bleaching were corrected via exponential fitting ($Y = b \cdot \lg(a \cdot X)$, where coefficients a and b were derived from pre-HIFU baseline values) of the VSD baseline values prior to HIFU application. Optical action potentials (OAPs) were normalized from 0 to unity and AP amplitude (APA) was defined as the value between OAPs peak and the resting potential. Activation time was identified as the corresponding times when $d(\Delta F)/dt$ reached maximum in an individual cardiac cycle, where ΔF, or the fractional fluorescence change, was the ratio between the change of fluorescence signal intensity and the background fluorescence level. Activation maps were formed from the activation time at each pixel and conduction velocities (CVs) were derived as the spatial gradient of the activation map. AP duration at 50 % and 80% of repolarization (APD_{50} and APD_{80}) were defined as the duration between activation time and 50% or 80 % peak APA value at repolarization. Changes in APA (ΔAPA), APD_{50} (ΔAPD_{50}), APD_{80} (ΔAPD_{80}), and activation times (Δactivation) were calculated by subtracting the pre-HIFU baseline values. Graphical representations of optical mapping data processing procedure are shown in Figure 2.3 and Figure 2.4.

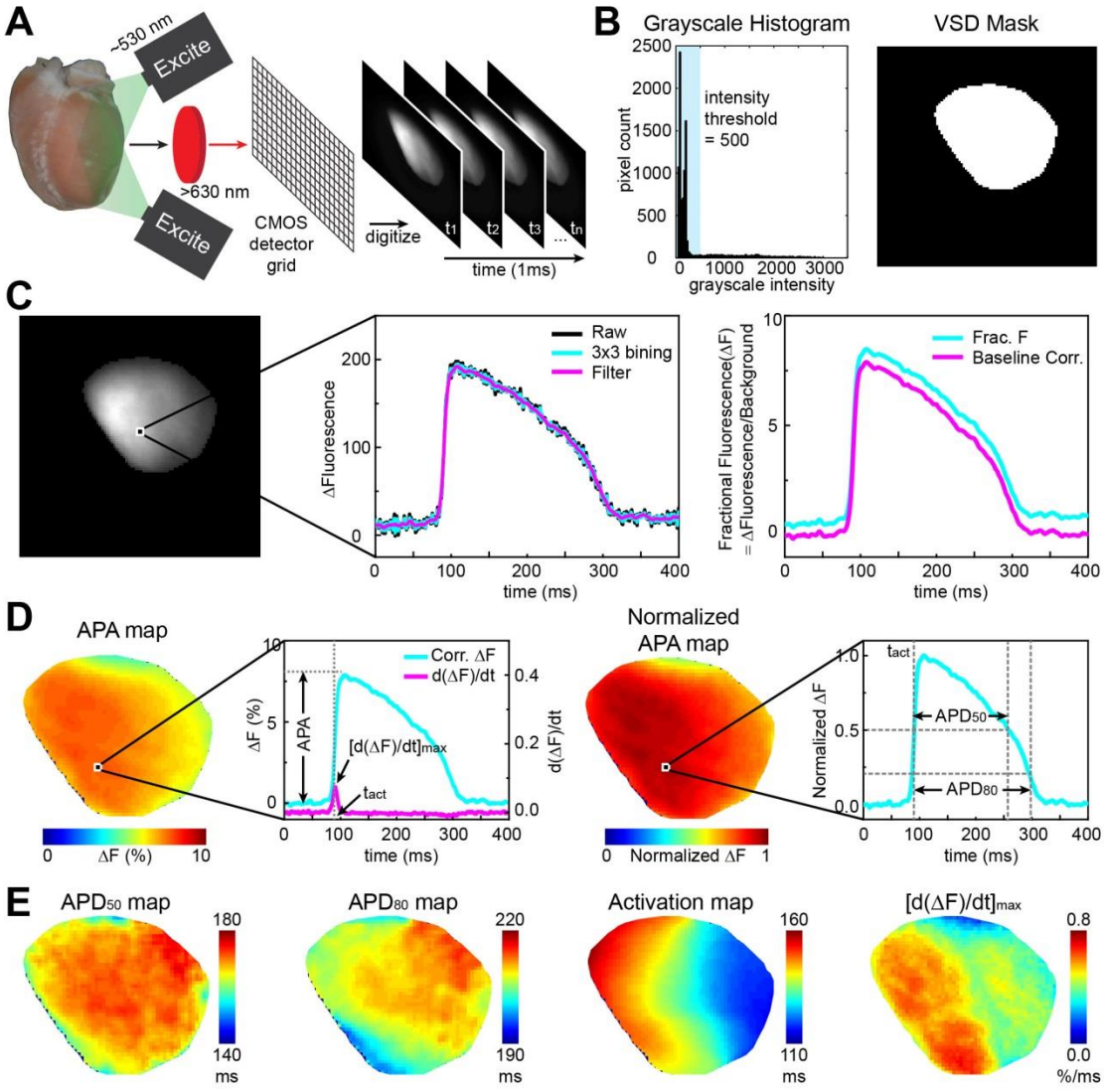

Figure 2.3 Optical mapping data processing procedure. (A) Diagram of optical mapping acquisition procedure. (B) Optical mapping images were first thresholded based on grayscale intensity and VSD mask was generated. (C) After thresholding, image was smoothed using 3 × 3 binning algorithm and filtered using FIR filter. Representative OAP at labeled pixel are shown at raw and after smoothing and filtering. OAP signal was then divided by optical mapping background image to generate fractional fluorescent signal (ΔF) and baseline offset was corrected. (D) APA map was generated from baseline corrected ΔF signal and first derivative of ΔF was calculated and the corresponding time index was the activation time and amplitude is the OAP upstroke velocity ($[d(\Delta F)/dt]_{max}$). APA map was normalized to the maximum pixel and APD_{50} and APD_{80} were found as shown. (E) Representative maps of APD_{50}, APD_{80}, activation, and upstroke velocity ($[d(\Delta F)/dt]_{max}$).

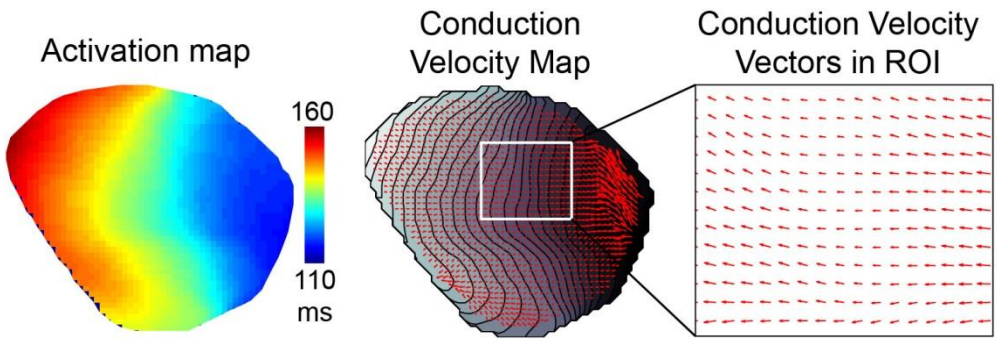

Figure 2.4 Generation of conduction velocities (CVs) map from activation map. CVs map are generated by taking the spatial gradient of activation map. The amplitude and direction of CVs are represented by the direction and length of red arrows.

2.3 Optical Mapping of HIFU Ablation

2.3.1 HIFU induced Tissue Physical Changes

During HIFU ablation, dramatic tissue histopathological changes were observed. In the ablation cases (n = 5), HIFU transducer was aligned such that its focus was placed at the epicardium of the heart. Post HIFU gross tissue examination demonstrated necrotic spot (~ 1 mm in diameter) in the epicardium with apparent discoloration (Figure 2.5). On the TTC stained images, HIFU lesions in the intact heart were clearly demarcated with a diameter covering 1.2 – 2.3 mm and maximal axial depth up to 4.2 mm for 10 s tone-burst HIFU applications.

Masson's trichrome histology further confirmed HIFU generated tissue damage. Lesion regions were stained as purple, indicating a hypereosinophilic reaction, while normal tissue was stained as pink (Figure 2.5). Clear contraction band condensation and a rim of inflammatory cells were seen at the edge of the

HIFU lesions. Within the lesions, disrupted myofibrils and cell derangements were observed while normal tissue area showed intact cell structure and tight cell-cell connections, suggesting a minimum collateral damage outside HIFU focal area.

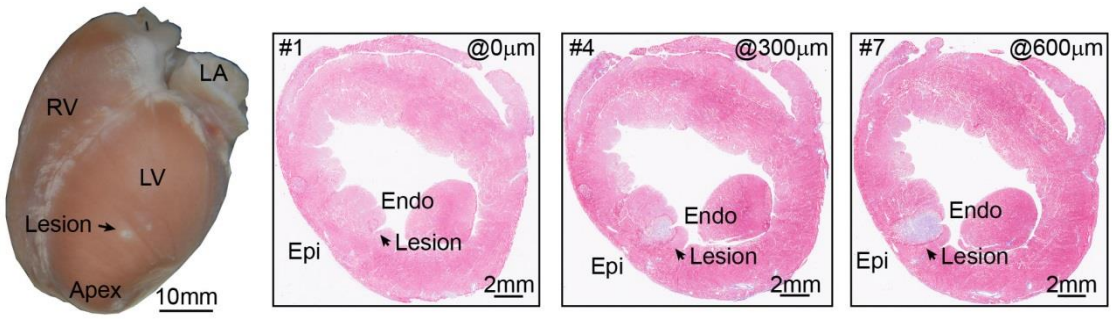

Figure 2.5 Example of gross image and masson's trichrome (MT) staining of HIFU generated lesion. Photograph of gross tissue with lesion (left) and MT slides at different cutting sections (0, 300, 600 μm) (right) are shown.

2.3.2 Effect of HIFU on Action Potential

Along with tissue physical changes, HIFU also induced significant action potential (AP) morphological changes. In the example shown in Figure 2.6, HIFU generated AP amplitude changes were up to 34 % compared to control area (< 2 %). Both APD_{50} and APD_{80} within the HIFU focus were greatly shortened by 36 % and 26 % respectively. Upstroke velocities of APs ($\Delta[d(\Delta F)/dt]_{max}$) were also reduced by up to 52 %. Area with ΔAPA and upstroke velocities reductions appears to be more localized than the areas with APD changes. APD_{50} showed severer shortening than APD_{80}, suggesting great AP triangulations which can be indicative of electrical conduction diminishment. Temporal trace of ΔAPA and upstroke velocity in the center of the lesion was irreversible after HIFU ablation.

Residual damages on APD_{50} and APD_{80} were observed after HIFU ablation and followed by gradual recoveries which were incomplete at the end of the 32 s optical recording.

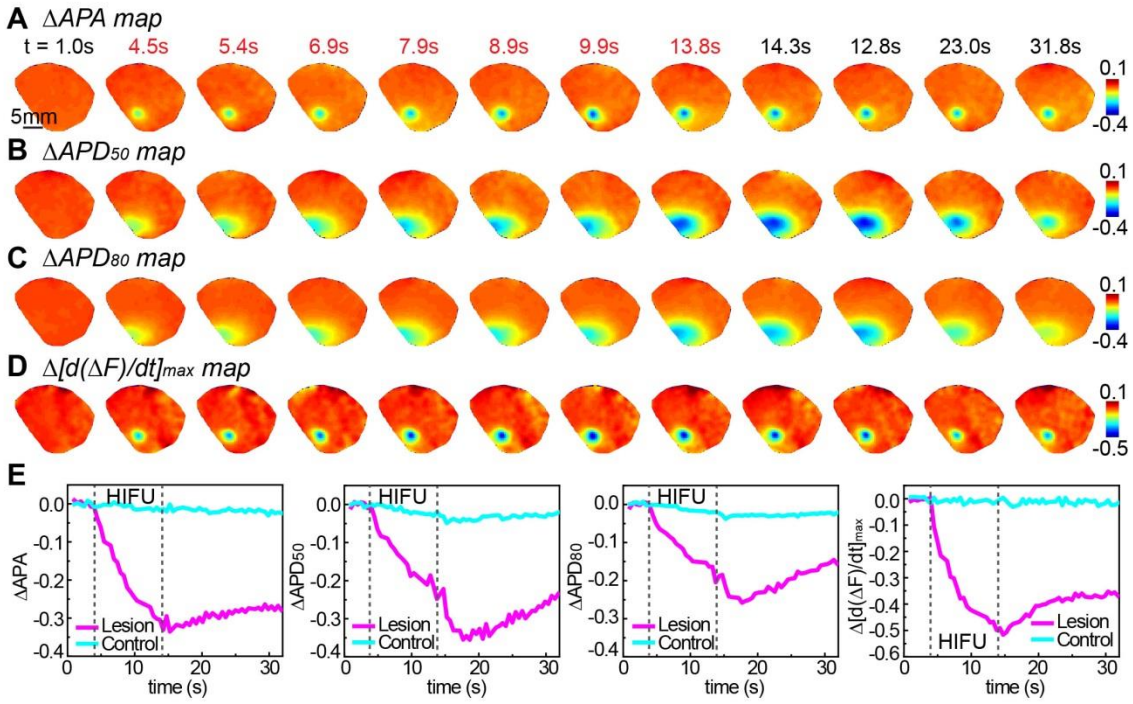

Figure 2.6 Example of HIFU induced action potential changes. Temporal development of two-dimensional (A) ΔAPA, (B) ΔAPD_{50}, (C) ΔAPD_{80}, and (D) upstroke velocity of AP ($\Delta[d(\Delta F)/dt]_{\max}$) before (< 4 s), during (4 s – 14 s), and after (15 s – 32 s) HIFU ablation. All AP parameters were normalized to pre-HIFU status. (E) Temporal traces of corresponding AP parameters within the center the HIFU lesion and in the normal tissue (control).

2.3.3 Effect of HIFU on Electrical Conduction

HIFU also generated electrical conduction changes as shown in Figure 2.7. In our experiments, all hearts were under sinus rhythm. Prior HIFU ablations, organized activation patterns across the ventricular epicardium were seen. After applying HIFU energy, distortions of activation isochrones were detected at the

HIFU focal area. As electrical wavefronts approached the HIFU lesions, significant bifurcation and clustering of isochrones occurred at the front edge of the lesions along with local activation delay within and behind lesion areas. Activation time was delayed by up to 6 ms within the lesion area. Conduction velocities (CVs) also changed dramatically around the HIFU lesions. In Figure 2.7C, after lesion formed, CVs tended to propagate around the lesion with CVs amplitudes reduction in the front edge (right side in the ROIs of Figure 2.7C) of the lesion but amplitudes increases surrounding and in the rear of the lesion (bottom left corner in the ROIs of Figure 2.7C). However, after the cessation of HIFU application, we did not see a complete conduction block when single lesion was generated. Several reasons such as smaller lesion sizes, optical "bleed-over" from adjacent pixels during recording, and electrical propagation around and under the lesion combined may cause the conduction delay being non-sustained.

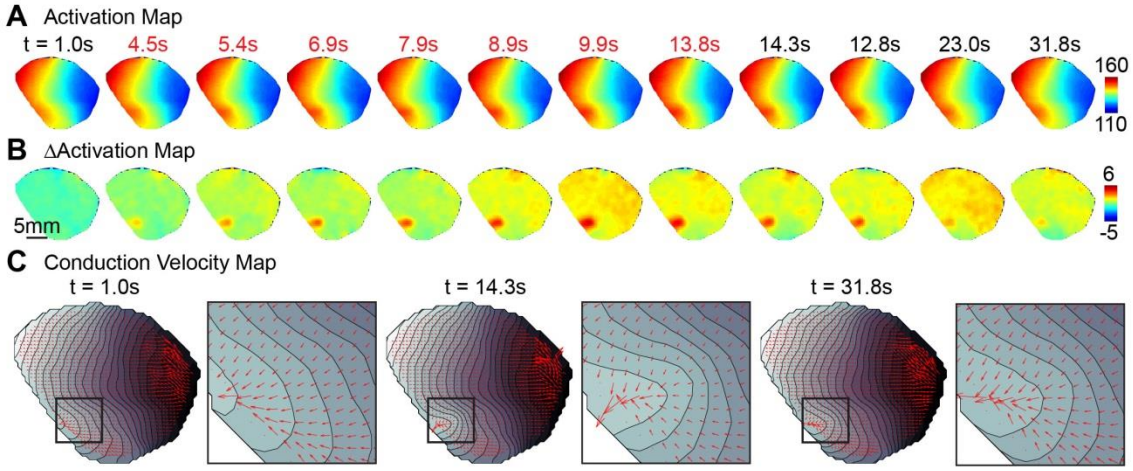

Figure 2.7 Example of HIFU generated electrical conduction changes. Two dimensional temporal changes of (A) activation time, (B) activation delay, (C) conduction velocities (CVs) changes at the same time in Figure 2.6. In the CVs maps, the amplitudes and directions of CVs are represented by the lengths and directions of the red arrows. The activation isochrones in (C) are separated by 2 ms step size.

2.4 Discussion

In this proof-of-concept study, we directly observed HIFU generated cardiac electrophysiological changes including APA reduction, APD shortening, AP upstroke velocity decrease, and distortion of activation patterns using optical mapping technique. Although optical mapping provided new methodology to study HIFU ablation, several cautions much be taken when using this technique.

The optical signal recorded at each pixel on the CMOS sensor is a weighted summation of emitted fluorescence from a volume of cells rather than a single cell. The imaging depth depends on the excitation and emission spectral properties of the fluorescent VSD. VSD has longer emission wavelength tends to provide more information about deeper tissue layers. For di-4-ANEPPS, majority of the detected signals from epicardial surface emanates from a tissue depth less than 300 μm for a rabbit heart.[16] Therefore, interpretation of the optical mapping signals needs to be done carefully, especially when HIFU generated lesions were beyond the imaging depth. It is unclear how much weight the subsurface HIFU lesion can contribute to reductions of the surface optical action potentials. Tissue absorption and photonic scattering may lead to miss interpretation about the epicardial optical mapping signals. Furthermore, the VSD used in our study has been demonstrated to cause photodynamic damage to isolated cardiomyocytes.[17] Although no significant photo-toxicity of the VSD was observed on isolated hearts, restricted excitation should be performed to reduce the risk of optical mapping related tissue damage. Another limitation of the optical mapping is cardiac repolarization related motion artifacts. It has been well noticed cardiac motion can deteriorate the optical mapping signals. In our study, excitation-contraction decoupler (BDM), which has been proved to affect the

electrophysiological property (e.g. calcium channel kinetics) of the cardiac tissue[18], was used. To avoid such side effect, a more appropriated decoupler blebbistatin, which showed no adverse effect on cellular EP[19], should be used.

2.5 References

1. Nath S, Redick JA, Whayne JG, Haines DE. Ultrastructural observations in the myocardium beyond the region of acute coagulation necrosis following radiofrequency catheter ablation. J Cardiovasc Electrophysiol. 1994;5:838-845
2. Ge YZ, Shao PZ, Goldberger J, Kadish A. Cellular electrophysiological changes induced in vitro by radiofrequency current: Comparison with electrical ablation. Pacing Clin Electrophysiol. 1995;18:323-333
3. Wu CC, Fasciano RW, 2nd, Calkins H, Tung L. Sequential change in action potential of rabbit epicardium during and following radiofrequency ablation. J Cardiovasc Electrophysiol. 1999;10:1252-1261
4. Wood MA, Fuller IA. Acute and chronic electrophysiologic changes surrounding radiofrequency lesions. J Cardiovasc Electrophysiol. 2002;13:56-61
5. He DS, Zimmer JE, Hynynen K, Marcus FI, Caruso AC, et al. Preliminary results using ultrasound energy for ablation of the ventricular myocardium in dogs. Am J Cardiol. 1994;73:1029-1031
6. He DS, Zimmer JE, Hynynen K, Marcus FI, Caruso AC, et al. Application of ultrasound energy for intracardiac ablation of arrhythmias. Eur Heart J. 1995;16:961-966
7. Lee LA, Simon C, Bove EL, Mosca RS, Ebbini ES, et al. High intensity focused ultrasound effect on cardiac tissues: Potential for clinical application. Echocardiography. 2000;17:563-566
8. Solomon SB, Nicol TL, Chan DY, Fjield T, Fried N, Kavoussi LR. Histologic evolution of high-intensity focused ultrasound in rabbit muscle. Invest Radiol. 2003;38:293-301

9. Engel DJ, Muratore R, Hirata K, Otsuka R, Fujikura K, et al. Myocardial lesion formation using high-intensity focused ultrasound. J Am Soc Echocardiogr. 2006;19:932-937

10. Fujikura K, Otsuka R, Kalisz A, Ketterling JA, Jin Z, et al. Effects of ultrasonic exposure parameters on myocardial lesions induced by high-intensity focused ultrasound. J Ultrasound Med. 2006;25:1375-1386

11. Efimov IR, Nikolski VP, Salama G. Optical imaging of the heart. Circ Res. 2004;95:21-33

12. Efimov IR, Cheng YN, Biermann M, Van Wagoner DR, Mazgalev TN, Tchou PJ. Transmembrane voltage changes produced by real and virtual electrodes during monophasic defibrillation shock delivered by an implantable electrode. J Cardiovasc Electrophysiol. 1997;8:1031-1045

13. Lou Q, Li W, Efimov IR. Multiparametric optical mapping of the langendorff-perfused rabbit heart. 2011:e3160

14. Parsons JE, Cain CA, Fowlkes JB. Cost-effective assembly of a basic fiber-optic hydrophone for measurement of high-amplitude therapeutic ultrasound fields. J Acoust Soc Am. 2006;119:1432-1440

15. Laughner JI, Ng FS, Sulkin MS, Arthur RM, Efimov IR. Processing and analysis of cardiac optical mapping data obtained with potentiometric dyes. Am J Physiol Heart Circ Physiol. 2012;303:H753-765

16. Knisley SB. Transmembrane voltage changes during unipolar stimulation of rabbit ventricle. Circ Res. 1995;77:1229-1239

17. Schaffer P, Ahammer H, Muller W, Koidl B, Windisch H. Di-4-anepps causes photodynamic damage to isolated cardiomyocytes. Pflugers Arch. 1994;426:548-551

18. Lou Q, Li W, Efimov IR. The role of dynamic instability and wavelength in arrhythmia maintenance as revealed by panoramic imaging with blebbistatin vs. 2,3-butanedione monoxime. Am J Physiol Heart Circ Physiol. 2012;302:H262-269

19. Fedorov VV, Lozinsky IT, Sosunov EA, Anyukhovsky EP, Rosen MR, et al. Application of blebbistatin as an excitation-contraction uncoupler for electrophysiologic study of rat and rabbit hearts. Heart Rhythm. 2007;4:619-626

CHAPTER 3

Electrophysiology Changes and Correlation with Temperature

In this chapter, HIFU induced cellular electrophysiological (EP) changes are correlated with corresponding temperature increases. The same Langendorff-perfused intact rabbit heart described in CHAPTER 2 was used. Simultaneous optical mapping and infrared imaging techniques were employed to measure epicardial EP and temperature during HIFU ablation. Since HIFU induced temperature changes have never been correlated with tissue EP before, the results can help us better understand the thermal effect of HIFU on cellular EP and provide thermal dosage information to guide HIFU cardiac ablation.

3.1 Overview

The technology of HIFU has been explored extensively. A number of *in vitro* studies have investigated the relationships between HIFU parameters (e.g. acoustic power, exposure time) and tissue necrosis.[1,2] Temperature and thermal dose were often used as indicators for tissue ablation.[3,4] However, these studies

have not elucidated HIFU induced cellular electrophysiological (EP) changes and their relationship with temperature increases.

Nath *et al*. first studied the temperature effects on cardiac EP properties including resting membrane potential (RMP), action potential (AP) amplitude and duration, and cellular automaticity and excitability in hyperthermia[5], and advanced the development of RF and microwave ablation. Haines further elucidated on the biophysics of RF ablation[6] and Wu *et al*. demonstrated that RF energy had both electronic and thermal effects on changing cellular EP[7]. Wood *et al*. showed the long term effect of RF ablation on cellular EP changes.[8] Whether EP changes during HIFU ablation are similar to RF ablation has not been directly confirmed. The detailed spatiotemporal information regarding cellular EP dynamics during HIFU ablation may help to improve current HIFU technique in cardiac ablation.

As demonstrated in CHAPTER 2, HIFU induced cardiac action potential (AP) changes can be optically mapped using perfused intact heart preparations. In this study, by combining infrared (IR) imaging with optical mapping, we obtained for the first time the spatiotemporal correlated measurements of temperature and EP changes during HIFU ablation in order to investigate the detailed characteristics of HIFU induced EP changes and their correlation with temperature. As electrical conduction block is often the endpoint for cardiac ablation therapy, information about cellular EP changes during HIFU ablation may help improve our understanding of the mechanisms of HIFU cardiac ablation and develop strategies to reduce the risk of electrical reconduction and recurrence of atrial fibrillation in HIFU ablation.

3.2 Methods

Isolated heart preparations are the same as described in CHAPTER 2. Eleven New Zealand white rabbits were used in this study following a protocol approved by UCUCA at University of Michigan.

3.2.1 Simultaneous Optical Mapping and Infrared Imaging

As shown in Figure 3.1, the heart preparation was placed in a custom-made holder with an acoustically transparent window (Tegaderm Film, 3M Co., St. Paul, MN, USA) of the size 4.5 × 4.5 cm^2 for ultrasound transmission from below. The heart was pinned from the apex, right, and left atrial appendages to a silicone gel pad (Sylgard 184, Dow Corning Corp., Midland, MI, USA) in the holder, which was controlled using a 3D positioning stage (EPS 300, Newport Corp., Irvine, CA, USA) for precise spatial alignment.

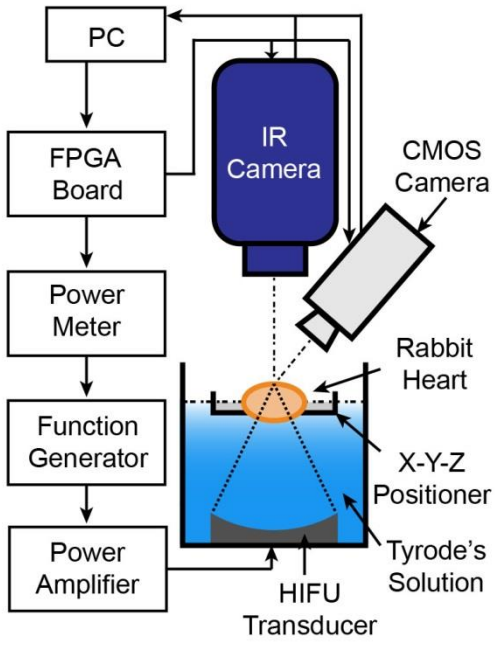

Figure 3.1 Experimental setup of simultaneous optical mapping and infrared imaging. Infrared (IR) camera for temperature imaging and high-speed fluorescence CMOS

camera for optical mapping for electrophysiology are confocally aligned focusing at the upper epicardium of the rabbit heart preparation. The HIFU transducer at the bottom of the tissue chamber is facing upwards with its focus at the upper myocardium within the field-of-view of the two cameras. The heart is mostly submersed in a Langendorff perfusion and superfusion system with only portion of the upper epicardium above the solution permitting IR imaging.

A concave single element HIFU transducer (2.0 MHz, H-148, Sonic Concepts, Inc., Bothell, WA, USA) (focal length 63.2 mm and F-number 0.95), driven by a signal generator (33250A, Agilent Technologies, Inc., Santa Clara, CA, USA) and a 75 W power amplifier (75A250, Amplifier Research, Souderton, PA, USA) was used to generate HIFU exposures with a spatial-peak pulse-average intensity (I_{sppa}) between 2300 to 2900 W/cm^2. The transducer was fixed at the bottom of the perfusion tank, facing upward with its focus placed on the epicardium of either right or left ventricle of the heart preparation through the acoustic window. A power meter (PM-1, JJ&A Instruments, Duvall, WA, USA) was used to monitor power output. The transducer has a 6-dB focal zone of 0.9 mm in lateral and 7.2 mm in axial direction measured using a custom fiber optic probe hydrophone (FOPH) system.[9]

The isolated heart was perfused and stained with di-4-ANEPPS, and mapped using the same optical mapping system demonstrated in CHAPTER 2. The upper surface of the heart preparation was elevated slightly above the solution to allow IR imaging. The IR camera (Silver SC5600, FLIR Systems, Boston, MA, USA) was confocally aligned with the CMOS camera to measure temperature in the same epicardial surface region of interest (ROI) at 50 frames/s and with a focal resolution of ~85 μm. The emissivity of the preparations was calibrated to be 0.86 prior to experiments via a black tape method[10] which used a vinyl electrical tape (Scotch Super33+, 3M Co., St. Paul, MN, USA) with a known emissivity of 0.95.

The CMOS and IR cameras were synchronized with HIFU via a custom programmed FPGA board (Cyclone® II, Altera, San Jose, CA, USA) to record optical action potentials (OAPs) and surface temperature of the isolated heart during HIFU application.

3.2.2 Experimental Procedures and Data Analysis

During experiment, the Langendorff-perfused rabbit heart was under sinus rhythm. Following equilibration for 10 – 15 mins, the excitation light was adjusted to maximize the signal-to-noise ratio. Single tone burst HIFU exposure (duration 10 s) with intensity varying from 2300 to 2900 W/cm^2 was applied to the heart preparation. After experiment, the heart was photographed (D5000, Nikon Inc., Melville, NY, USA), stained with triphenyltetrazolium (TTC, Sigma Aldrich, St. Louis, MO, USA)[11], and sectioned from mid-line of the HIFU focus for gross tissue examination. Gross tissue were then stored in 10 % formalin solution for 48 hours, paraffin embedded, and sectioned with 100 μm step size across HIFU applied region. Masson's trichrome (MT) staining was conducted on tissue sections and the stained slides were scanned at high resolution (CanoScan 8800F, Canon USA, Inc., Melville, NY, USA). HIFU-induced lesions were identified from the images.

Each pair of optical mapping image and IR image were registered with each other using a control point registration algorithm (Matlab v. 2011b, Mathworks, Natick, MA, USA), and are shown in Figure 3.2. Multiple common identifiable feature points (8 to 10) on both images were identified and a projective transformation was performed on the IR images to compensate the error induced by the angle differences between the two cameras. Optical mapping data were then processed following the method described in

CHAPTER 2. Maps of APA, APD_{50}, APD_{80}, activation, conduction velocities and their changes were generated in a similar fashion.

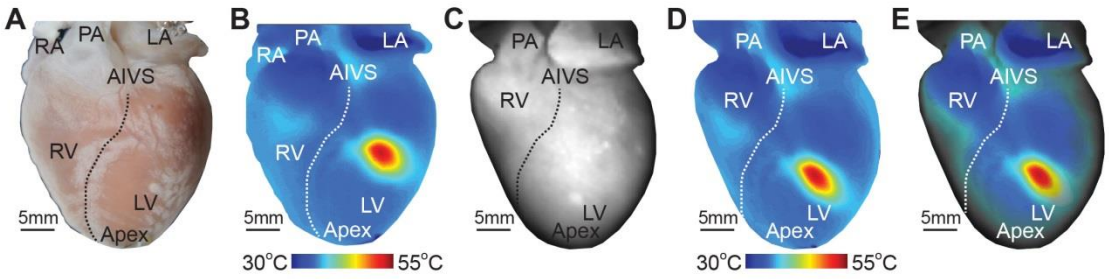

Figure 3.2 Image registration for optical mapping and infrared imaging data. (A) Photograph of a rabbit heart preparation. (B) Corresponding infrared (IR) image during HIFU ablation (t = 14 s). (C) Background image of optical mapping. (D) Projective transformed IR image from (B). (E) Overlaid image of both (C) and (D) based on physical landmarks (e.g. atrial-ventricular groove). RA = Right Atrial; LA = Left Atrial; RV = Right Ventricle; LV = Left Ventricle; AIVS = Anterior Inter-Ventricular Sulcus.

HIFU lesion was identified from TTC images of tissue specimens as positive (P) whereas non-lesion region was denoted as negative (N). Receiver-operating characteristic (ROC) analysis was performed on temperature maps at t = 14 s (HIFU was applied from 4 s – 14 s) to detect lesion formation, APA changes, and APD_{50} changes. A ROC curve was formed by comparing true positive rate (sensitivity) against false positive rate (1 – specificity) at all running thresholds and total area under curve (AUC) was calculated to assess the overall prediction performance. Optimal temperature threshold for generating lesion (lethal isotherm) was then decided to achieve the best detection accuracy. Leave-one-out cross-validation (LOOCV) was used to determine the variation of the overall ROC AUC and optimal thresholds.

Results were expressed as mean ± standard error of mean (SEM). One-way analysis-of-variance (ANOVA) (Tukey-Kramer test for multiple comparisons) and paired Student-t test was used for statistical comparisons between groups.

Statistical significance was defined as $p < 0.05$. Linear regression and F-test were used for testing linear correlation between different parameters and goodness-of-fit was assessed by the adjusted R^2 and root mean square error ($RMSE$) of the residuals.

3.3 Electrophysiology and Temperature Correlation

3.3.1 Effect of HIFU on OAPs Baseline

During HIFU ablation, IR imaging captured the spatiotemporal evolution of tissue temperature changes, and a baseline drift of OAPs (red line) were observed which was proportional to the temperature increase (Figure 3.3).

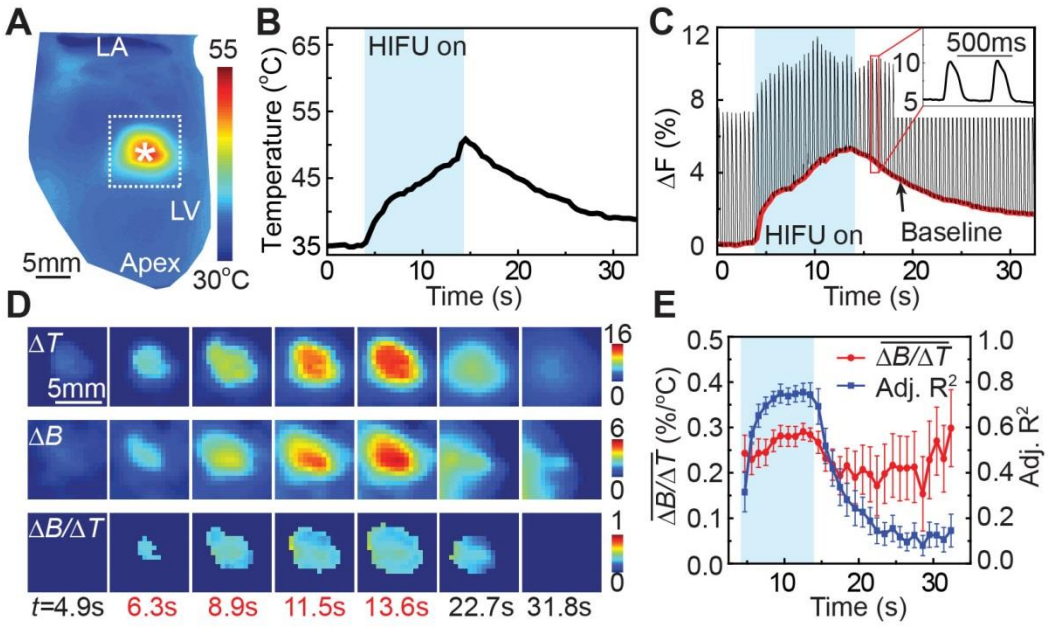

Figure 3.3 Changes of OAP baseline and temperature and their correlation. (A) Temperature map from infrared (IR) imaging at t = 14.5 s. (B) A representative temperature trace at white asterisk labeled location within HIFU focus in (A). (C) Corresponding OAPs trace at the same location in (A) with each "spikes" corresponding to single cardiac cycle. Red line highlights the baseline of fractional fluorescence signal

(Δ*F*). HIFU was on from 4 s to 14 s (blue shaded area). Inset is the zoom in for two OAPs. (D) Maps of temperature changes (Δ*T*) and corresponding OAP baseline changes (Δ*B*) in the region-of-interest (ROI) in white dashed box in (A). Ratiometric map of Δ*B*/Δ*T* at corresponding times (bottom). Red time indices represent HIFU *in situ* time. (E) Linear regression slope ($\overline{\Delta B / \Delta T}$) for paired Δ*B*-Δ*T* frames and adjusted R^2 as function of time (n = 7). HIFU *in situ* time is during blue shaded period.

The 2D maps of Δ*F* baseline (Δ*B*) in a selected ROI (17 × 17 pixels) surrounding the HIFU focus and the corresponding temperature changes (Δ*T*) appear to be spatiotemporally correlated, especially during HIFU application (4 s − 14 s). The ratiometric maps (Δ*B*/Δ*T*) (bottom row in Figure 3.3) at a given time point were fairly uniform within the ROI when Δ*T* was greater than 5 °C, indicating a linear relationship between Δ*B* and Δ*T* spatially. The linear correlation was confirmed through *F*-test and the overall linear regression slope during HIFU heating was (29.91 ± 0.09) × 10^{-2} %/°C (adj. R^2 = 0.78, 16 frames from each of the total 7 heart preparations) with a *RMSE* of 0.27 %. However, linear regressions of Δ*B* and Δ*T* at different time points showed that Δ*B*−Δ*T* correlations were not uniform throughout entire recording (Figure 3.2E). In particular, the linear regression slop increased during HIFU application, especially initially, indicating a nonlinear shift of the baseline Δ*B* with increasing Δ*T*. The correlation of Δ*B* and Δ*T* during HIFU (adj. R^2 = 0.75 ± 0.04) was also better than during cooling period (adj. R^2 < 0.5) with smaller variations during heating (< 0.03 %/°C) than during cooling (> 0.05 %/°C).

3.3.2 Mapping of EP and Temperature during HIFU Ablation

Two dimensional characteristics of cardiac EP including APA, APD, and AP triangulation (APD_{50}/APD_{80}) were demonstrated and correlated spatiotemporally with temperature changes during HIFU application, and temperature-dependent AP changes were derived in the end.

(1) Reversible EP Changes

At HIFU intensities I_{sppa} = 2300 – 2600 W/cm² and exposure duration of 10 s, no tissue necrosis was observed in the heart preparation in our experiments (n = 9). In these cases, the peak temperature reached 50.1 ± 0.8 °C (45.0 ~ 56.6 °C). During HIFU application, OAPs exhibited morphological changes including amplitude reduction and shortening of AP duration (Figure 3.4C). After cessation of HIFU, the OAP recovered to more than 95 % of the pre-HIFU level. Temperature was the highest at the center with a spatial gradient around the HIFU focus (Figure 3.4D). A slight asymmetric temperature distribution around the HIFU focus was sometimes observed, likely due to heterogeneous myocardial fiber and different orientations of microvasculature.

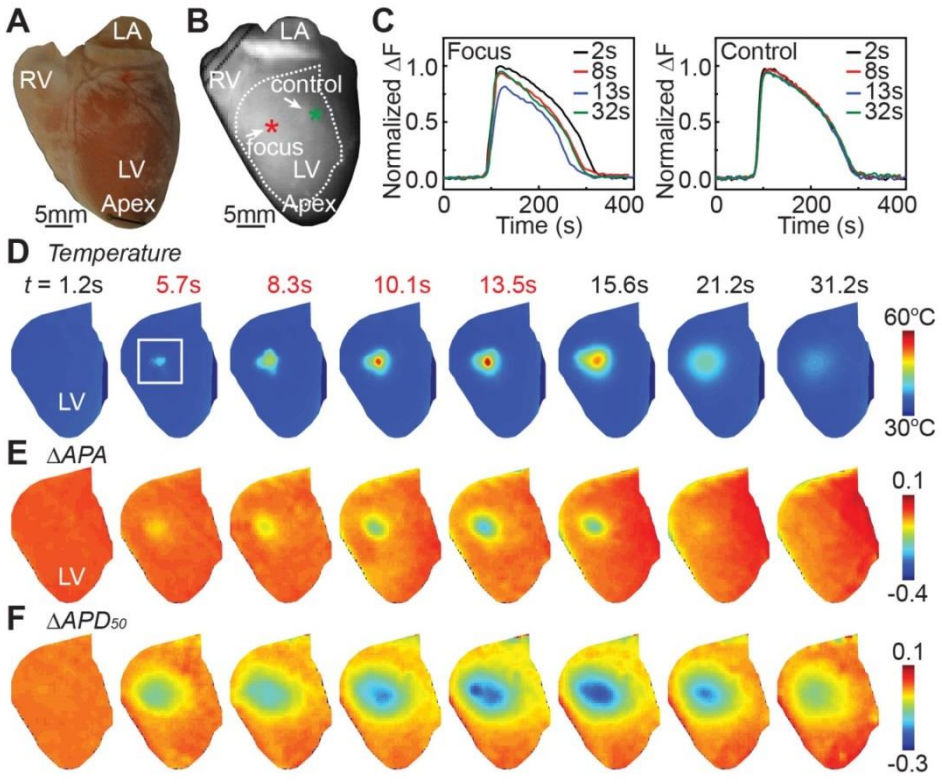

Figure 3.4 Example of a reversible ablation case. (A) Photograph of a gross heart. (B) Background image of optical mapping of the same heart with region-of-interest (ROI)

encircled by white dash line. (C) Superimposed normalized single OAPs at HIFU focus (red) and control (green) site at the color asterisks labeled location in (B) at t = 2 s, 8 s, 13 s, and 32 s. (D) Temperature maps in the ROI displayed in (B) at indicated time with red indices representing frames acquired during HIFU application. (E) Maps of APA changes (ΔAPA) in the same ROI. (F) Maps of APD_{50} changes (ΔAPD_{50}).

Corresponding with the temperature, spatially graded reductions in APA and APD_{50} were apparent around the HIFU focus (Figure 3.4E − F) with a more localized region of APA reduction. Activation isochrones were clustered when electrical wavefronts propagated across (blue to red) the HIFU focal region with activation time delayed by up to 5 ms at the HIFU focus and CV increased by up to 1.3 mm/ms (Figure 3.5). Changes in APA and activation patterns appeared to recover faster than APD_{50} after HIFU application.

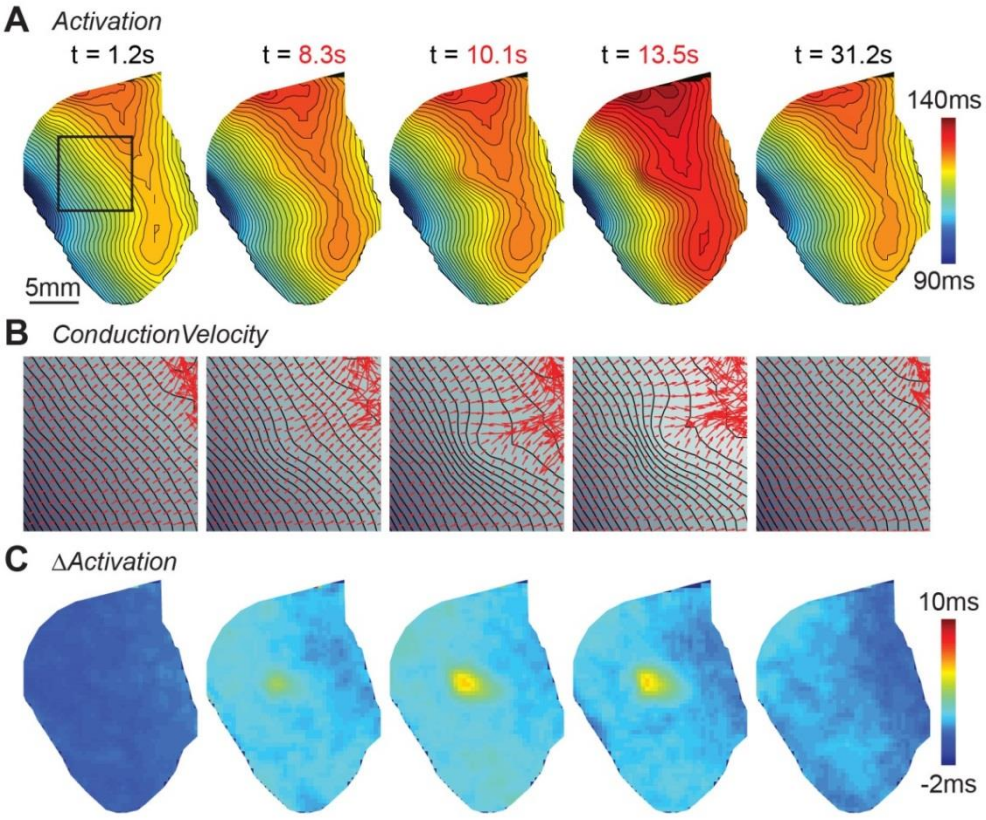

Figure 3.5 Example of activation changes for reversible case. (A) Activation map prior (1.2 s), during (8.3, 10.1, 13.5 s), and post (31.2 s) HIFU ablation for reversible damage

(RD). Isochrones are separated at 1 ms step size and blue representing early activation and red representing late activation. (B) Maps of conduction velocity (CV) within the black box labeled smaller ROI in (A). Red arrows point the direction of electrical conduction and their lengths represent corresponding magnitudes of CV. (C) Maps of activation delay derived by subtracting averaged activation maps from their pre-HIFU state (1 – 4 s).

Both APA and APD_{50} appeared to decrease nonlinearly with increasing temperature during HIFU ablation, as shown by the ratiometric maps (Figure 3.6A − B). At the beginning of HIFU heating, ΔAPA was small while ΔT was large, leading to smaller ΔAPA/ΔT values. Near the end of HIFU heating, APA decreased significantly while increase of temperature slowed down, resulting in larger ΔAPA/ΔT values. In addition, during HIFU application, APA reduction outpaced APD_{50} reduction, demonstrated by the spatial peak at the HIFU focus at t = 13.5 s (Figure 3.6C). No significant disproportional APD changes ($\Delta APD_{50}/\Delta APD_{80}$) were observed in Figure 3.6D, suggesting no significant AP triangulation in these cases with relatively small temperature increases and reversible APA and APD changes in the absence of tissue necrosis.

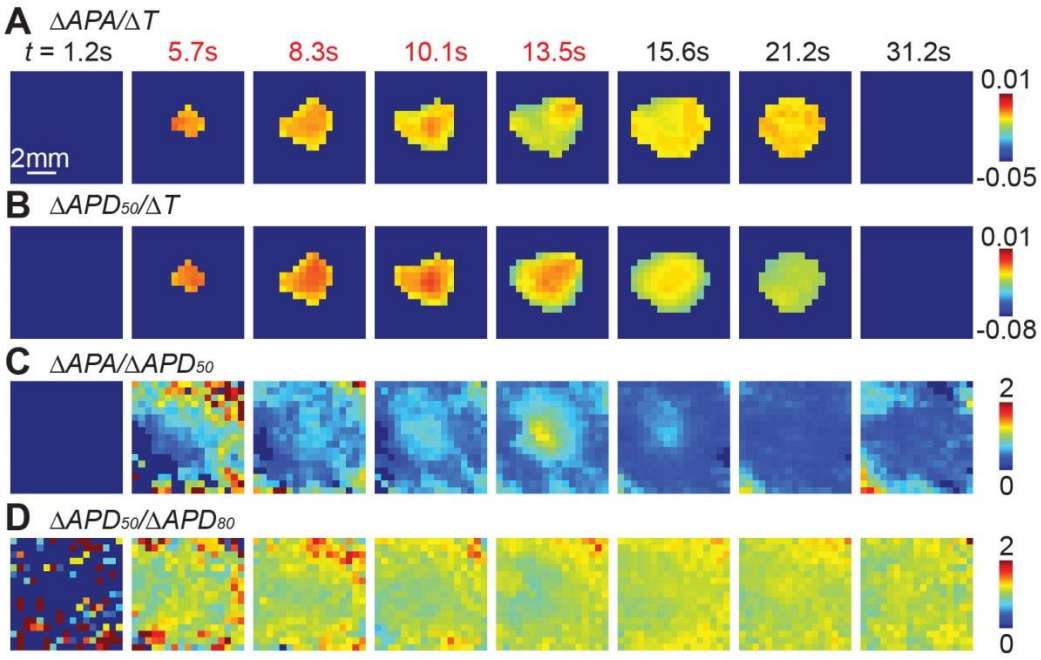

Figure 3.6 Maps of EP and temperature correlation for reversible ablation case. (A) Ratiometric maps of ΔAPA/ΔT in the smaller ROI of white box in Figure 3.4D. (B) Ratiometric maps of $\Delta APD_{50}/\Delta T$ in the same ROI. (C) Maps of $\Delta APA/\Delta APD_{50}$. (D) Maps of $\Delta APD_{50}/\Delta APD_{80}$.

(2) Irreversible EP Changes

At a higher HIFU intensity (e.g. I_{sppa} = 2900 W/cm^2), tissue necrosis or thermal lesions were generated by HIFU application. Lesions had a cross-section area of 5.95 ± 0.99 mm^2, with an axial depth of 3.55 ± 0.38 mm and lateral width of 2.10 ± 0.14 mm (n = 6). In these case, amplitude of OAPs and APD_{50} reduced by 32 % and 52 ms respectively, as shown by the OAPs at the representative locations (Figure 3.7C). Significant APD reduction (triangulation) was observed compared to the cases with reversible EP changes without tissue necrosis, indicating that plateau potentials of OAPs were significantly suppressed by HIFU ablation. After HIFU ablation at t = 31 s, OAPs amplitude recovered to only 73% of the pre-HIFU values, suggesting irreversible loss of cellular excitability.

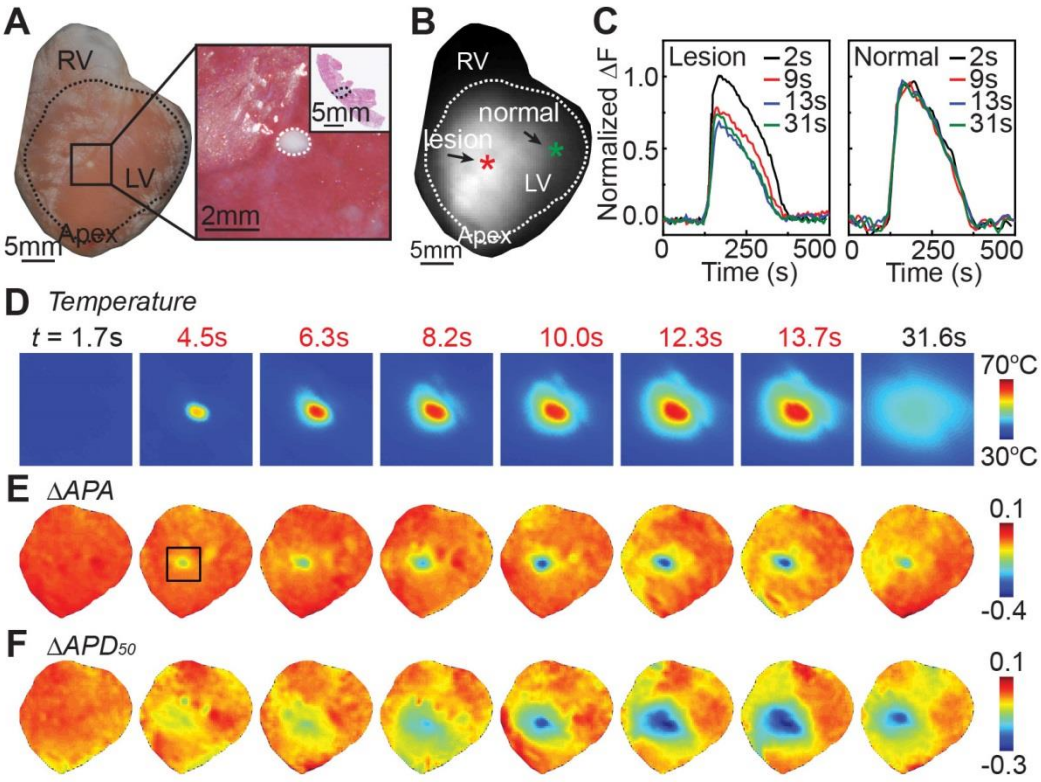

Figure 3.7 Example of an irreversible ablation case. (A) Photograph of gross heart with region-of-interest (ROI) encircled by black dash line. TTC stained tissue specimen with lesion in the middle in the smaller ROI in black box. Tissue cross-section was masson's trichrome stained with lesion highlighted by black dash line (inset). (B) Background image of optical mapping of the same heart with the same ROI in (A) encircled by black dash line. (C) Superimposed normalized single OAPs in the lesion (red) and outside (green) HIFU focus at the color asterisks labeled location in (B) at t = 2 s, 9 s, 13s , and 31 s. (D) Temperature maps in the smaller ROI in (A, black box) at indicated time with red indices representing frames acquired during HIFU application. (E) Maps of APA changes (ΔAPA) in the big ROI displayed in (A). (F) Maps of APD_{50} changes (ΔAPD_{50}) in the same ROI.

Compared to the cases with reversible EP changes, the spatiotemporal evolution of HIFU induced temperature changes showed higher temperature increase with the peak temperature reaching 66.4 ± 8.5 °C (52.1 ~ 84.9 °C). Steep spatial gradients of temperature and higher peak temperature were seen around the HIFU focus (Figure 3.7D).

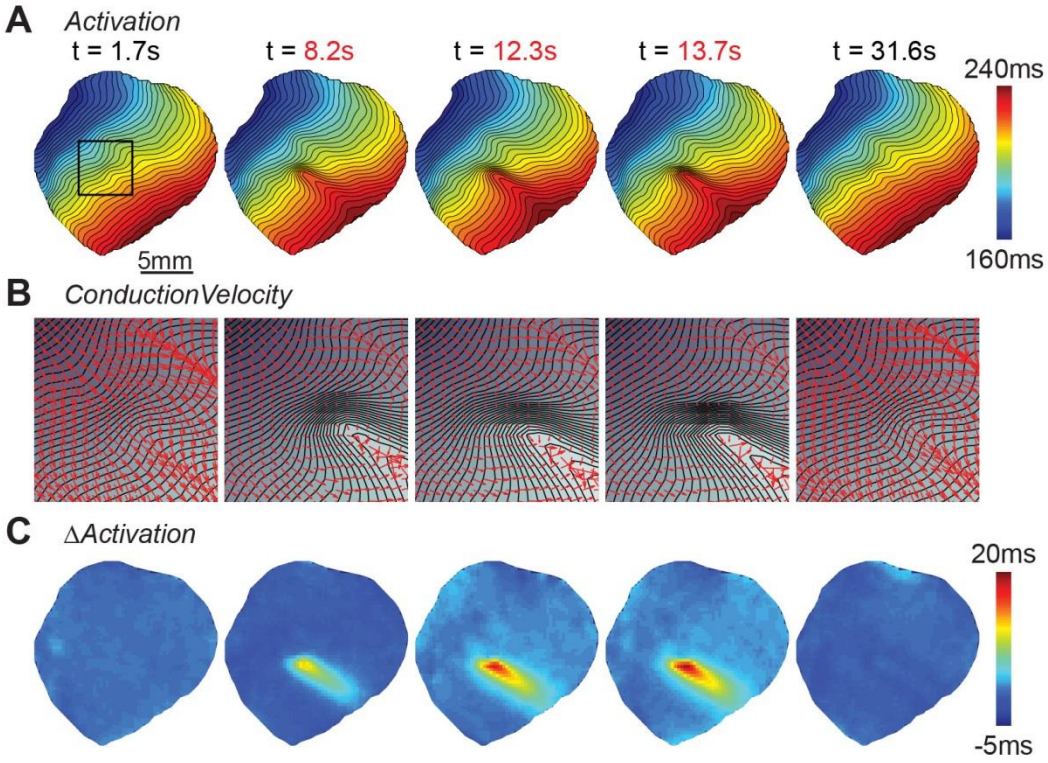

Figure 3.8 Example of activation changes for irreversible case. (A) Activation map prior (1.7 s), during (8.2, 12.3, 13.7 s), and post (31.6 s) HIFU ablation for irreversible damage (ID). Isochrones are separated at 1 ms step size and blue representing early activation and red representing late activation. (B) Maps of conduction velocity (CV) within the black box labeled smaller ROI in (A). Red arrows point the direction of electrical impulses conduction and their lengths represent corresponding magnitudes of CV. (C) Maps of activation delay derived by subtracting averaged activation maps from their pre-HIFU state (1 – 4 s).

The corresponding spatiotemporal OAPs showed sustained changes of APA and APD_{50} induced by HIFU exposures after cessation of HIFU (Figure 3.7E − F). A more significant activation isochronal clustering and changes of CVs were seen as electrical wave propagated through lesion area along with a typical activation delay "tail" (Figure 3.8). Local activation delay was not sustained as HIFU generated lesion was isolated. Similar to the cases with reversible EP changes presented earlier, regions with APA changes were smaller than areas with APD_{50} changes, indicating higher thermal sensitivity for cell-cell coupling

(related to APD). This is consistent with a lower thermal threshold for APD_{50} damage.[5]

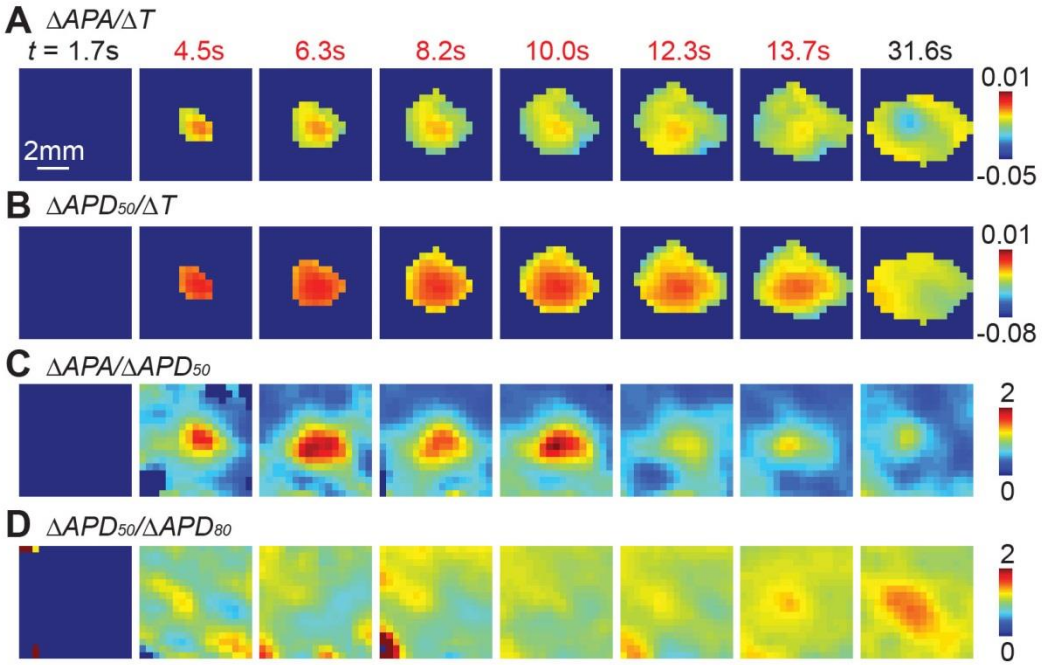

Figure 3.9 Maps of EP and temperature correlation for irreversible ablation case. (A) Ratiometric maps of ΔAPA/ΔT in the smaller ROI of white box in Figure 3.7. (B) Ratiometric maps of $\Delta APD_{50}/\Delta T$ in the same ROI. (C) Maps of $\Delta APA/\Delta APD_{50}$. (D) Maps of $\Delta APD_{50}/\Delta APD_{80}$.

Again, the reduction of APA and APD_{50} increased nonlinearly with increasing temperature (Figure 3.9A – B). Since these changes of APA and APD_{50} were irreversible in these cases with tissue necrosis, ΔAPA/ΔT and $\Delta APD_{50}/\Delta T$ continue to increase after HIFU application as measured at t = 31.6 s when temperature was decreasing. Changes of APA outpaced ΔAPD_{50} changes from the beginning of HIFU application while significant AP triangulation ($\Delta APD_{50}/\Delta APD_{80}$) was also observed around HIFU focus after lesions were formed (Figure 3.9C – D), in contrast to the cases with reversible EP changes.

3.3.3 Characteristics of EP Changes Correlated with Temperature

As shown above, we grouped our experimental data into two groups: reversible damage (RD) group (n = 9) without lesion generation, and irreversible damage (ID) group (n = 6) with lesion formation. As expected, the temperature increases in the ID group were significantly higher than those measured in the RD group, with a maximum temperature (T_{max}) of 50.1 ± 0.8 °C and 66.4 ± 8.5 °C for the RD and ID group respectively (Figure 3.10).

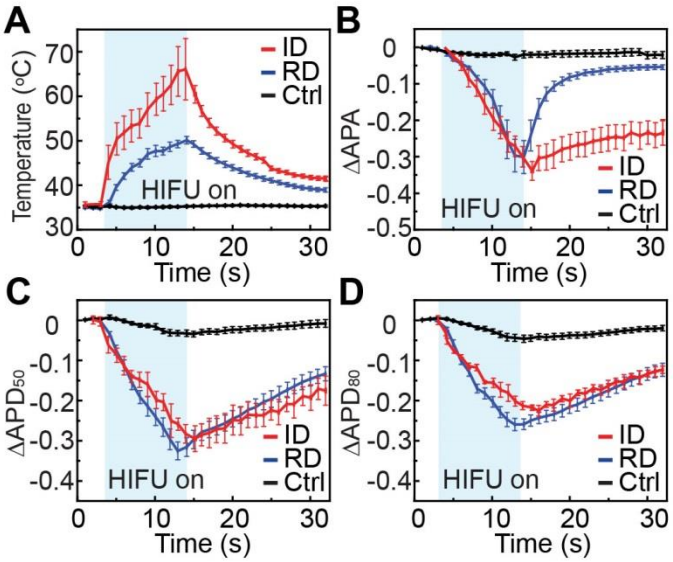

Figure 3.10 Temporal traces of temperature and EP parameters. Statistical progression of (A) temperature, (B) ΔAPA, (C) ΔAPD_{50}, and (D) ΔAPD_{80} for reversible damage (RD) and irreversible damage (ID) within HIFU focus, and control (Ctrl) in normal tissue. Plots are presented as mean ± SEM. HIFU was on from 4 s to 14 s (blue shaded area).

Corresponding to the temperature increases, ΔAPA, ΔAPD_{50} and ΔAPD_{80} increased during HIFU heating (Figure 3.10B − D). The APA eventually recovered after HIFU application for the RD group (− 0.05 ± 0.01), in contrast to the sustained or irreversible change observed for the cases in the ID group (− 0.27 ± 0.04) ($p << 0.05$). However, ΔAPD_{50} showed no significant difference between

both groups during HIFU heating, and the values after HIFU exhibited slight difference (− 0.13 ± 0.02 and − 0.18 ± 0.03 for RD and ID respectively, $p << 0.05$), suggesting that the APA changes after HIFU were more affected by tissue necrosis than APD.

To illustrate how the EP changes corresponding to temperature changes, the values of ΔAPA and ΔAPD_{50} within HIFU focus for RD, ID, and control (normal tissue outside HIFU focus) were plotted against their corresponding temperatures (Figure 3.11). During HIFU heating, the absolute values of ΔAPA increased with increasing temperature. The increase was slow at lower temperatures, but as temperatures reached above 51 °C, larger values of ΔAPA were detected that were not reversible (ID group). During post HIFU cooling (upward arrows in Figure 3.11A), ΔAPA recovered for the RD group, with a fast recovery initially, in contrast to the irreversible changes for the ID group. Unlike APA, the values of APD_{50} seemed to increase relative linearly with increasing temperature from the beginning of HIFU application (Figure 3.11B). These results suggest a lower thermal threshold for generating APD_{50} changes and a dominant thermal effect for HIFU ablation.[7] Recovery of APD_{50} followed similar trend (downward arrows in Figure 3.11) for both groups, but the separation between the damaging and recovering phases was more significant for ID group, indicating a severer cellular AP damages on the ID group during HIFU application.

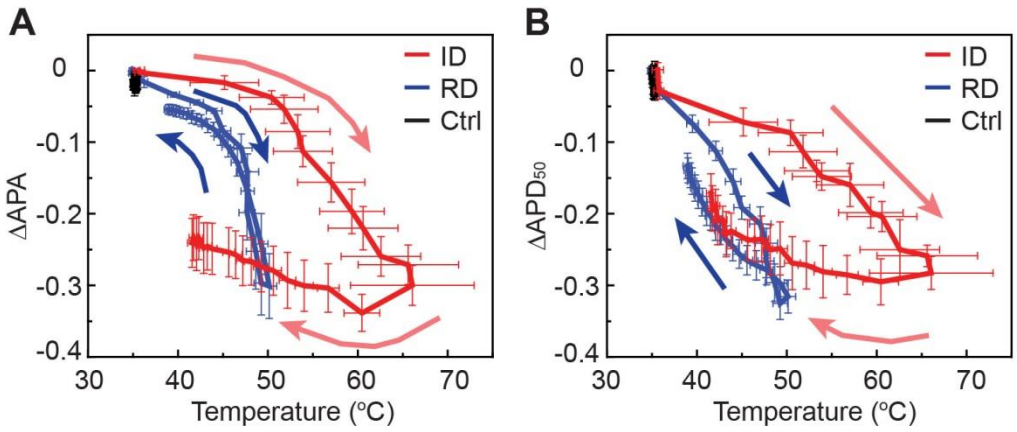

Figure 3.11 Correlation between EP parameters and temperature. (A) ΔAPA vs. temperature, and (B) ΔAPD_{50} vs. temperature for RD, ID, and Ctrl (control) during and after HIFU application. Blue and red arrows indicate the direction of the temporal trends (damaging and recovery) for each parameter. Data are presented as mean ± SEM.

3.3.4 Spatial Characteristics of EP Changes associated with Lesions

For both reversible and irreversible (lesion) cases in this study, we observed that the region with APA changes were smaller than the region with APD_{50} changes (Figure 3.12A – B). Midline profiles of temperature and AP parameters clearly demonstrated that the temperature decreased with increasing distance from the HIFU focus where ΔAPA and ΔAPD_{50} were the largest (Figure 3.12D). Steeper spatial gradient of ΔAPA than that for the ΔAPD_{50} was seen. Considering the tissue and EP changes, the HIFU ablated area was divided into three zones: a lesion zone (e.g. $r < 1.05 \pm 0.07$ mm) where tissue necrosis was present with significant reduction of APA and APD_{50}; a transition zone (e.g. $r < 2.00 \pm 0.22$ mm) with no lesion but with detectable reductions of APA and APD_{50}; and a remote zone (e.g. $r < 3.79 \pm 0.35$ mm) where no tissue changes was seen but APD_{50} reduction was evident. Different pathological changes were observed in different zones: in the lesion zone (Figure 3.12E), hypereosinophilic stained cells were observed, indicating thermal induced protein denaturation, and cellular

structures were incomplete with deranged myofibrils and enlarged interstitial space; in the transition zone or lesion border zone, an inflammatory rim with condensed necrotic band were observed; in the remote zone, cellular structure of myocytes were intact with minimum interstitial space.

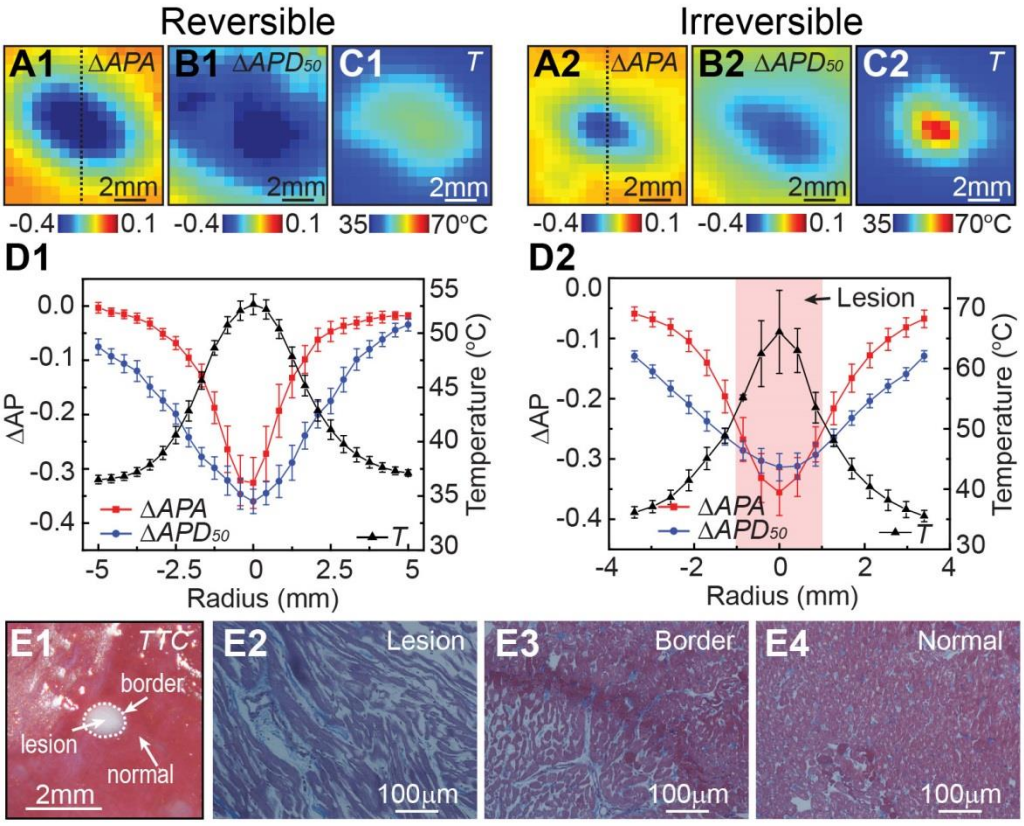

Figure 3.12 Spatial characteristics of lesion and EP changes. (A) An example of ΔAPA map at t = 14 s with dash line representing midline. (B) ΔAPD_{50} map at t = 14 s. (C) Temperature map at t = 14 s. (D) Midline cross-sectional profiles of ΔAPA, ΔAPD_{50}, and temperature for reversible (D1, n = 9) and irreversible (D2, n = 5) cases. Lesion region is indicated by red shaded area. Reversible cases are on the left column and irreversible cases are on the right column. (E1) An example of TTC stained lesion with lesion edge encircled by white dash line. (E2) Masson's trichrome (MT) stained slide (20 X) within lesion. (E3) MT slide of lesion border. (E4) MT slide of normal tissue outside lesion. (E2 – E4) are MT slides for the lesion in (E1).

By overlaying temperature maps on lesion and binary masks of EP determined by a given threshold, we determined the temperature isotherms for

generating tissue necrosis, APA, and APD_{50} changes via ROC analysis (Table 3.1). The APA and APD_{50} masks were generated using threshold values − 0.08 and − 0.10 which were significantly above the noise level (− 0.05 ± 0.03 and − 0.06 ± 0.04 respectively). The temperature isotherms were 52.3 ± 1.4 °C, 42.7 ± 0.1 °C, and 39.6 ± 0.1 °C for lesions, ΔAPA, and ΔAPD_{50} respectively. The lower temperature isotherms for ΔAPD_{50} than ΔAPA again confirmed that APD_{50} was more thermally sensitive than APA, suggesting that cellular plateau potentials were more thermally vulnerable than excitabilities.

Table 3.1 Temperature thresholds for generating lesion, APA loss, and APD_{50} loss in HIFU ablation. Results were derived using receiver-operating characteristic (ROC) analysis on pixel-by-pixel basis.

	Temperature	
	AUC	Threshold (°C)
Lesion (n = 5)	0.84 ± 0.11	52.3 ± 1.4
ΔAPA (n = 7)	0.72 ± 0.06	42.7 ± 0.1
ΔAPD_{50} (n = 7)	0.67 ± 0.06	39.6 ± 0.1

3.3.5 Heat Conduction by Vessel in HIFU Ablation

Blood flow has been known to affect thermal ablation by acting as a "heat sink" due to heat conduction.[6,12] Here we investigated the effect of perfusion cooling on HIFU ablation when the HIFU focus was near a lateral anterior descending (LAD) coronary artery (Figure 3.13A, diagonal branch) with an intensity of 2900 W/cm^2, same as that used in the group with lesion formation. However, no lesion was generated in these experiments and reversible EP changes were observed instead (n = 7).

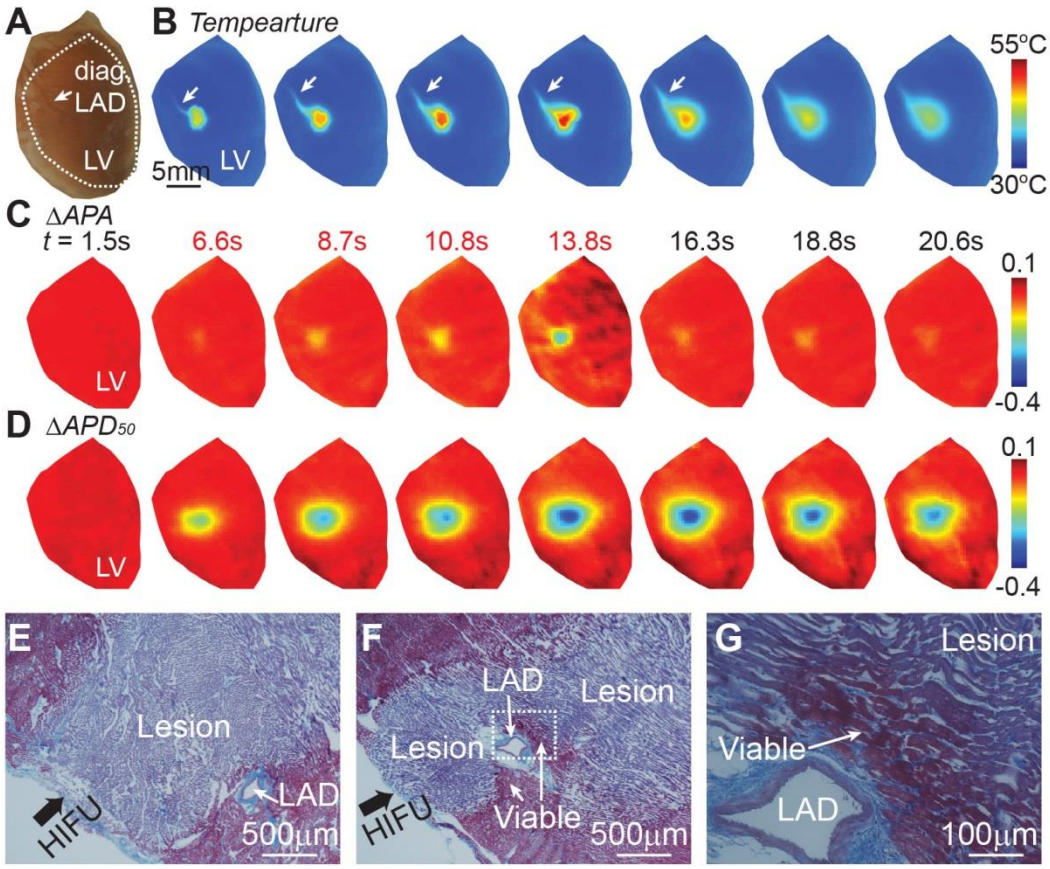

Figure 3.13 Convective heat loss due to perfusion. (A) Photograph of a gross heart with region-of-interest (ROI) encircled by white dash line. Diagonal branch of a lateral anterior descending (LAD) coronary artery is highlighted by a white arrow. (B) IR images during (6.6, 8.7, 10.8, and 13.8 s) and after (16.3, 18.8, and 20.6 s) HIFU ablation with convective heat loss indicated by white arrows within the ROI in (A). (C) Corresponding APA changes. (D) Changes of APD_{50}. (E) Masson's trichrome (MT) stained lesion with LAD coronary artery aside from the HIFU axial beam. (F) MT slide of a HIFU lesion with LAD coronary artery within the field of HIFU beam. HIFU ablation was applied along the black arrow pointed direction for both (E) and (F). (G) Zoomed in (5 X) of ROI of the white box in (F). Lesion was stained as purple while viable tissue was pinkish.

As illustrated in Figure 3.13B, IR imaging clearly showed the heat conduction away from the targeting zone by perfusion in the LAD coronary artery (the "tail" near the upper left of ablation zone [white arrow] in Figure 3.13B). The maximum temperature increase (T_{max}) was 51.1 ± 1.4 °C (n = 7), lower

than the temperature achieved for the ID group (66.4 ± 8.5 °C). No tissue necrosis was detected, and changes of APA and APD_{50} were transient (Figure 3.13C − D).

Histological examination further illustrated the cooling effect on ablation. Figure 3.13F and G show an example with a LAD coronary artery in the center of the HIFU axial beam on a lesion specimen different from Figure 3.13A − D. After MT staining, viable myocytes were observed surrounding the LAD coronary artery as an evidence of significant heat conduction by the artery during HIFU ablation. Compared with the case when LAD coronary artery was outside the HIFU beam (Figure 3.13E), an asymmetric lesion along the HIFU beam was formed (Figure 3.13F − G).

3.4 Discussion

In this study, we conducted spatiotemporally correlated optical mapping of EP and IR imaging of temperature during HIFU ablation to investigate how EP changes were affected by temperature changes. The major findings of this study are (1) HIFU induced EP changes included temperature-dependent reduction of APA, shortening of APD, activation clustering, and increases of conduction velocities around the HIFU focus; (2) tissue EP changes can be reversible with temperature increases below 50.1 ± 0.8 °C; (3) irreversible EP changes along with tissue necrosis occurred as HIFU-induced temperature was above 52.3 ± 1.4 °C; (4) APD_{50} is more thermally sensitive than APA, and APA decreased nonlinearly while APD_{50} decreased relative linearly with temperature increases during HIFU application; (5) HIFU generated irreversible region can be divided into three zones with different tissue physical and EP properties; and (6)

OAP baseline drifts were linearly correlated with HIFU induced temperature rises. We also show the effect of perfusion cooling on EP and temperature during HIFU ablation.

3.4.1 Spatiotemporal Temperature Measurement using IR Imaging

Direct temperature measurement conventionally relies on the use of thermocouples. However, insertion of thermocouples into tissue at discrete locations was not always convenient and feasible, and the thermocouples themselves also introduced error in temperature measurements by a "heat sink" effect via thermal conduction.[4] In this mechanistic study, we employed IR imaging for temperature measurements at high spatial-temporal resolution (< 100 μm, up to 50 Hz) in a noncontact fashion. Although limited to surface measurements, IR imaging and optical mapping basically acquire signals from the same tissue layers (e.g. sub-epicardium) due to spectrum similarity (infrared vs. near-infrared VSD emission), therefore providing a well-suited technique to obtain temperature maps that can be spatiotemporally correlated with OAP signals.

3.4.2 EP Characteristic Correlated with Temperature

Significant EP changes including APA reduction, APD shortening, and conduction time increases have been observed in hyperthermia, RF, and microwave ablation.[5,8,13] In this study, we observed similar EP changes for HIFU ablation for the first time with finer spatiotemporal resolutions, and the detailed dynamics of EP changes were quantitatively investigated. While our results are generally consistent with previously reported results, several discrepancies are noted due to the advancements of the IR and optical mapping technologies.

Reduction of APA was previously reported to linearly depend on temperature between 37.0 °C to 49.9 °C with a relatively smaller Pearson's *r* value (0.54).[5] Our results showed that the reduction of APA changed nonlinearly following HIFU induced temperature rises, with increasing ΔAPA/ΔT during HIFU application. A turning point in the temporal ΔAPA curve (Figure 3.11A) suggested a temperature threshold around 42 °C for significant APA changes. Employing ROC analysis, we calculated the threshold for generating APA changes to be ≥ 42.7 ± 0.1 °C, consistent with previous results (42.7 °C ~ 51.8 °C).[5]

Shortening of APD was also observed to be linearly related to temperature for hyperthermia (Pearson's $r < 0.5$).[5] For RF ablation, Wu *et al*. reported a hysteretic behavior of APD_{80} with $\Delta APD_{80}/T$ being large at the beginning of RF ablation and being small at the end. A counterclockwise damaging and recovering sequence of ΔAPD_{80}-T curve was seen, suggesting a combination of thermal and electrotonic effects for RF ablation.[7] Since HIFU ablation is predominantly thermal in our study, ΔAPD_{50}-T curve was almost linear during HIFU application however with a clockwise damage-recovery hysteresis loop during and after HIFU application. Ideally, ΔAPD_{50}-T curve during cooling phase should follow the same trajectory as heating phase. However, as the peak temperature induced by HIFU was around 50 °C, cellular EP property can be transiently damaged despite that APD_{50} recovered completely in the end, leading to a slower APD_{50} recovery and clockwise hysteretic loop.

The APA and APD_{50} reduction regions were different with the region of ΔAPD_{50} being larger than ΔAPA, indicating a higher thermal sensitivity for APD_{50}. As the APA was the difference between AP peak and the RMP, the increases of the RMP caused by temperature increases may result in reduction of APA. Earlier work suggested the depolarization of RMP became more prominent

when temperature was above 45 °C[5], this may potentially explain the threshold behavior of the temporal APA changes in our study. Temperature increases from 25 °C to 35 °C have also been proved to shorten the inactivation period of L-type calcium channels and lead to shortened APD, indicating the ionic mechanism for a lower temperature threshold for generating APD changes.[14] In our study, we found the temperature threshold for inducing APD_{50} change to be ≥ 39.6 ± 0.1°C, which was significantly lower than the temperature threshold for causing APA changes (42.7 ± 0.1 °C, $p < 0.05$), although with a relatively low ROC AUC (0.67 ± 0.06) (Table 3.1). This may be ascribed to the thermal kinetics of different ion channels which are beyond the scope of the current study.

Simultaneous measurements of temperature and EP changes allowed categorization of HIFU ablation cases into reversible and irreversible groups based on tissue and EP changes including APA and APD. The temperature of 50.1 ± 0.8 °C corresponding to reversible EP changes may be useful as pre-ablation test in complex fractionated atrial electrograms (CFAEs) ablations in EP research laboratories and clinical settings. Compared with previous research that mainly focusing on obtaining HIFU parameters (i.e., acoustic intensity, duty cycle, pulse-repetition frequency) based on tissue necrosis alone,[1,15-17] temperature criterions derived from EP characteristics may provide information that are more relevant for devising strategies to optimize HIFU ablation to avoid recurrence of conduction in atrial fibrillation therapy.[18,19] As expected, no complete electrical conduction block was observed for irreversible cases because of small isolated lesions (Figure 3.8). Three effects including relatively larger pixel size (420 – 460 μm) comparing to smaller lesion (~ 2 mm diameter), optical scattering and "cross-talking" from adjacent pixels, and AP propagation around

and under the non-transmural lesions, combined have caused the conduction block being non-sustained.

With the spatial distributed temperature around HIFU ablation focus, we observed similar radial profiles of APA and APD reductions (Figure 3.12) that were also observed by other researchers. We further divided the HIFU ablated area into three zones: *lesion*, *transition*, and *remote* zones. APA and APD can be transiently suppressed or "stunned" within the latter two zones which may help to explain some of the late conduction blocks or late recurrence of conduction observed clinically.[20]

3.4.3 OAP Baseline Changes Measured during HIFU Ablation

Wu *et al*. observed the OAP baseline shifts during RF ablation, however such baseline change can be prone to artifacts due to tissue-probe contact and movement of RF electrode, therefore has not been rigorously quantified.[7] In our study, as HIFU ablation was performed without direct tissue contact, the OAP baseline drift was most likely induced by HIFU generated temperature changes. We quantitatively compared the OAP baseline drift with temperature for the first time via synchronized measurements of OAP and temperature. Because the observed increase in OAP baseline corresponds to a decrease in the total fluorescence, we speculate that the reduced fluorescence may result from (1) thermal response of the dye[21], (2) changes in tissue properties that may affect dye-membrane binding, and (3) temperature-induced changes in the resting membrane potential (RMP) induced by HIFU exposure. Nath *et al*. demonstrated the RMP followed a sigmoidally-shaped relationship with temperature increases.[5] In our study, the correlation between OAP baseline and temperature increases during HIFU heating appeared to be relatively linear, suggesting the

baseline drift was not merely caused by RMP changes. Jin *et al*. reported a similar di-4-ANEP dye with its fluorescence being affected by the membrane status which became liquid-disordered above a transition temperature and solid phase below the temperature.[22] Similarly, in our experiments, the status of the myocardial membrane phospholipids could transit into more fluid-like phases as HIFU induced temperature crossed certain threshold, making the baseline fluorescence drift. Overall, these three mechanisms may all contribute to the drift of OAP baseline and each of them cannot be studied in isolation. Determining the exact mechanism responsible for this baseline shift may extend beyond the scope of this study.

3.4.4 Perfusion caused Heat Loss during HIFU Ablation

The "heat sink" effect due to major blood vessel has been documented for RF ablation. Especially for ablation at the mitral isthmus (MI), 42 % patients showed unsuccessful MI block when ablation was performed close to coronary artery.[23] HIFU induced heating can be conducted away by blood perfusion in treating liver tumors,[24] therefore more HIFU energy was needed to achieve desired ablation volume. The efficacy of HIFU ablation close to blood vessels may depend on the diameter of the vessel and the flow rate of the blood perfusion. Using two-dimensional IR imaging, we directly observed heat loss by coronary artery flow during HIFU cardiac ablation for the first time. No significant EP damage along LAD coronary artery was generated by HIFU. Perivascular viable tissue was obtained histopathologically, which can help explain the incomplete lesion line in HIFU ablation[18] and the late recurrence of AF after RF ablation in clinical[23]. In addition, geometric narrowing of lesion

towards the epicardium was observed for most HIFU lesions and this can be induced by arterial flow and superfusion.

3.4.5 Experimental Limitations

A Langendorff-perfused rabbit heart model was used in this study, thus results may vary for other species and differ from *in vivo* condition. Excitation-contraction decoupler (BDM) may affect the normal ion channel properties.[25] In addition, continuous light illumination can weaken BDM and cause photo-bleaching of the VSD, affecting the accuracy of the OAP measurement. Although we corrected photo-bleaching using an exponential model, a dual-wavelength ratiometric method may be more appropriate to reduce error.[26] Optical mapping and IR imaging are technically limited to epicardial measurements due to light absorption and scattering across tissue thickness.

3.5 References

1. Engel DJ, Muratore R, Hirata K, Otsuka R, Fujikura K, et al. Myocardial lesion formation using high-intensity focused ultrasound. J Am Soc Echocardiogr. 2006;19:932-937
2. Fujikura K, Otsuka R, Kalisz A, Ketterling JA, Jin Z, et al. Effects of ultrasonic exposure parameters on myocardial lesions induced by high-intensity focused ultrasound. J Ultrasound Med. 2006;25:1375-1386
3. Hsiao Y-S, Kumon RE, Deng CX. Characterization of lesion formation and bubble activities during high-intensity focused ultrasound ablation using temperature-derived parameters. Infrared Physics & Technology. 2013;60:108-117
4. Rivens I, Shaw A, Civale J, Morris H. Treatment monitoring and thermometry for therapeutic focused ultrasound. Int J Hyperthermia. 2007;23:121-139

5. Nath S, Lynch C, 3rd, Whayne JG, Haines DE. Cellular electrophysiological effects of hyperthermia on isolated guinea pig papillary muscle. Implications for catheter ablation. Circulation. 1993;88:1826-1831

6. Haines DE. The biophysics of radiofrequency catheter ablation in the heart: The importance of temperature monitoring. Pacing Clin Electrophysiol. 1993;16:586-591

7. Wu CC, Fasciano RW, 2nd, Calkins H, Tung L. Sequential change in action potential of rabbit epicardium during and following radiofrequency ablation. J Cardiovasc Electrophysiol. 1999;10:1252-1261

8. Wood MA, Fuller IA. Acute and chronic electrophysiologic changes surrounding radiofrequency lesions. J Cardiovasc Electrophysiol. 2002;13:56-61

9. Parsons JE, Cain CA, Fowlkes JB. Cost-effective assembly of a basic fiber-optic hydrophone for measurement of high-amplitude therapeutic ultrasound fields. J Acoust Soc Am. 2006;119:1432-1440

10. Madding RP. Emissivity measurement and temperature correction accuracy considerations. 1999:393-401

11. Fishbein MC, Meerbaum S, Rit J, Lando U, Kanmatsuse K, et al. Early phase acute myocardial infarct size quantification: Validation of the triphenyl tetrazolium chloride tissue enzyme staining technique. Am Heart J. 1981;101:593-600

12. Fuller IA, Wood MA. Intramural coronary vasculature prevents transmural radiofrequency lesion formation: Implications for linear ablation. Circulation. 2003;107:1797-1803

13. Whayne JG, Nath S, Haines DE. Microwave catheter ablation of myocardium in vitro. Assessment of the characteristics of tissue heating and injury. Circulation. 1994;89:2390-2395

14. Puglisi JL, Yuan W, Bassani JW, Bers DM. Ca(2+) influx through ca(2+) channels in rabbit ventricular myocytes during action potential clamp: Influence of temperature. Circ Res. 1999;85:e7-e16

15. Okumura Y, Kolasa MW, Johnson SB, Bunch TJ, Henz BD, et al. Mechanism of tissue heating during high intensity focused ultrasound pulmonary vein

isolation: Implications for atrial fibrillation ablation efficacy and phrenic nerve protection. J Cardiovasc Electrophysiol. 2008;19:945-951

16. Villamizar NR, Crow JH, Piacentino V, 3rd, DiBernardo LR, Daneshmand MA, et al. Reproducibility of left atrial ablation with high-intensity focused ultrasound energy in a calf model. J Thorac Cardiovasc Surg. 2010;140:1381-1387 e1381

17. Solomon SB, Nicol TL, Chan DY, Fjield T, Fried N, Kavoussi LR. Histologic evolution of high-intensity focused ultrasound in rabbit muscle. Invest Radiol. 2003;38:293-301

18. Laughner JI, Sulkin MS, Wu Z, Deng CX, Efimov IR. Three potential mechanisms for failure of high intensity focused ultrasound ablation in cardiac tissue. Circ Arrhythm Electrophysiol. 2012;5:409-416

19. Oral H, Knight BP, Ozaydin M, Tada H, Chugh A, et al. Clinical significance of early recurrences of atrial fibrillation after pulmonary vein isolation. J Am Coll Cardiol. 2002;40:100-104

20. Ouyang F, Antz M, Ernst S, Hachiya H, Mavrakis H, et al. Recovered pulmonary vein conduction as a dominant factor for recurrent atrial tachyarrhythmias after complete circular isolation of the pulmonary veins: Lessons from double lasso technique. Circulation. 2005;111:127-135

21. Clarke RJ, Kane DJ. Optical detection of membrane dipole potential: Avoidance of fluidity and dye-induced effects. Biochim Biophys Acta. 1997;1323:223-239

22. Jin L, Millard AC, Wuskell JP, Dong X, Wu D, et al. Characterization and application of a new optical probe for membrane lipid domains. Biophys J. 2006;90:2563-2575

23. Kurotobi T, Shimada Y, Kino N, Iwakura K, Inoue K, et al. Local coronary flow is associated with an unsuccessful complete block line at the mitral isthmus in patients with atrial fibrillation. Circ Arrhythm Electrophysiol. 2011;4:838-843

24. Jiang F, He M, Liu YJ, Wang ZB, Zhang L, Bai J. High intensity focused ultrasound ablation of goat liver in vivo: Pathologic changes of portal vein and the "heat-sink" effect. Ultrasonics. 2013;53:77-83

25. Cheng Y, Mowrey K, Efimov IR, Van Wagoner DR, Tchou PJ, Mazgalev TN. Effects of 2,3-butanedione monoxime on atrial-atrioventricular nodal conduction in isolated rabbit heart. J Cardiovasc Electrophysiol. 1997;8:790-802

26. Knisley SB, Justice RK, Kong W, Johnson PL. Ratiometry of transmembrane voltage-sensitive fluorescent dye emission in hearts. Am J Physiol Heart Circ Physiol. 2000;279:H1421-1433

CHAPTER 4

Parametric Ultrasound Imaging of HIFU Ablation

Effective intra-procedural imaging techniques are important for guiding ablation of AF. However, direct transmural correlation between lesion and electrophysiological (EP) changes is difficult. Different from previous chapters of using intact heart model, in this chapter, we used a perfused canine ventricular wedge preparation to investigate the transmural tissue and EP changes induced by HIFU ablation in a spatiotemporally correlated fashion using optical mapping described earlier and ultrasound imaging. By correlating with lesion histology and EP changes, we demonstrated the feasibility of parametric ultrasound imaging for detection lesion and EP changes transmurally during HIFU ablation.

4.1 Overview

As described in CHAPTER 1, atrial fibrillation (AF) is a common cardiac condition occurring in patients with or without overt heart disease.[1] Cardiac ablation using various energy sources (e.g. radiofrequency, cryo, HIFU) has

increasingly become an important treatment option.[2,3] However, ablation efficacy is often compromised by recurrence of AF episodes after initial procedure. For example, 20 % to 40 % patients experience recurrent AF and will need repeated ablation procedures.[4] This is likely due to incomplete tissue necrosis, ablation gaps, and electrical reconnection from tissue healing.[5-8] Intra-operative electrogram and electroanatomical voltage mapping have been used to confirm success of ablation clinically, but it is difficult to precisely relate such surface measurements to tissue changes in a transmural plane due to the lack of effective imaging technique for detecting lesion and APA changes along the tissue depth direction.

4.1.1 Imaging Technique for Cardiac Ablation

Various imaging techniques have been developed for assessing thermal lesions during ablation. Magnetic resonance imaging (MRI)[9], intracardiac echocardiography (ICE)[10], and fluoroscopy, commonly used to identify anatomic structures to guide the placement of ablation catheter, have not provided sufficient intra-operative assessment of tissue physical and EP changes. Measurements such as tissue electrical impedance[11], ablation temperature[12], and catheter-tissue contact force[13] provide useful feedback for energy titration and prediction of lesion volume, but accuracies of lesion estimation are suboptimal. Direct tissue surface visualization using endoscopy during pulmonary vein isolation (PVI)[14] cannot provide complete lesion assessment in a transmural plane along the tissue depth direction. Optical coherence tomography (OCT), with superior imaging resolution, is also limited by imaging tissue depth only up to 2 mm.[15]

Therefore, development of transmural lesion imaging for accurate lesion detection and EP assessment can be highly beneficial for ablation guidance. As ultrasound imaging has the unique capability to "see" through and into soft tissue layers, various advanced ultrasound imaging techniques have been exploited to improve its capability for real time monitoring of lesion formation in subsurface tissue layers. For examples, Wright *et al*. showed a novel M-mode ultrasound imaging integrated into a radiofrequency ablation (RFA) catheter for direct visualization of lesion formation in real time[16], demonstrating an advantageous approach for image-guided procedures. Kolios *et al*. demonstrated high frequency ultrasound backscatter signals can be used to effectively detect apoptotic changes in cell nucleus using spectral analysis method[17], indicating changes in the nucleus, such as apoptotic, necrosis or other changes, may produce detectable signals for high frequency ultrasound imaging for monitoring events reflective of cellular level changes. We have previously shown that high frequency ultrasound imaging at 55 MHz combined with fast frame rate M-mode (1 kHz) and short time B-mode (70 – 130 frames/s) imaging can image HIFU lesion and gas body formation[18,19] with high accuracy and resolution by tracking the temporal history of ultrasound integrated backscatter (IBS) and frame-to-frame echo decorrelation. ICE-based acoustic radiation force impulse (ARFI) imaging provided improved performance in identifying lesion boundaries and dimensions in RFA lesion lines[20], although motion artifacts sometimes led to false classification of lesions with low imaging frame rate (< 4 frames/min).

4.1.2 Transmural Cellular Electrophysiology

Electroanatomical mapping combined with pacing technique is used clinically for validating ectopic foci isolation after ablation, however, the technique is based on surface measurement thus it is difficult to directly relate such measurements to transmural tissue status in a three-dimensional (3D) space. Given that cellular repolarization varies with the depth of myocardium across ventricular wall due to heterogeneous excitation-contraction coupling[21,22], it is unclear whether cellular EP exhibits different characteristics in different transmural tissue layers when lesion is formed in ablation. Using microelectrode recording at isolated locations within myocardium, Wood *et al*. showed similar changes of action potential amplitude, duration, and upstroke velocity surrounding a RF lesion across epi-, mid-, and endocardium[23], however, a complete spatiotemporal evaluation of EP changes across the depth of the myocardium in a transmural plane during and after lesion formation remains unrevealed.

In this study, in order to investigate the sptatiotemporal changes of tissue and correlate them with AP changes in a transmural plane along the tissue depth direction during HIFU ablation, we used a perfused canine ventricular wedge preparation as a model system which enabled simultaneous ultrasound imaging and optical mapping on the same transmural plane during HIFU ablation. Although the wedge preparation is not necessarily the best model representing an intact heart *in vivo*, the model system permitted high spatiotemporal resolution measurement of EP changes during HIFU ablation using optical mapping that can be correlated with ultrasound imaging of the same tissue plane, which cannot be achieved with an intact heart either *in vitro* or *in vivo*. These measurements allowed characterization of the EP changes induced by

HIFU ablation, and by correlating with lesion histology, we tested parametric ultrasound imaging for detecting lesion and AP changes across the ventricular depth direction during HIFU ablation.

4.2 Methods

4.2.1 Perfused Canine Wedge Preparation

Animal use was approved by the University Committee on Use and Care of Animals (UCUCA) at the University of Michigan. The transmural wedges of canine ventricular wall were isolated from mongrel dogs (25 − 40 kg) as described before[24]. Briefly, freshly harvested canine heart was immediately aortic rinsed, and arrested with a 4°C cardioplegic solution[21]. Wedge with a dimension of ~ 4 × 1.5 × 1.5 cm with smooth transmural surfaces was dissected using microtome blades from the anterolateral or posterior-lateral free wall of either left ventricle (LV) or right ventricle (RV) supplied by left anterior descending (LAD) coronary arteries or marginal right coronary arteries (RCA) (Figure 4.1). A custom flexible plastic cannula was inserted into the section of the artery from the base along the wedge length, and major arterial leaks were quickly (< 10 mins) ligated with suture. Perfusion was validated by injection of Methylene Blue dye (Sigma, St. Louis, MO, USA), and poorly perfused wedges were discarded. The isolated wedge was then mounted in a tissue holder, placed onto a perfusion system, and perfused with oxygenated Tyrode's solution[25] (pH = 7.35 ± 0.05; 37 °C; 95 % O_2/5 % CO_2) at constant arterial pressure (50 – 60 mmHg).

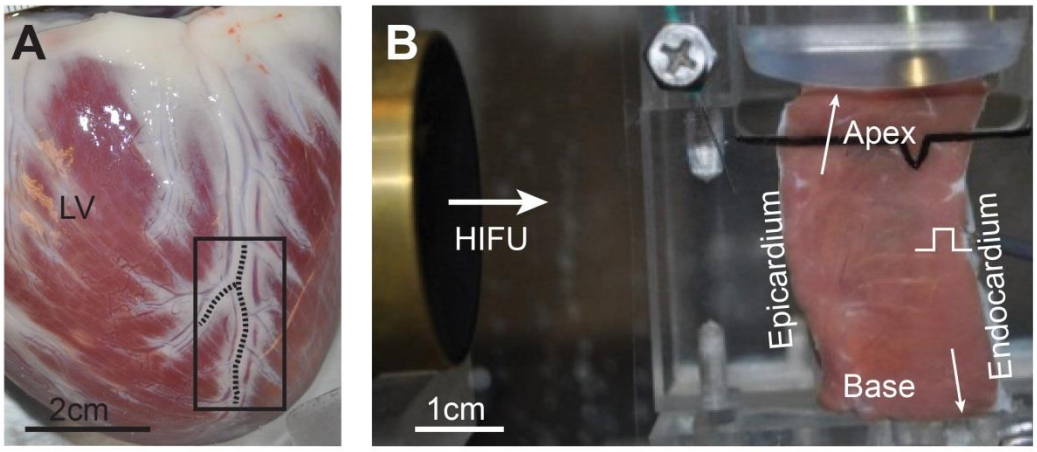

Figure 4.1 Canine left ventricular wedge preparation. (A) A photograph of a canine heart immersed in cardioplegia before wedge preparation. The black box indicates the tissue region used on left ventricle (LV). Dash lines highlight marginal coronary arteries. (B) A photograph of a coronary perfused left ventricle wedge with epicardium at the left, endocardium at the right, apex on top, and base at the bottom of the photograph. HIFU energy was delivered from the left.

The preparation was completely bathed in the same solution and slowly warmed up by superfusion. The wedge was then paced from either endocardium or epicardium at a cycle length (CL) of 1000 ms until a stable Q-T interval was reached on ECG (30 – 40 mins). The ECG and arterial pressure were continuously monitored (PowerLab 26T, AD Instruments, Colorado Springs, CO, USA) via two floating electrodes to ensure physiological stability of the preparation during experiments. After adding excitation-contraction decoupler, 2, 3-butanedione monoxime (BDM, 15 mM; Fisher Scientific, Pittsburgh, PA, USA) into the perfusate, the wedge was stained with a voltage-sensitive dye (VSD) di-4-ANEPPS (Invitrogen, Life Technologies, Grand Island, NY, USA) at 15 μM. Stabilized for 15 mins, the transmural surface of the wedge was gently pushed against a flat acoustically transparent screen (Figure 4.1).

4.2.2 Optical Mapping, Ultrasound Imaging, and HIFU Ablation

Figure 4.2 shows a schematic graph of the experiment setup for spatiotemporally correlated optical mapping and ultrasound imaging of HIFU ablation. Optical mapping used two green-filtered light emitting diodes (531 ± 45 nm, 5G Illumination, SciMedia USA Ltd., Costa Mesa, CA, USA) for excitation. A 100 × 100 pixel CMOS camera system (MiCAM Ultima-L, SciMedia USA Ltd.) was used to record the long-pass filtered (> 630 nm) emission fluorescence from the transmural surface of the wedge (1000 frames/s and spatial resolution 200 - 260 μm/pixel). Imaging using M2D-mode (M-mode imaging with a two-dimensional window size of 17.0 × 5.6 mm) of a Vevo 770 (FUJIFILM VisualSonics, Inc., Toronto, Ontario, Canada) was used to acquire the backscattered raw radio-frequency (RF) signals (11 frames/s). A RMV 707B probe (30 MHz, 12.7 mm focal length, 2.2 mm 6-dB focal depth, and 45 MHz bandwidth) was orthogonally and con-focally aligned with the CMOS camera to image the same transmural plane (< 0.5 mm variation) of the wedge using a 3D measurement procedure. A triangular cut on the edge of the flat polycarbonate film (transparent for both HIFU and ultrasound imaging) screen (Figure 4.1) was used as a fiducial marker which can be seen on both optical mapping and ultrasound imaging.

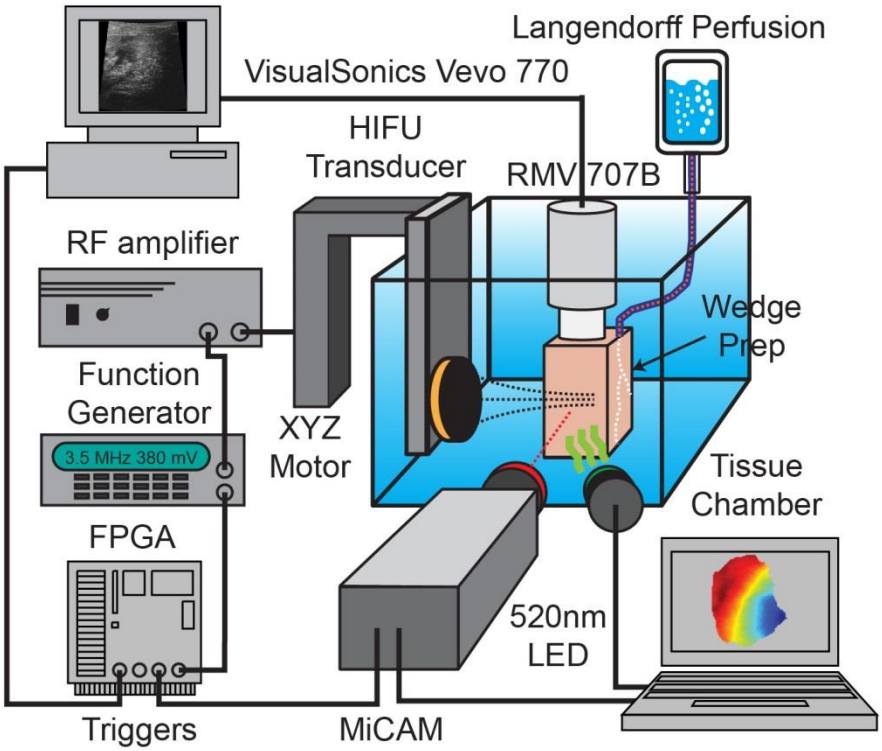

Figure 4.2 Schematic experiment setup of simultaneous optical mapping, ultrasound imaging, and HIFU ablation. The HIFU transducer is mounted on a high precision XYZ motor stage. Imaging and ablation were synchronized via a custom programmed FPGA circuit.

A concave single element HIFU transducer (3.5 MHz, SU-102, Sonic Concepts, WA) driven by a signal generator (33250A, Agilent Technologies, Inc., Santa Clara, CA, USA), and a 75W power amplifier (75A250, Amplifier Research, Souderton, PA, USA), was used for HIFU application from the epi/endocardial surface of the wedge preparation. The HIFU transducer has a focal length of 56.5 mm and 6-dB focal zone of 0.6 mm (lateral) × 7 mm (axial) measured with a custom fiber optic probe hydrophone (FOPH) system.[26] The transducer was aligned perpendicularly with the ultrasound imaging probe with its focus placed slightly (< 0.5 mm) beneath the transmural surface.

Optical mapping, ultrasound imaging and HIFU ablation were synchronized via a custom-programmed FPGA board (Cyclone® II, Altera, San Jose, CA, USA). Synchronized with the continuous 32 s optical mapping, M2D ultrasound imaging was from t = 4 s to 8.6 s, and HIFU was applied from t = 4.5 s to 8.5 s. M2D backscattered RF signals were digitized using an 8-bit oscilloscope (54830B, Agilent Technologies, Inc., Santa Clara, CA, USA) at 100 Mega-sample/s. Pulsed HIFU exposure (pulse-repetition-frequency = 11 Hz, duty cycle = 70%, duration 4 s, and spatial-peak pulse-average intensity [I_{sppa}] = 3500 ± 300 W/cm^2) was applied epi/endocardially to generate a single lesion near the wedge transmural surface to allow simultaneous optical mapping and ultrasound imaging. HIFU pulses were interleaved with M2D ultrasound imaging to avoid HIFU interference in ultrasound imaging. Before and after each mapping-ablation procedure, B-mode ultrasound images with a larger FOV (16.5 × 18.9 mm), and color photographs of the wedges were obtained.

4.2.3 Analysis of Optical Mapping Data

Optical mapping images were analyzed similarly as in CHAPTER 1. Briefly, 3 × 3 spatial binning and 1 – 100 Hz FIR band-pass filter were applied for spatiotemporal smoothing. The measured optical action potentials (OAPs) were normalized to range of between 0 and 1. Activation map was constructed based on the time needed for d(ΔF)/dt to reach the maximum value during each cycle, where ΔF is the fractional fluorescence change, defined as the change of fluorescence signal divided by the background fluorescence. AP duration at 50% and 80% repolarization (APD_{50} and APD_{80}) were calculated as the duration from the activation time to 50% or 80% of the peak AP amplitude during repolarization. AP upstroke rising rate was defined as $(d(\Delta F)/dt)_{max}$ and

conduction velocity (CV) was the spatial gradient of the activation time. The changes of corresponding AP parameters were calculated by subtraction of the average of pre-HIFU frames. A demonstration of optical mapping data processing is shown in Figure 4.3.

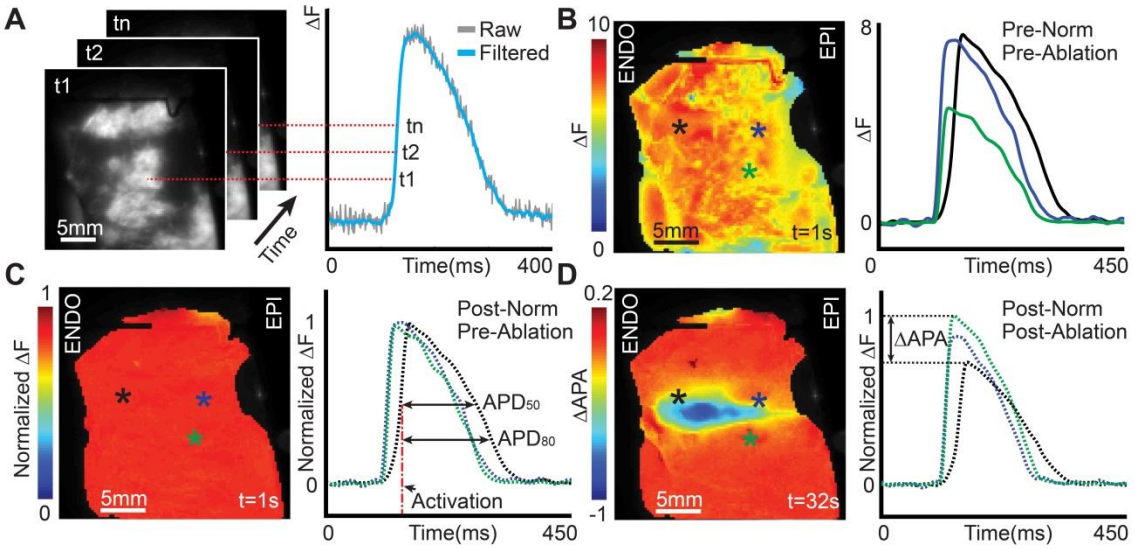

Figure 4.3 Example of optical mapping data analysis. (A) Sequential images (t_1, t_2, … , t_n) were acquired via optical mapping on a canine left ventricular (LV) wedge. Temporal recording at each pixel corresponds to optical trans-membrane action potential. Raw optical signal is filtered through FIR filter and fractional fluorescence changes (ΔF) are used to describe optical action potentials (OAPs). (B) Within one cardiac cycle, maps of ΔF amplitude before high-intensity focused ultrasound (HIFU) ablation are generated. Representative OAP traces at color asterisks labeled locations are presented. Since perfusion of voltage sensitive dye is not perfectly uniform from endocardium (ENDO) to epicardium (EPI), the ΔF amplitude map is non-uniform before HIFU ablation. (C) ΔF amplitude map is further normalized to its initial state (temporal average of first 4 ΔF amplitude maps). (D) Upon HIFU ablation, normalized ΔF amplitude decreased within HIFU focal region and led to OAPs amplitude reduction. The amount of normalized ΔF amplitude reduction is defined as ΔAPA and the reconstructed ΔAPA is illustrated with representative OAPs trace.

4.2.4 Parametric Ultrasound Imaging

Backscattered RF signals of ultrasound images were collected prior, during, and after HIFU application and were processed off-line. The amplitude

of Hilbert transformed RF signals, yielded the envelope data A(x, y; t), which was used to form various ultrasound parametric images as described in earlier works.[18,27] Briefly, gray-scale (GS) ultrasound images were computed as the logarithmic compression of the envelope data (in decibels)[18]

$$GS(x,y;t) = 10\log_{10}(\langle A(x,y;t)\rangle) \qquad 4.1$$

Integrated backscatter (*IBS*), a parameter related to acoustic impedance of the tissue, was calculated as the averaged power spectral density over a limited bandwidth (in decibels)[18]

$$IBS(x,y;t) = 10\log_{10}(\langle A^2(x,y;t)\rangle) \qquad 4.2$$

Rayleigh distribution parameter (α, Eq. 4.3) and scale parameter of log-normal distribution (σ, Eq. 4.4), both reflecting the spatial organization of ultrasonic scatters, were calculated based on the spatial intensity distribution of the envelope data using a maximum likelihood estimates (MLE) method[27]

$$p(A(x,y;t)) = \frac{2A}{\alpha} e^{-A^2/\alpha} \qquad 4.3$$

$$p(A(x,y;t)) = \frac{1}{A\sigma\sqrt{2\pi}} e^{-\frac{(\ln A-\mu)^2}{2\sigma^2}} \qquad 4.4$$

Figure 4.4 shows an example of generating Rayleigh and log-normal parametric image from ultrasound envelope image.

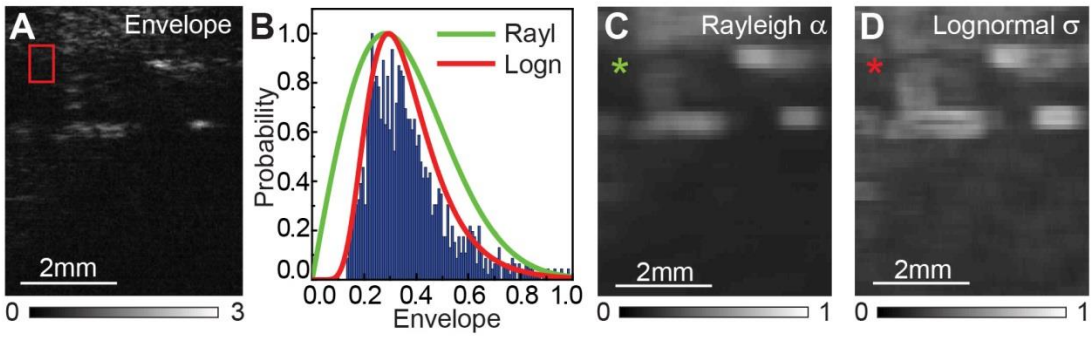

Figure 4.4 Example of generating ultrasound parametric images. (A) An ultrasound M2D-mode envelope image is presented with a red rectangular window (100 × 13 pixels). (B) Histogram of pixel intensity within the red window in (A) is plotted as blue bars. Histogram is fitted using probability density functions of Rayleigh (Rayl, green) and log-normal (Logn, red) distribution model. Rayleigh and log-normal parameters are estimated using MLE method. (C) Rayleigh image with the green asterisk labeled pixel indicating α value in the red window. (D) Log-normal image with the red asterisk labeled pixel indicating σ value in the red window.

The temporal evolution for any given ultrasound parameter X(x, y; t) defined in Eq. 4.1 – Eq. 4.4 is then calculated as the following

$$X_t(x,y;t) = \left| X(x,y;t) - X(x,y;t-1) \right| \qquad 4.5$$

$$X_c(x,y;t) = \left| X(x,y;t) - X(x,y;0) \right| \qquad 4.6$$

$$X_{\max}(x,y;t) = \max_{t'} \left| X(x,y;0 \le t' \le t) \right| \qquad 4.7$$

Transient change of X is defined as the absolute difference between two adjacent frames (Ep. 4.5). Cumulative change of X is the absolute difference between the current frame at *t* and the average of pre-HIFU recording. Cumulative extrema is the temporal maximum of the transient changes. This function captures the entire time history of any parameter changes which occurred during HIFU application. Figure 4.5 shows an example of the transient change, cumulative

change, and cumulative extrema of grayscale image. The temporal changes for all parametric images were normalized in the end for further analysis.

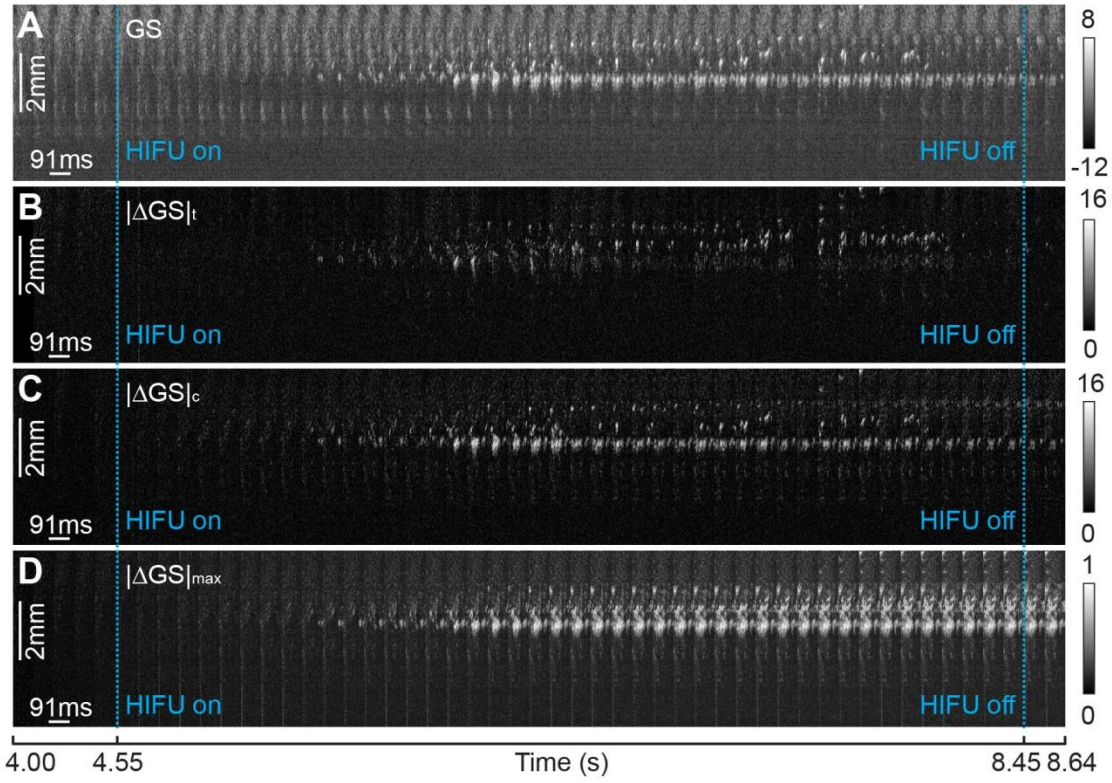

Figure 4.5 Example of temporal changes of gray-scale images. (A) Horizontally stacked gray-scale (GS) M2D-mode ultrasound images in decibels [dB] with blue dash lines representing the start and cessation of HIFU ablation. (B) Transient changes of GS images. (C) Cumulative changes of GS images. (D) Cumulative extrema of GS images with normalization.

4.2.5 Histology, Lesion Assessment, and Image Registration

Immediate after each ablation trial, wedge preparations were stained with triphenyltetrazolium (TTC, Sigma Aldrich, St. Louis, MO, USA) following a previously described protocol[28] and were photographed again. Finally, all wedge tissues were stored in 10 % formalin for > 48 hours. Formalin-fixed tissue blocks were paraffin-embedded, sectioned at 5 μm and went through masson's

trichrome (MT) staining. MT stained slides were scanned using a high resolution scanner (CanoScan 8800F, Canon USA, Inc., Melville, NY, USA) and the boundaries of HIFU induced lesions were identified using a custom semi-automatic Matlab algorithm (v. 2012b, Mathworks, Natick, MA, USA). Briefly, color-based segmentation using *k*-means clustering and simple Markov random field (MRF) model were used to differentiate lesion from normal tissue. Algorithm detected lesion masks were then combined with hand-picked lesion contours to further reduce detection errors. Lesion boundaries detected from images of MT slides, TTC stained images, and photographs of gross tissue showed high similarity (> 98 %). Due to potential artifacts associated with histology preparation (e.g. tissue deformation during embedding and slicing), we used gross images taken immediately after experiments to detect lesion boundary for ultrasound parametric imaging analysis.

Ultrasound M2D images, tissue gross photographs, and optical mapping images were registered based on the fiducial marker (red asterisk) on the flat imaging screen as depicted in Figure 4.6. MT stained slides and tissue gross photographs were also registered via lesion geometry (e.g. lesion centroids). A representative example of registered images was shown in Figure 4.6. The region-of-interest (ROI) in M2D imaging window (green box) was further reduced to 6 × 5.6 mm for further analysis.

Receiver operating characteristic (ROC) analysis was performed to determine whether HIFU induced ΔAPA corresponds to lesion. ROC analysis was also performed to test ultrasound imaging parameters we used for detecting lesion and ΔAPA. Leave-one-out (LOO) cross-validation was employed to determine the variation of ROC analysis. Results are presented as mean ± standard deviation unless specified otherwise. Kruskal-Wallis ANOVA were

used for statistical comparisons between groups and $p < 0.05$ was considered statistical significant.

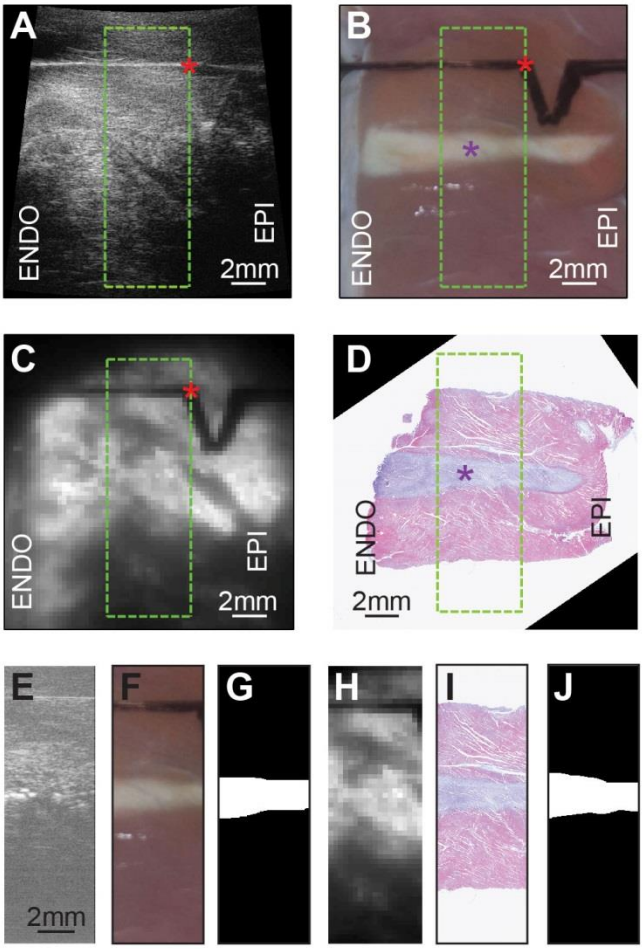

Figure 4.6 Ultrasound, gross, optical, and histological images registration. (A) Ultrasound B-mode image of a wedge preparation after HIFU ablation. Green box indicates the field-of-view (FOV) of M2D imaging and red asterisk at a corner of the fiducial marker on the acoustic transparent screen. ENDO = endocardium, EPI = epicardium. (B) Photograph of the same wedge with purple asterisk labeling the lesion centroid. (C) Background optical mapping image. M2D, gross, and optical images were registered based on the FOV and fiducial marker. (D) Masson's trichrome (stained) microscopic slide of the same transmural plane. (E - J) Registered FOV of M2D image, gross image, lesion mask from gross image, background optical image, MT slide, and lesion mask from MT image.

4.3 Transmural Lesion and EP Imaging

4.3.1 Transmural Optical Mapping of Canine Wedge

The OAPs, activation pattern, and APD measured from the perfused wedge preparations in this study, whether pacing either endocardially (n = 7) or epicardially (n = 6), are consistent with reported results.[24] Figure 4.7 shows an example of a canine LV wedge preparation under a pacing rate of 60 bpm (CL = 1000 ms), showing systematic activation and steep spatial APD_{80} gradient from epicardium to endocardium transmurally with shorter APD_{80} near the epicardium and longer APD_{80} near the endocardium. The observed AP morphology at different layers was consistent with that under normal sinus rhythm, indicating sufficient perfusion, cell-cell coupling, and absence of ischemic regions in the wedge preparation.[21] The perfused preparations were viable with normal EP for over 3 hours and all experiments were performed within this period.

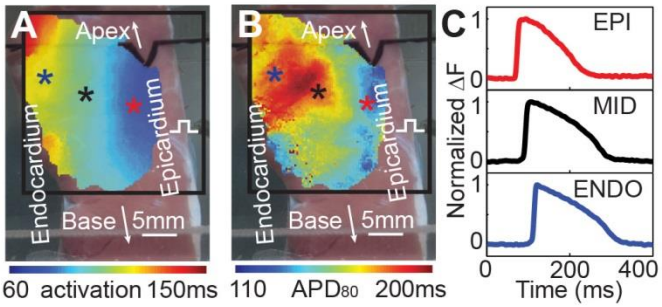

Figure 4.7 Electrophysiology and OAPs of a canine left ventricular wedge preparation. (A) Activation map superimposed on the photograph of the transmural surface of the wedge. The large black box is the region of interest for optical mapping. The color asterisks indicate locations where OAPs were plotted. Pacing (cycle length = 1000 ms) was applied from the epicardium. (B) APD_{80} map superimposed on the same wedge. (C) Representative OAPs at subepicardium (EPI), midmyocardium (MID), and subendocardium (ENDO) indicated by the colored asterisks in (A) and (B).

4.3.2 Transmural EP Changes and Lesion generated by HIFU

HIFU generated single lesion, either cigar-shaped (n = 4) or tadpole-shaped (n = 9), as indicated by the pale or discolored region in gross photograph and MT stained slide, were 12.27 ± 2.03 mm × 2.86 ± 0.57 mm (n = 13) along the depth of ventricular wedges (Figure 4.8). Lesion regions detected from MT images, TTC stained images, and gross photographs showed high similarity (> 98% pixel-by-pixel match).

Microscopically, condensed cytoplasmic filament and loss of cellular structure were observed near the center necrotic area. A border zone was seen as a rim of necrotic contraction band with apparent hemorrhage or inflammation but intact cell structures. Outside the border zone, cardiomyocytes were intact (Figure 4.8). No microscopic cavity was observed on the lesion MT slides, suggesting minimum effects from high temperature related "boiling" or HIFU induced cavitation. Correspondingly, different EP characteristics were observed within and surrounding HIFU lesions in the ventricular transmural plane. Near the lesion center, significant APA reduction (~80 %) was accompanied by significantly more APD shortening, AP triangulation, and reduced upstroke rising rate (Figure 4.8). Fewer changes were seen in the border zone and no changes were observed in tissue regions further away (Figure 4.8).

Overall higher APA reduction was seen near lesion center than in border zone (n = 13). Similarly, APD_{50} and APD_{80} shortening (up to 33 % and 21 % respectively) were more severe near the center than in border zone. However, shortening of APD extended up to 2.8 mm for APD_{50} and 2.0 mm for APD_{80} beyond lesion boundary or region of APA reduction. Transmurally, more APD reduction was seen near epicardium than endocardium, implying different

thermal resistivity across ventricular wall. Decrease of APD_{50}/APD_{80} (from 0.8 to 0.74) suggested influence of HIFU on the plateau potential.

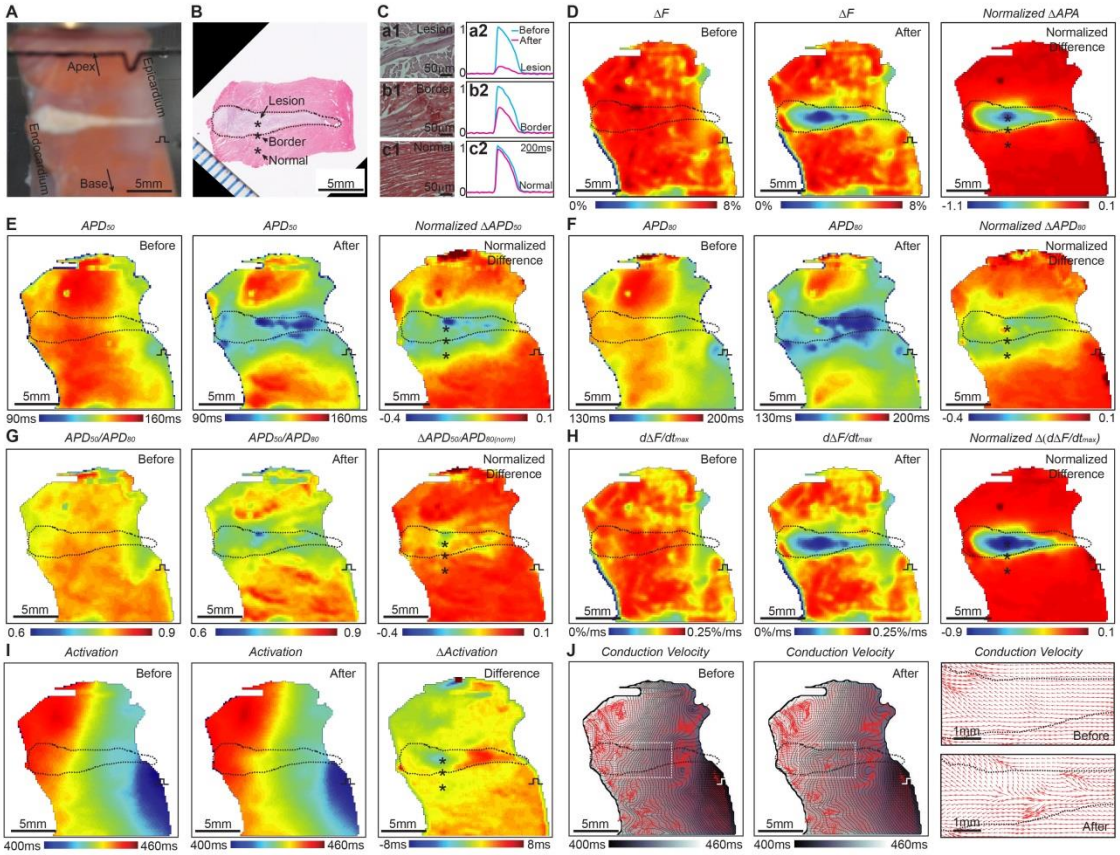

Figure 4.8 Spatiotemporal changes of transmural EP of wedge preparation around HIFU lesion. (A) Photograph of a LV wedge with HIFU lesion. (B) Masson's trichrome (MT) stained slide of the same wedge with lesion. Black dash line encircles lesion boundary. Black asterisks label representative locations inside lesion, border, and normal tissue. (C) Microscopically magnified (40X) MT histology images at asterisks labeled locations in (B): lesion (a1), border (b1), and normal tissue (c1). Corresponding normalized OAPs (a2 – c2) before (blue) and after (pink) HIFU ablation. (D) Amplitude map of ΔF before and 24 s after HIFU ablation, and the percentage difference (ΔAPA) with dashed line representing the same lesion in (B). (E) Maps of APD_{50} before and after HIFU ablation and their percentage difference (ΔAPD_{50}). (F) Maps of APD_{80} before and after HIFU and ΔAPD_{80}. (G) Maps of the ratio between APD_{50} and APD_{80} before and after HIFU ablation, and $\Delta APD_{50}/APD_{80}$. (H) Maps of upstroke rising rate $(d\Delta F/dt)_{max}$ before and after HIFU, and their difference. (I) Activation maps before and after HIFU, and their difference. (J) Conduction velocities (CVs) map before and after HIFU superimposed on the activation maps in (I). Directions of electrical wave propagation and magnitude of CVs are indicated by the directions of the red arrows and their lengths. Zoomed-in local CVs

(right column) around HIFU lesion within the ROI (dashed white boxes) in the global CVs maps (left and middle columns in J).

Suppression of cellular excitability within lesion after HIFU ablation was indicated by a reduction of upstroke rising rate from 0.19 %/ms to 0.11 %/ms. Although no transmural conduction block for the single lesion was seen on activation map, local activation delay up to 5 ms was observed close to the epicardial pacing site and minor early activation (2 ms) occurred in the lesion center. The propagating wavefront bifurcated in the lesion axial direction and increased CVs were seen along the edge of the lesion (Figure 4.8). Bipolar pacing confirmed loss of excitability in lesions (Figure 4.9). No propagating APs were observed when pacing at lesion center, while pacing provoked AP propagation was generated when pacing was near the border of lesion and normal tissue.

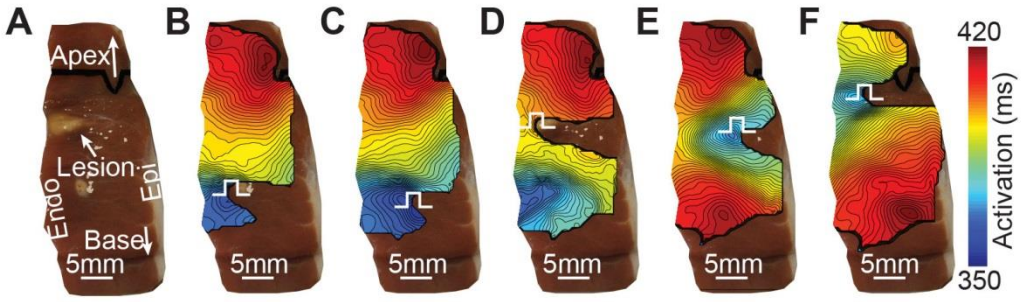

Figure 4.9 Activation maps with pacing at various locations relative to a HIFU lesion. (A) Photograph of a canine LV wedge preparation after HIFU lesion formation with epicardium (Epi) on the right and endocardium (Endo) on the left. Lesion is indicated by the arrow. (B) Activation map superimposed on the LV wedge in (A) before HIFU ablation with pacing placed close to the base of the wedge. (C) Activation map after HIFU ablation with pacing placed below the lesion and close to the base. (D) Activation map after HIFU ablation with pacing placed in the center of the lesion. No electrical activation was provoked from the pacing site whereas spontaneous activation was initiated from earlier pacing site. (E) Activation map after HIFU ablation with pacing at the epicardial side of the lesion, resulting in a reformatted activation pattern. (F) Activation map after HIFU ablation with pacing above the lesion close to apex. Activation was reestablished with origin at the pacing. Pacing threshold was 2X threshold voltage (6V) for all experiments. Isochrones of activation map was separated

with step size of 1 ms with blue representing early activation and red representing late activation. Pacing electrode blocked the view of optical mapping and caused missing areas on all activation maps.

4.3.3 Spatiotemporal Characteristics of AP Changes during HIFU

Baseline changes of fluorescence signals (ΔF) from optical mapping were observed during HIFU ablation (Figure 4.10). CHAPTER 3 determined that such baseline changes correlated with tissue temperature changes induced by HIFU ablation. Analysis of EP changes in this study was performed after baseline drift correction.

In addition to spatial distribution of OAP changes, we observed that OAP exhibited little recovery within the lesion but partial recovery in the lesion border zone after HIFU application. Compared to HIFU induced APA reduction, APD_{50} shortening extended to larger spatial region and occurred faster than ΔAPA during HIFU application (shaded areas in Figure 4.10). Furthermore, less recovery of APA than APD_{50} occurred after HIFU application when tissue gradually cooled down. These observations indicate that plateau potential (related to APD) is more thermally sensitive than excitability (associated with APA and resting membrane potential).

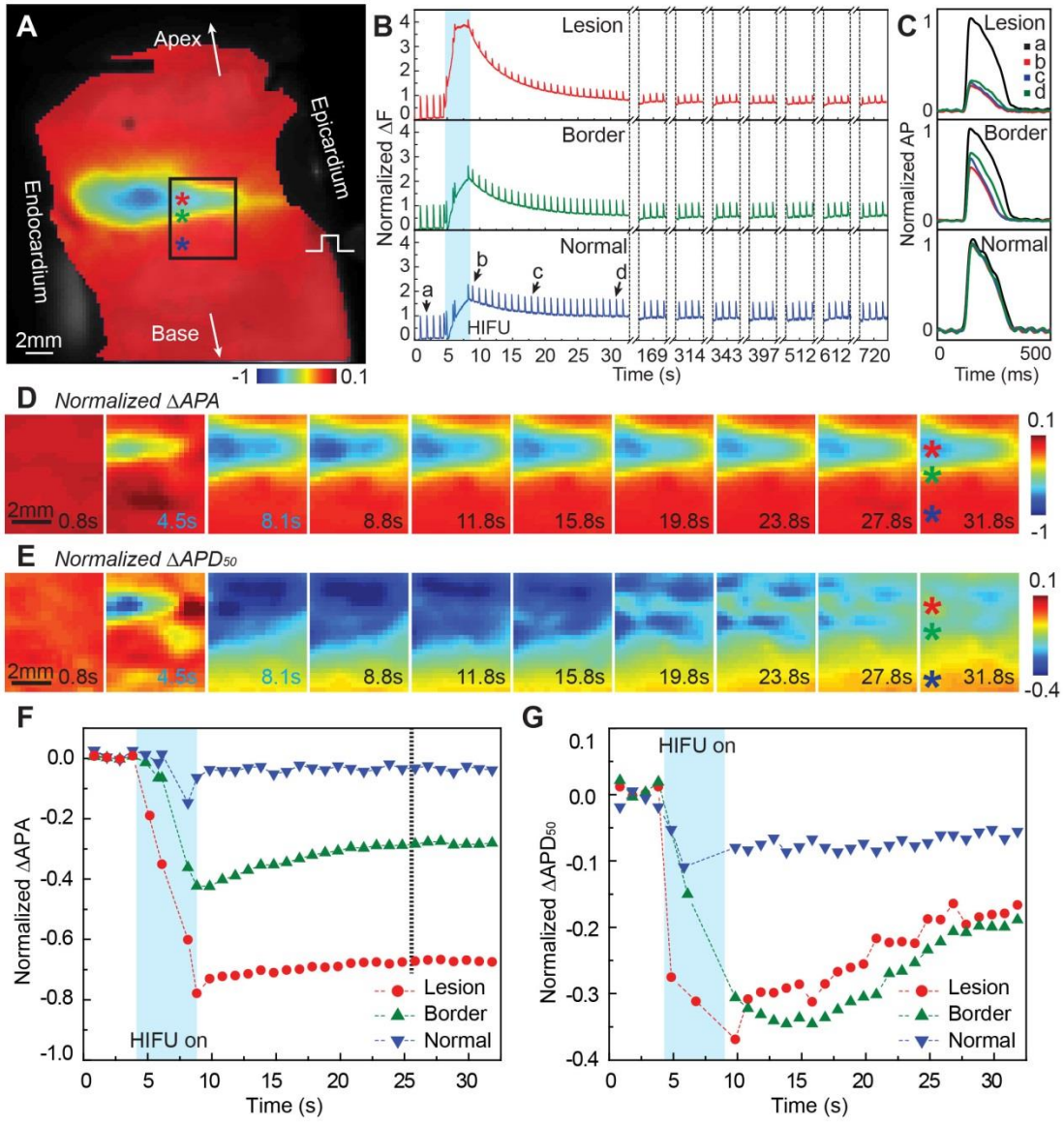

Figure 4.10 Acute changes of AP prior, during, and after HIFU ablation. (A) Changes of OAPs amplitude (ΔAPA) at t = 32 s superimposed on background optical mapping image (gray scale). Black box represents the ROI (6 × 5.6 mm) within the field-of-view of M2D ultrasound imaging. Colored asterisks label representative locations inside lesion, border, and normal tissue. (B) Normalized OAPs at the labeled locations in (A). Cyan shaded area indicates HIFU duration. Single cycle OAPs at t = 1.8, 8.8, 17.8, and 31.8 s indicated by a, b, c, and d. (C) Normalized OAPs at the labeled locations in (A) superimposed at corresponding times (arrows a – d in B). (D) Spatiotemporal changes of ΔAPA. Blue labeled frames were during HIFU ablation. (E) Spatiotemporal changes of ΔAPD_{50}. (F) Normalized ΔAPA and (G) ΔAPD_{50} at representative locations (asterisks in D and E).

4.3.4 HIFU Lesion vs. OAP Changes

We determined the threshold of ΔAPA corresponding to HIFU lesion (Figure 4.11). Based on a lesion mask obtained from gross photograph and MT slide with corresponding ΔAPA map at t = 32 s, histograms of the ΔAPA values at pixel locations inside (n = 2058) or outside lesion mask (m = 4117) (from 13 preparations) show that APA reductions inside lesion (− 0.57 ± 0.16) was significantly higher than outside (− 0.16 ± 0.15) ($p \ll 0.05$). The ROC curves of ΔAPA using all preparations yielded an averaged ROC area-under-curve (AUC) of 0.96 ± 0.01. The optimal threshold of ΔAPA for detecting lesion was − 0.43 ± 0.01 and the corresponding predicted lesion (Figure 4.11, inset) matched precisely with lesion histology. LOO test yielded an ROC AUC of 0.88 ± 0.07, confirming the stability of the detection method.

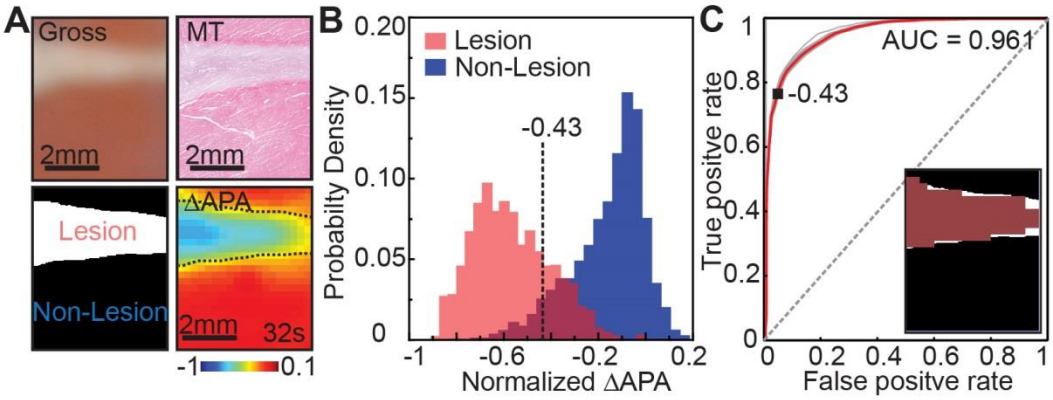

Figure 4.11 OAPs changes within and outside a HIFU lesion. (A) Photograph and masson's trichrome stained slide of a wedge preparation after HIFU ablation (top panel) along with the binary lesion mask (lesion as white) (bottom penal), ΔAPA at t = 32 s. Black dash lines indicate lesion region. (B) ΔAPA (n = 13) within lesion and outside lesion (non-lesion) determined by lesion mask. A black dash line indicates a ΔAPA threshold (- 0.43 ± 0.01) for predicting HIFU lesions determined from receiver-operating characteristic (ROC) analysis. (C) ROC curves for ΔAPA detection of lesion for all cases (individual and overall curves are marked pale and red respectively) with an area under ROC curve (AUC) of 0.961. Inset: ΔAPA predicted lesion (red) for the example in (A) is overlaid on the real binary lesion mask.

4.3.5 Lesion Detection using Optical and Ultrasound Imaging

A clear region of APA reduction was readily identified from optical mapping, but lesion identification was difficult from regular B-mode gray-scale ultrasound images (Figure 4.12).

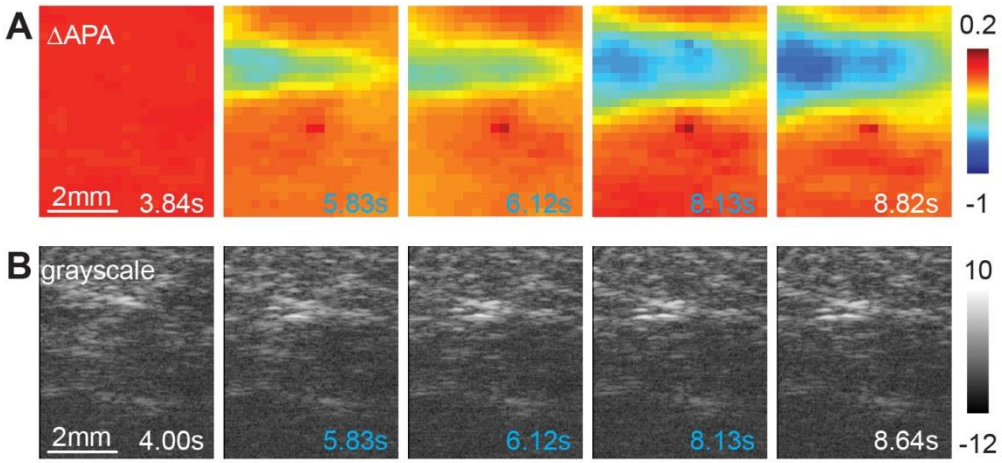

Figure 4.12 Example of optical mapping and ultrasound imaging of lesion growth. (A) Selected ΔAPA maps prior, during, and after HIFU ablation. HIFU ablation was applied from t = 4.55 to 8.55 s. (B) Selected grayscale ultrasound images (from t = 4 to 8.64 s) corresponding to the ΔAPA maps in (A). Frames during HIFU ablation are labeled with blue time indices.

Assuming lesion corresponding to ΔAPA threshold of − 0.43 ± 0.01, parametric images using $|\Delta GS|_{max}$, $|\Delta\alpha|_{max}$, and $|\Delta\sigma|_{max}$ yielded the best AUCs, 0.82 ± 0.03, 0.89 ± 0.02, and 0.89 ± 0.01 respectively (Table 4.1), much better than conventional B-mode (0.53 ± 0.01). The ROC AUCs increased significantly until the end of HIFU application (t = 8 s, n = 4) (Figure 4.13), as detection sensitivity increased correspondingly. Stability of the prediction was confirmed by LOO cross-validation. Since $|\Delta\sigma|_{max}$ generated the highest ROC AUCs (optimal threshold 0.28 ± 0.01), we chose it for our subsequent analysis.

Table 4.1 The area under the receiver-operating characteristic curve (ROC AUC) for detection of lesion from different ultrasound parameters of all canine wedges (n = 13).

Parameter	Symbol	ROC AUC	Threshold
Gray-scale change (tran.) [dB]	$\lvert\Delta GS\rvert_t$	0.53 ± 0.01	5.09 ± 1.84
Gray-scale change (cumu.) [dB]	$\lvert\Delta GS\rvert_c$	0.64 ± 0.03	5.43 ± 1.28
Gray-scale change (cumu. extrm.)	$\lvert\Delta GS\rvert_{max}$	0.82 ± 0.03	0.44 ± 0.16
IBS change (cumu.) [dB]	$\lvert\Delta IBS\rvert_c$	0.65 ± 0.03	10.50 ± 2.10
IBS change (cumu. extrm.)	$\lvert\Delta IBS\rvert_{max}$	0.71 ± 0.06	0.46 ± 0.22
Rayleigh α change (tran.)	$\lvert\Delta\alpha\rvert_t$	0.69 ± 0.04	0.11 ± 0.14
Rayleigh α change (cumu.)	$\lvert\Delta\alpha\rvert_c$	0.77 ± 0.03	0.16 ± 0.03
Rayleigh α change (cumu. extrm.)	$\lvert\Delta\alpha\rvert_{max}$	0.89 ± 0.02	0.11 ± 0.02
Log-normal σ change (tran.)	$\lvert\Delta\sigma\rvert_t$	0.64 ± 0.05	0.12 ± 0.11
Log-normal σ change (cumu.)	$\lvert\Delta\sigma\rvert_c$	0.75 ± 0.01	0.18 ± 0.01
Log-normal σ change (cumu. extrm.)	$\lvert\Delta\sigma\rvert_{max}$	0.89 ± 0.01	0.28 ± 0.01

Based on the ΔAPA threshold (− 0.43 ± 0.01) and $\lvert\Delta\sigma\rvert_{max}$ threshold for lesion identification (0.28 ± 0.01), we constructed color coded parametric images of ΔAPA and $\lvert\Delta\sigma\rvert_{max}$ showing temporal evolution of lesion formation, where lesion region identified from optical mapping (blue) and parametric ultrasound images (red) were superimposed on gray-scale B-mode ultrasound images (Figure 4.13). Compare to ΔAPA, $\lvert\Delta\sigma\rvert_{max}$ imaging overestimated lesion area during the first 2 s of HIFU ablation, but its performance improved significantly and achieved good lesion prediction in the end ($t \approx 8.64$ s).

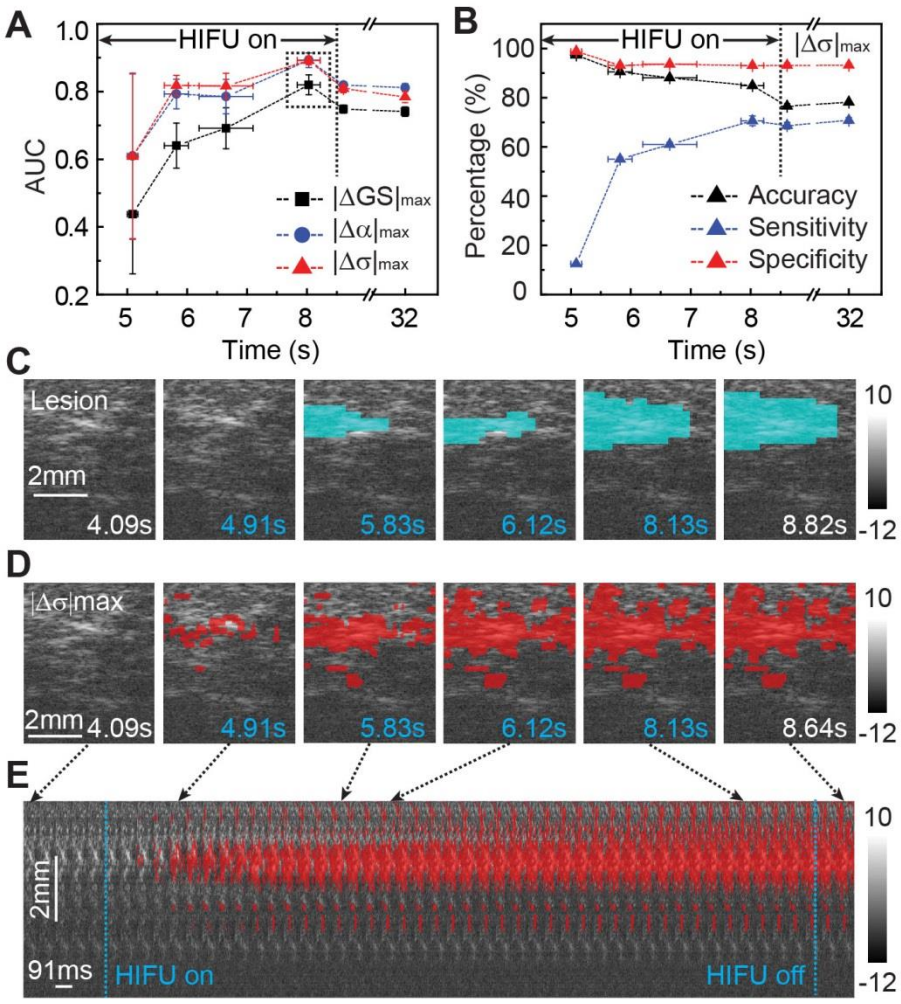

Figure 4.13 Lesion detection using optical mapping and ultrasound imaging. (A) Temporal changes of the ROC area-under-curves (AUCs) for $|\Delta GS|_{max}$ (black), $|\Delta\alpha|_{max}$ (blue), and $|\Delta\sigma|_{max}$ (red), with maximum at t = 8.03 ± 0.19 s (black dash box). (B) Temporal changes of lesion detection accuracy, sensitivity (true positive rate), and specificity (true negative rate) using $|\Delta\sigma|_{max}$. (C) M2D-mode image color-coded by lesion map determined by ΔAPA threshold (cyan). (D) M2D images color-coded by lesion region determined by cumulative extrema of log-normal parameter $|\Delta\sigma|_{max}$ (red). (E) Stacked temporal M2D images superimposed with lesion mask detected by $|\Delta\sigma|_{max}$.

4.3.6 Parametric Ultrasound Imaging vs. ΔAPA

In addition to detecting ΔAPA associated with lesion (< − 0.43), ultrasound distribution parameters α and σ outperformed other parameters in detecting smaller ΔAPA (between − 0.19 and − 0.43) that were not correlated with lesion during HIFU ablation. An arbitrary value − 0.19, significantly above the noise level (− 0.07 ± 0.12), was chosen. Again, the cumulative extrema of the ultrasound parameters yielded higher AUC than transient and cumulative changes. Figure 4.14 shows the ROC AUCs of $|\Delta\sigma|_{max}$ for detecting ΔAPA associated with lesion and non-lesion at different times. Compared with ROC AUC of $|\Delta\sigma|_{max}$ for detecting lesion-related ΔAPA (0.89 ± 0.01), detection of non-lesion ΔAPA achieved an AUC of 0.79 ± 0.03. Similarly, ROC AUCs improved with time, with increasing detection sensitivity correspondingly.

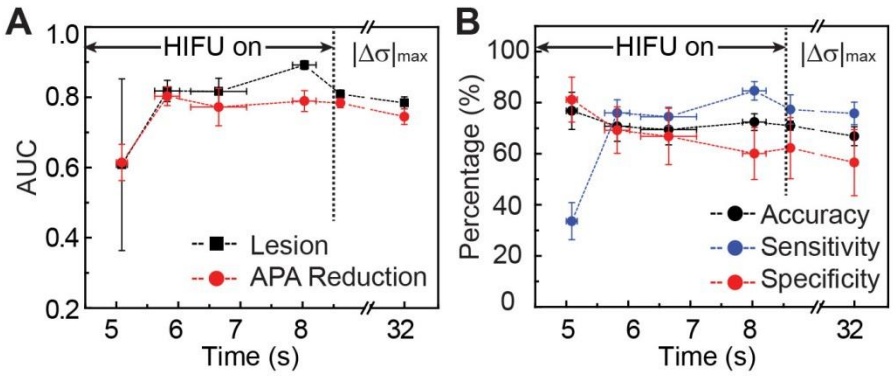

Figure 4.14 Temporal ROC analysis of APA detection using parametric ultrasound imaging. (A) Temporal changes of the ROC area-under-curves (AUCs) using $|\Delta\sigma|_{max}$ for detecting lesion and ΔAPA below lesion threshold (non-lesion). (B) Temporal changes of detection accuracy, sensitivity (true positive rate), and specificity (true negative rate) using cumulative extrema of log-normal parameter ($|\Delta\sigma|_{max}$) for detection of lesion and peripheral ΔAPA regions.

Figure 4.15A shows an example of color coded ΔAPA images for lesion (ΔAPA < – 0.43) in blue and non-lesion regions (– 0.19 < ΔAPA < – 0.43) in green.

Figure 4.15B – C is the color coded $|\Delta\sigma|_{max}$ images for detecting ΔAPA within lesion (red) and non-lesion (yellow), with overestimation of areas associated with non-lesional ΔAPA.

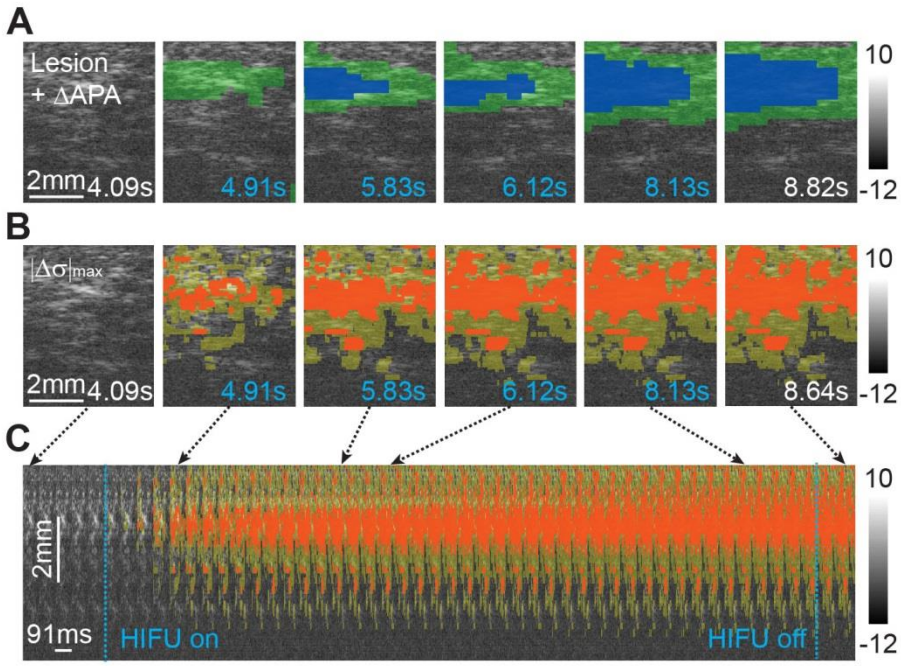

Figure 4.15 Example of APA detection using ultrasound parametric imaging. (A) M2D image color coded by true lesion region (ΔAPA < - 0.43, blue) and non-lesional ΔAPA (- 0.43 < ΔAPA < - 0.19, green) determined from ΔAPA maps. (B) Gray-scale M2D images color coded with lesion (red) and non-lesional ΔAPA (yellow) regions determined from $|\Delta\sigma|_{max}$ images. Blue time indices indicate frames during HIFU application. (C) Stacked temporal M2D images coded with lesion and non-lesional ΔAPA masks detected by $|\Delta\sigma|_{max}$.

4.4 Discussion

Using optical mapping and ultrasound imaging, we investigated HIFU induced tissue and EP changes transmurally in a spatiotemporally correlated fashion in perfused canine wedge preparations. We demonstrated that

parametric ultrasound imaging using cumulative extrema of the log-normal scale parameter σ ($|\Delta\sigma|_{max}$) can differentiate HIFU generated lesion and small ΔAPA around the thermal lesions. To note, the proposed imaging technique, which is potentially useful for intra-operative identification of lesion transmurality, can be applied in other ablation modalities such as RF and laser ablation as well, and can help improve the efficacy of current ablation procedure in clinical practice.

4.4.1 Spatiotemporal Changes of APA and APD around Lesions

Our results of the spatiotemporal changes of EP induced by HIFU ablation, such as reduction of APA and shortening of APD, in the transmural surface of the wedge preparations are in general agreement with the reported EP data recorded epicardially and intracardially.[23,29,30] Although HIFU generated lesion and EP changes in our study showed similar properties to RF lesions, several findings are worth noting.

Significant reduction in electrogram amplitude (e.g. 80 %) has been used clinically[31] to confirm ablation. However, no universal endpoint for single ablation has been well defined. In this study, we determined a threshold of ΔAPA (43 ± 1 %, n = 13) that best demarked single lesion region validated by histology. The more conservative reduction may be necessary clinically to reduce the risk of electrical reconnection.

Shortening of APD_{50} and APD_{80} extended beyond the lesion boundary (Figure 4.8 and Figure 4.10), as well as triangulation, consistent with the reported results using RF ablation.[23] APD_{50} and APD_{80} occurred faster than and prior to APA reduction (Figure 4.8 and Figure 4.10), and there was also larger recovery of APD than APA after HIFU application during tissue cooling, suggesting a more thermally sensitive characteristics of the ion channels (thus plateau potentials)

than cell excitability and a more stable measurement of EP changes using APA instead of APD. In addition, less reduction in APD_{80} compared to APD_{50}, firstly reported by Wood *et al*. in RF ablation[23], was also observed in HIFU lesion. Triangulation was < 20 % within lesion and on lesion border zone (Figure 4.8). Possible mechanisms include suppression of L-type Ca^{2+} current, delayed outward K^+ current, and inward rectifier K^+ current when temperature across certain threshold.

Optical mapping in a transmural surface revealed early activation within the HIFU lesion and local activation delay at locations proximal to pacing site, suggesting the effect of the intricate alignment of myocardial fibers across the transmural ventricular wall. Conduction velocities increased along the edges of HIFU lesions, similar to the observations in RF lesions.[23,32]

4.4.2 Lesion Assessment using Ultrasound Imaging

Superior tissue penetration of ultrasound imaging compared to other imaging methods such as endoscopy or optical coherent tomography makes it a suitable tool for real time transmural monitoring of lesion formation, as observed in ablation in an *in vivo* sheep model.[16] However, conventional ultrasound imaging has not provided sufficient contrast to detect lesions accurately.

Eyerly *et al.* demonstrated an novel ICE base ARFI imaging technique using a 6.15 MHz imaging probe for identifying RF generated lesions and discontinuous lesion set.[20] But the imaging rate of ARFI was less than 4 frames/min and the imaging quality was affected by the probe placement and cardiac motions. Wright *et al.* introduced a novel system that combined ultrasound imaging with ring or polymethylpentene (TPX) covered RF catheters to directly visualize lesion formation in real time.[16] We have previously shown

that high frequency ultrasound imaging at 55 MHz combined with fast frame rate M-mode (1 kHz)[19] and short time B-mode (STBM) (frame rate 70 – 130 Hz)[18] imaging can detect HIFU lesion and gas body formation by tracking the temporal history of changes in ultrasound integrated backscatter (*IBS*) and frame-to-frame echo decorrelation. In the current study, we employed lower ultrasound imaging frequency at 30 MHz with a deeper imaging depth (~12.7 mm) which is more suitable for imaging across the depth of human atrial tissue (5 – 7 mm). Using the ΔAPA threshold corresponding to the histological lesion, we showed that statistical parameters such as Rayleigh and log-normal parameters performed better than the parameters employed previously in predicting lesion formation and sizes.

Both Rayleigh and Non-Rayleigh (e.g. K-distribution and Nakagami parameters) distribution methods have been employed to differentiate infarcted myocardium from normal heart in studies using imaging frequency below 15 MHz.[27,33] In this study, we showed that statistical parameters such as Rayleigh and log-normal parameters performed better than other parameters, suggesting the ultrasound scatters (e.g. cell nucleus) within HIFU lesions were most likely poly-dispersed and non-periodic.[34] However, the detection accuracies between Rayleigh and Nakagami method were marginal. The cumulative extrema of the parameters, which captured the temporal evolution of the backscatter changes during HIFU ablation, performed better than transient and cumulative changes. For example, ROC AUC increased by 20 % using cumulative extrema of $|\Delta\sigma|$. In addition, the spatial resolution with Rayleigh and log-normal imaging was fine enough to image small size lesions (98 μm in axial and 115 μm in lateral), although slightly lower than the resolution of using grayscale and IBS (55 × 115 μm).

4.4.3 Ultrasound Imaging of APA Changes

Our results show that histological lesion regions matched well with spatial map of APA reduction above a threshold (Figure 4.8), suggesting a link of cell morphological damage (e.g. loss of cellular nuclei, myocardial fiber dissolution, damaged plasma membrane and gap junctions) (Figure 4.8C) with cellular EP changes including the loss of AP and inter-cellular electrical conductivity.[35]

Although it is the significant irreversible ΔAPA combined with lesion that is relevant for intra-operative ablation guidance, it is also important to gauge smaller changes of APA because Wood *et al.* observed that cellular EP within lesion border zone completely recovered 22 ± 13 days after RF ablation,[23] which may be responsible for arrhythmia recurrence. We demonstrated that parametric ultrasound imaging can accurately detect lesion thus irreversible changes of APA during HIFU ablation and also smaller APA changes although with less accuracy.

4.4.4 Experimental Limitations

In vitro preparations of canine ventricular wedges that are mechanically stabilized using BDM have inherent physiological differences from *in vivo* beating hearts. A more appropriate decoupler, blebistatin which has less side-effect on cellular EP than BDM[36], should be used. In this study, ultrasound imaging and optical mapping were performed on the same transmural tissue surface of a wedge preparation, which may be different from a transmural plane within a 3D tissue. Optical mapping provides relative AP values and can only be used for *in vitro* study. Since we used a 30 MHz imaging system for high spatial

imaging resolution, to extrapolate this to *in vivo* implementation for ablation monitoring, further studies will be required to examine the effects of imaging frequency, imaging beam characteristics, as well as ECG-gating for motion tracking to suit for beating heart conditions. As a preclinical proof-of-principle study, we were able to image the lesion and AP changes on the ablation plane parallel to the ablation axis along tissue depth direction. Ideally, ultrasound imaging transducer shall be co-axially aligned with ablation probe as Wright *et al*. presented earlier[16], therefore, further efforts are needed to fabricate dual-element transducers for co-axial ablation and imaging. Furthermore, the temperature during ablation was not monitored directly, thereby whether ablation induced "boiling" occurred and the effects of gas body activities and cavitation on the performance of the parametric imaging techniques for lesion and EP detection were not fully investigated.

4.5 References

1. Roger VL, Go AS, Lloyd-Jones DM, Benjamin EJ, Berry JD, et al. Heart disease and stroke statistics--2012 update: A report from the american heart association. Circulation. 2012;125:e2-e220
2. Morady F. Radio-frequency ablation as treatment for cardiac arrhythmias. N Engl J Med. 1999;340:534-544
3. Cappato R, Calkins H, Chen SA, Davies W, Iesaka Y, et al. Worldwide survey on the methods, efficacy, and safety of catheter ablation for human atrial fibrillation. Circulation. 2005;111:1100-1105
4. Kobza R, Hindricks G, Tanner H, Schirdewahn P, Dorszewski A, et al. Late recurrent arrhythmias after ablation of atrial fibrillation: Incidence, mechanisms, and treatment. Heart Rhythm. 2004;1:676-683

5. Miyagi Y, Ishii Y, Nitta T, Ochi M, Shimizu K. Electrophysiological and histological assessment of transmurality after epicardial ablation using unipolar radiofrequency energy. J Card Surg. 2009;24:34-40

6. Perez FJ, Wood MA, Schubert CM. Effects of gap geometry on conduction through discontinuous radiofrequency lesions. Circulation. 2006;113:1723-1729

7. Ouyang F, Antz M, Ernst S, Hachiya H, Mavrakis H, et al. Recovered pulmonary vein conduction as a dominant factor for recurrent atrial tachyarrhythmias after complete circular isolation of the pulmonary veins: Lessons from double lasso technique. Circulation. 2005;111:127-135

8. Melby SJ, Lee AM, Zierer A, Kaiser SP, Livhits MJ, et al. Atrial fibrillation propagates through gaps in ablation lines: Implications for ablative treatment of atrial fibrillation. Heart Rhythm. 2008;5:1296-1301

9. Lardo AC, McVeigh ER, Jumrussirikul P, Berger RD, Calkins H, et al. Visualization and temporal/spatial characterization of cardiac radiofrequency ablation lesions using magnetic resonance imaging. Circulation. 2000;102:698-705

10. Marrouche NF, Martin DO, Wazni O, Gillinov AM, Klein A, et al. Phased-array intracardiac echocardiography monitoring during pulmonary vein isolation in patients with atrial fibrillation: Impact on outcome and complications. Circulation. 2003;107:2710-2716

11. Vaseghi M, Cesario DA, Valderrabano M, Boyle NG, Ratib O, et al. Impedance monitoring during catheter ablation of atrial fibrillation. Heart Rhythm. 2005;2:914-920

12. Langberg JJ, Calkins H, el-Atassi R, Borganelli M, Leon A, et al. Temperature monitoring during radiofrequency catheter ablation of accessory pathways. Circulation. 1992;86:1469-1474

13. Yokoyama K, Nakagawa H, Shah DC, Lambert H, Leo G, et al. Novel contact force sensor incorporated in irrigated radiofrequency ablation catheter predicts lesion size and incidence of steam pop and thrombus. Circ Arrhythm Electrophysiol. 2008;1:354-362

14. Reddy VY, Neuzil P, Themistoclakis S, Danik SB, Bonso A, et al. Visually-guided balloon catheter ablation of atrial fibrillation: Experimental feasibility and first-in-human multicenter clinical outcome. Circulation. 2009;120:12-20

15. Fleming CP, Wang H, Quan KJ, Rollins AM. Real-time monitoring of cardiac radio-frequency ablation lesion formation using an optical coherence tomography forward-imaging catheter. J Biomed Opt. 2010;15:030516

16. Wright M, Harks E, Deladi S, Suijver F, Barley M, et al. Real-time lesion assessment using a novel combined ultrasound and radiofrequency ablation catheter. Heart Rhythm. 2011;8:304-312

17. Kolios MC, Czarnota GJ, Lee M, Hunt JW, Sherar MD. Ultrasonic spectral parameter characterization of apoptosis. Ultrasound Med Biol. 2002;28:589-597

18. Gudur MS, Kumon RE, Zhou Y, Deng CX. High-frequency rapid b-mode ultrasound imaging for real-time monitoring of lesion formation and gas body activity during high-intensity focused ultrasound ablation. IEEE Trans Ultrason Ferroelectr Freq Control. 2012;59:1687-1699

19. Kumon RE, Gudur MS, Zhou Y, Deng CX. High-frequency ultrasound m-mode imaging for identifying lesion and bubble activity during high-intensity focused ultrasound ablation. Ultrasound Med Biol. 2012;38:626-641

20. Eyerly SA, Bahnson TD, Koontz JI, Bradway DP, Dumont DM, et al. Intracardiac acoustic radiation force impulse imaging: A novel imaging method for intraprocedural evaluation of radiofrequency ablation lesions. Heart Rhythm. 2012;9:1855-1862

21. Glukhov AV, Fedorov VV, Lou Q, Ravikumar VK, Kalish PW, et al. Transmural dispersion of repolarization in failing and nonfailing human ventricle. Circ Res. 2010;106:981-991

22. Di Diego JM, Sicouri S, Myles RC, Burton FL, Smith GL, Antzelevitch C. Optical and electrical recordings from isolated coronary-perfused ventricular wedge preparations. J Mol Cell Cardiol. 2013;54:53-64

23. Wood MA, Fuller IA. Acute and chronic electrophysiologic changes surrounding radiofrequency lesions. J Cardiovasc Electrophysiol. 2002;13:56-61

24. Libbus I, Wan X, Rosenbaum DS. Electrotonic load triggers remodeling of repolarizing current ito in ventricle. Am J Physiol Heart Circ Physiol. 2004;286:H1901-1909

25. Voss F, Opthof T, Marker J, Bauer A, Katus HA, Becker R. There is no transmural heterogeneity in an index of action potential duration in the canine left ventricle. Heart Rhythm. 2009;6:1028-1034

26. Parsons JE, Cain CA, Fowlkes JB. Cost-effective assembly of a basic fiber-optic hydrophone for measurement of high-amplitude therapeutic ultrasound fields. J Acoust Soc Am. 2006;119:1432-1440

27. Clifford L, Fitzgerald P, James D. Non-rayleigh first-order statistics of ultrasonic backscatter from normal myocardium. Ultrasound Med Biol. 1993;19:487-495

28. Fishbein MC, Meerbaum S, Rit J, Lando U, Kanmatsuse K, et al. Early phase acute myocardial infarct size quantification: Validation of the triphenyl tetrazolium chloride tissue enzyme staining technique. Am Heart J. 1981;101:593-600

29. Ge YZ, Shao PZ, Goldberger J, Kadish A. Cellular electrophysiological changes induced in vitro by radiofrequency current: Comparison with electrical ablation. Pacing Clin Electrophysiol. 1995;18:323-333

30. Wu CC, Fasciano RW, 2nd, Calkins H, Tung L. Sequential change in action potential of rabbit epicardium during and following radiofrequency ablation. J Cardiovasc Electrophysiol. 1999;10:1252-1261

31. Pappone C, Rosanio S, Oreto G, Tocchi M, Gugliotta F, et al. Circumferential radiofrequency ablation of pulmonary vein ostia: A new anatomic approach for curing atrial fibrillation. Circulation. 2000;102:2619-2628

32. Chorro FJ, Sanchis J, Such L, Garcia-Civera R, Llavador E, et al. Acute effects of radiofrequency ablation upon atrial conduction in proximity to the lesion site. Pacing Clin Electrophysiol. 1998;21:659-668

33. Hao X, Bruce CJ, Pislaru C, Greenleaf JF. Characterization of reperfused infarcted myocardium from high-frequency intracardiac ultrasound imaging using homodyned k distribution. IEEE Trans Ultrason Ferroelectr Freq Control. 2002;49:1530-1542

34. Saha RK, Kolios MC. Effects of cell spatial organization and size distribution on ultrasound backscattering. IEEE Trans Ultrason Ferroelectr Freq Control. 2011;58:2118-2131

35. Nath S, Redick JA, Whayne JG, Haines DE. Ultrastructural observations in the myocardium beyond the region of acute coagulation necrosis following radiofrequency catheter ablation. J Cardiovasc Electrophysiol. 1994;5:838-845

36. Fedorov VV, Lozinsky IT, Sosunov EA, Anyukhovsky EP, Rosen MR, et al. Application of blebbistatin as an excitation-contraction uncoupler for electrophysiologic study of rat and rabbit hearts. Heart Rhythm. 2007;4:619-626

CHAPTER 5

Conclusions and Future Works

This dissertation has demonstrated the feasibility of using optical mapping technique to investigate HIFU thermal effects on cardiac cellular electrophysiology (EP). EP changes during HIFU are characterized and correlated with temperature measurements. Detailed spatiotemporal EP-temperature correlation enhances our understanding about HIFU cardiac ablation. The demonstrated HIFU-temperature dosage information will hopefully provide valuable information for planning HIFU cardiac ablation and designing temperature feedback schemes. Ultrasound parametric imaging techniques developed in this work provide a new prospect of imaging lesion and action potential changes simultaneously during HIFU ablation. Combined, this work may help increase the safety and efficacy of HIFU ablation and advance the application of the HIFU technology in cardiac ablation. Future work in HIFU technique will focus on developing safe HIFU ablation technique to reduce HIFU related complications and to explore other potential effects of therapeutic ultrasound on cardiac EP. This chapter aims to summarize and combine the findings of this work, and provide future research scopes.

5.1 Conclusions

In this dissertation, three specific aims are achieved. First, we successfully demonstrated using optical mapping to continuously monitor HIFU induced cardiac EP changes in Langendorff-perfused rabbit whole heart model in real time. The details described in CHAPTER 2 build the methodological foundation to carry out experiments in the rest studies.

By combining infrared imaging, we then systematically explored the spatiotemporal correlation between HIFU induced EP changes and corresponding temperature increases during and following HIFU ablation in CHAPTER 3. We find cardiac EP changes during HIFU application are predominantly thermal mediated. HIFU-generated APA reduction, APD shortening, activation distortion, and local conduction velocities increases are temperature dependent: temperature below 50.1 ± 0.8 °C only lead to reversible EP changes while temperature above 52.3 ± 1.4 °C can induce irreversible tissue physical and EP changes. Temperature thresholds for generating APA reductions are > 42.7 ± 0.1 °C and > 39.6 ± 0.1 °C for causing APD shortening, confirming the hypothesis that APD is more thermal sensitive than APA. Compounding both tissue histopathology and EP, we find an ablation transition zone which can help explain electrical reconnection in clinical ablation. Major vessels related to the "heat sink" effect can also compromise the efficacy of HIFU ablation. These results help derive the temperature dosage information that is necessary for achieving irreversible EP changes during HIFU ablation and also point out the importance of temperature monitoring during HIFU ablation. Further efforts are needed to develop robust temperature monitoring scheme to improve the efficacy of HIFU ablation. Unfortunately, we did not develop specific HIFU

ablation sequences (e.g. intensity values, pulse duration, duty cycle, and etc.) to achieve permanent EP damage and tissue lesioning.

Finally, we developed ultrasound parametric imaging technique to monitor HIFU ablation in terms of tissue physical and action potential changes in CHAPTER 4. The specific imaging scheme is able to provide feedbacks along the ablation axial direction in the subsurface tissue layers, thereby, becoming a promising technique to monitor the lesion transmurality, which is critically important in ablation of AF. One advantage of the proposed imaging technique is its ability to identify the tissue area susceptible for electrical reconduction which is a major cause of recurrence of AF. However, implementation of the parametric imaging technique in real time at lower ultrasound imaging frequencies that is more appropriate in clinical needs to be tested in future.

5.2 Future Works

5.2.1 In-vivo Implementation of Ultrasound Imaging Technique

In the dissertation (CHAPTER 4), we demonstrated using parametric ultrasound imaging to monitor HIFU generated lesion and EP changes. Real-time feedback during ablation (e.g. RF, HIFU) is imperative. Neven *et al.* have demonstrated PVI using HIFU could cause severe complications such as atrial-esophageal fistula (AEF) which can be lethal.[1,2] Esophageal temperature monitoring algorithm during HIFU ablation has been proved ineffective to avoid AEF.[2] However, esophagus temperature monitoring combined with echocardiography during RF ablation can effectively reduce the incidence of AEF in clinical.[3]

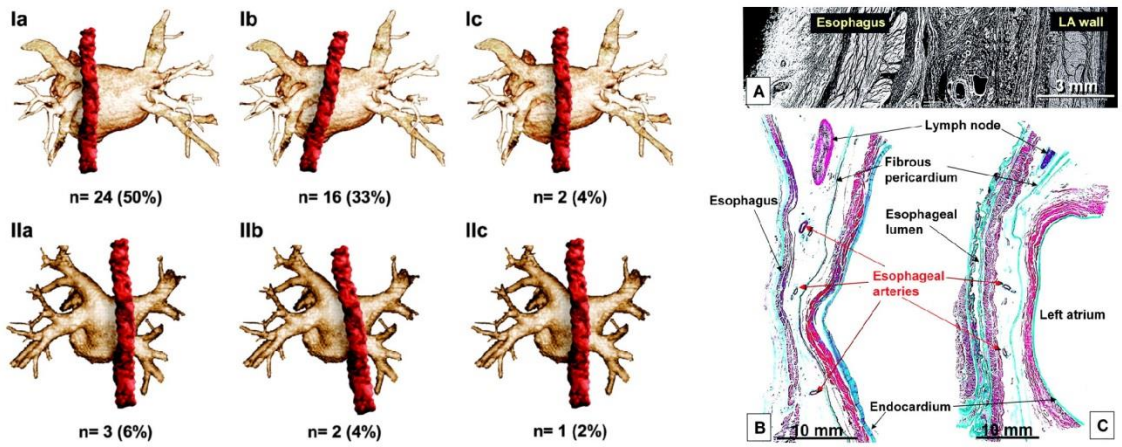

Figure 5.1 Anatomic relationship between the esophagus and left atrium. Major and subtypes of esophagus-posterior LA free wall relationship. (Left) SEM and masson's trichrome stained esophagus-LA wall sagittal sections. (Right). Copyrights © American College of Chest Physicians[4] and American Heart Association[5].

Figure 5.1 shows the anatomic relationship between an esophagus and posterior left atrium free wall. The distance between left atrium (the major target of PVI during catheter ablation) and esophageal wall appears to be around 10 mm. In CHAPTER 4, we employed a 30 MHz ultrasound imaging probe with an imaging depth ~ 12.7 mm. Thereby, it is feasible to implement the parametric ultrasound imaging technique in *in vivo* circumstances to monitor RF or HIFU generated lesion in real time. By combining with ultrasound thermography or gas body detection algorithm[6,7], the ablation process can be well monitored and the risks of AEF will be significantly lowered. If the trans-esophageal route was adopted, imaging-ablation sequences must be precisely synchronized to reduce detection error. Since current trans-esophageal echocardiography (TEE) system typically uses imaging frequency between 3.5 – 7 MHz, the detection accuracy using the proposed image algorithm may be compromised due to lowered imaging frequency. However, because single lesions with diameters within 5 – 10 mm are typically used in clinical setting, it may be possible to detect lesion at

lower frequency without significant loss of detection accuracy. Further investigations are needed to explore the relationship between imaging frequency and the accuracy of lesion detection algorithm.

Since current minimal invasive ablation techniques are mostly catheter based, another more promising method is the catheter-based ultrasound imaging system similar to the settings proposed by Wright *et al*[8]. High imaging frequency (e.g. > 30 MHz), which provide better imaging resolution, can be achieved. In addition to lesion detection, ultrasound imaging can be used for temperature estimation. Therefore, simultaneously two dimensional temperature monitoring and assessment of lesion transmurality can be realized in real time during ablation procedure, particularly for ablation of scar-related ventricular tachycardia or atrial tachycardia originating from relatively thick portions of the left atrium. Further efforts are needed to fabricate ultrasound imaging transducers compatible with current ablation energies such RF, microwave, laser, and HIFU to be able to provide accurate imaging feedback about lesion transmurality and to avoid overheating related complications such as perforation and esophagus injury. For such system, ECG or respiratory gated algorithm is necessary to reduce motion related false detection.

5.2.2 Effect of Ultrasound Radiation Force on Cellular EP

In CHAPTER 1, we have learnt two different ultrasonic effects can be used for therapeutic purposes: thermal effect (ablation) and mechanical effect (acoustic cavitation). Another interesting effect of ultrasound is radiation force, a type of ultrasound mechanical effect which is the net force exerted on tissue and shows the ability to displace the tissue away from its steady state position. It has been employed for remote tissue compression in acoustic elasticity imaging (e.g.

acoustic radiation force impulse [ARFI] imaging).[9,10] Dalecki *et al.* did several pioneer works regarding the ultrasound induced premature ventricular contractions (PVC).[11-13] Pulsed ultrasound energy was applied on murine hearts and the major effect for generating PVC was found to be acoustic radiation force.[14] However, the detailed electrophysiological mechanism of ultrasound induced PVC is still unclear. Using the combined ultrasound and optical mapping system described in CHAPTER 2, we can investigate ultrasound radiation force generated cardiac EP changes spatiotemporally in real time in 2D.

5.2.3 Sonoporation and Cardiac EP Responses

Microbubbles under the excitation of ultrasound waves can generate transient pores on the membrane of adjacent cells, and this is defined as sonoporation. Research has demonstrated calcium influx was generated when cell membrane was sonoporated by ultrasound.[15] For cardiac cells, calcium channel kinetics play a critical role in regulating membrane potentials. Specifically, L-type Ca^{2+} channels were proved to affect cardiac action potential plateau phase.[16] Theoretically, by sonoporating the cell membrane, calcium influx can be generated, leading to changes of cellular membrane potentials. If periodic ultrasound exposure was generated, the rhythm of cardiomyocytes excitation can be potentially "controlled". Using ultrasound contrast agent during echocardiography, premature ventricular arrhythmias (PVA) were observed when the microbubbles were excited by ultrasound energy.[17-19] Therefore, we can use optical mapping technique to monitor sonoporation generated cardiac EP changes in a whole heart model. The mechanism of sonoporation related PVA can be revealed using proposed method in CHAPTER 2. Furthermore, using

periodic ultrasound exposures, cardiac arrhythmias can be potentially corrected using a sonoporation-based method.

5.3 References

1. Neven K, Metzner A, Schmidt B, Ouyang F, Kuck KH. Two-year clinical follow-up after pulmonary vein isolation using high-intensity focused ultrasound (hifu) and an esophageal temperature-guided safety algorithm. Heart Rhythm. 2012;9:407-413

2. Neven K, Schmidt B, Metzner A, Otomo K, Nuyens D, et al. Fatal end of a safety algorithm for pulmonary vein isolation with use of high-intensity focused ultrasound. Circ Arrhythm Electrophysiol. 2010;3:260-265

3. Mackensen GB, Hegland D, Rivera D, Adams DB, Bahnson TD. Real-time 3-dimensional transesophageal echocardiography during left atrial radiofrequency catheter ablation for atrial fibrillation. Circ Cardiovasc Imaging. 2008;1:85-86

4. Tsao HM, Wu MH, Higa S, Lee KT, Tai CT, et al. Anatomic relationship of the esophagus and left atrium: Implication for catheter ablation of atrial fibrillation. Chest. 2005;128:2581-2587

5. Sanchez-Quintana D, Cabrera JA, Climent V, Farre J, Mendonca MC, Ho SY. Anatomic relations between the esophagus and left atrium and relevance for ablation of atrial fibrillation. Circulation. 2005;112:1400-1405

6. Gudur MS, Kumon RE, Zhou Y, Deng CX. High-frequency rapid b-mode ultrasound imaging for real-time monitoring of lesion formation and gas body activity during high-intensity focused ultrasound ablation. IEEE Trans Ultrason Ferroelectr Freq Control. 2012;59:1687-1699

7. Liu D, Ebbini ES. Real-time 2-d temperature imaging using ultrasound. IEEE Trans Biomed Eng. 2010;57:12-16

8. Wright M, Harks E, Deladi S, Suijver F, Barley M, et al. Real-time lesion assessment using a novel combined ultrasound and radiofrequency ablation catheter. Heart Rhythm. 2011;8:304-312

9. Dalecki D. Mechanical bioeffects of ultrasound. Annu Rev Biomed Eng. 2004;6:229-248

10. Eyerly SA, Bahnson TD, Koontz JI, Bradway DP, Dumont DM, et al. Intracardiac acoustic radiation force impulse imaging: A novel imaging method for intraprocedural evaluation of radiofrequency ablation lesions. Heart Rhythm. 2012;9:1855-1862

11. Dalecki D, Keller BB, Carstensen EL, Neel DS, Palladino JL, Noordergraaf A. Thresholds for premature ventricular contractions in frog hearts exposed to lithotripter fields. Ultrasound Med Biol. 1991;17:341-346

12. Dalecki D, Raeman CH, Carstensen EL. Effects of pulsed ultrasound on the frog heart: Ii. An investigation of heating as a potential mechanism. Ultrasound Med Biol. 1993;19:391-398

13. Dalecki D, Keller BB, Raeman CH, Carstensen EL. Effects of pulsed ultrasound on the frog heart: I. Thresholds for changes in cardiac rhythm and aortic pressure. Ultrasound Med Biol. 1993;19:385-390

14. Dalecki D, Raeman CH, Child SZ, Carstensen EL. Effects of pulsed ultrasound on the frog heart: Iii. The radiation force mechanism. Ultrasound Med Biol. 1997;23:275-285

15. Fan Z, Kumon RE, Park J, Deng CX. Intracellular delivery and calcium transients generated in sonoporation facilitated by microbubbles. J Control Release. 2010;142:31-39

16. Lopez-Lopez JR, Shacklock PS, Balke CW, Wier WG. Local calcium transients triggered by single l-type calcium channel currents in cardiac cells. Science. 1995;268:1042-1045

17. Miller DL, Dou C, Lucchesi BR. Are ecg premature complexes induced by ultrasonic cavitation electrophysiological responses to irreversible cardiomyocyte injury? Ultrasound Med Biol. 2011;37:312-320

18. Miller DL, Dou C, Lucchesi BR. Cardiac arrhythmia and injury induced in rats by burst and pulsed mode ultrasound with a gas body contrast agent. J Ultrasound Med. 2009;28:1519-1526

19. Miller DL, Li P, Dou C, Armstrong WF, Gordon D. Evans blue staining of cardiomyocytes induced by myocardial contrast echocardiography in rats:

Evidence for necrosis instead of apoptosis. Ultrasound Med Biol. 2007;33:1988-1996

APPENDIX

Langendorff Rabbit Experimental Procedural

Preparation of Experiment

1. Prepare Tyrode's solution as described in the recipe. Stock solution can be stored in 4 °C refrigerator to avoid repetitive preparation before each experiment.

2. After preparation of Tyrode's solution, add in excitation-contraction decoupler 15 mM BDM (~3 g) in every 2 L Tyrode's solution for the perfusion and superfusion circulation. Prepare VSD di-4-ANEPPS stock solution (5 mg dissolved in 5 ml DMSO). Single rabbit heart typically require three 2L Tyrode's solution (2 for perfusion and superfusion, 1 for dissection process) and roughly 30 μL di-4-ANEPPS stock solution.

3. Prepare circulation stages and monitoring equipment. Warm up all Tyrode's solutions at 37 °C via water bath and connect the container to the Langendorff circulation system. Oxygenate the Tyrode's solution (95 % O_2/5 % CO_2) and keep monitoring the pH value. The pH value can be adjusted through adjustment of the speed of oxygenation (increase O_2 tends to lower the pH) and keep pH value close to 7.35. Begin the circulation and the solution is filtered through a nylon net filter (NY1104700, EMD Millipore, Billerica, MA,

USA) and set up monitoring equipment (pressure monitoring, ECG monitoring).

Rabbit Heart Harvesting

1. Before harvesting the heart, transfer rough 250 ml warmed and oxygenated Tyrode's solution into a small container. Add 0.2 ~ 0.5 ml Heparin solution in the container, which will be used for transporting the heart from surgery stage to the Langendorff system.

2. The anesthesia and euthanasia procedure follows a protocol approved by UCUCA at University of Michigan. First anesthetize the rabbit through intramuscular injection of 0.7 ml Xylazine and 0.5 ml Ketamine. The rabbit will be anesthetized after 2 – 3 mins. Catheterize the marginal ear vein and inject 1 ml Heparin (1000 U/kg). Two minutes later, inject 1 ml sodium pentobarbital (100 mg/kg) for euthanasia. The rabbit is euthanized immediately which can be confirmed through pain reflex test. Median sternotomy is performed immediately and the heart is excised and kept in the transportation Tyrode's solution.

3. Quickly cut the aorta along ascending direction right before the first branch of aortic arch. Immediately cannulate the heart using a 16-gauge cannula which is connected to a bubble trapper. Tight the heart with the cannula using suture and start perfusion of a non-recirculating Langendorff system (dissection stage) while keep aortic pressure at 60 – 80 mmHg.

4. Open the pericardium quickly to avoid cardiac tamponade. Cut off the peripheral tissue (e.g. lungs, fat, thyroid, and trachea). Cut open the pulmonary artery which is close to the aorta.

5. Blood trapped in the heart is flushed out. Move the heart to the recirculating Langendorff system by connecting cannula to perfusion inlet and prepare for HIFU ablation and optical mapping. Adjust the pump speed to keep the aortic pressure stable (60 – 80 mmHg). Place the floating ECG needle electrodes to mimic the Lead I and II of the Einthoven triangle ECG.

Focusing HIFU Transducer

1. Move the heart holder such that the intact rabbit heart is in the middle of the tissue chamber. Rotate the heart to let the desired ablation region face the HIFU transducer and wait the heart to stabilize.

2. Connect the HIFU transducer with an electrical pulser-receiver which is connected to an oscilloscope. Turn on the pulser-receiver and monitor the signal from the oscilloscope.

3. A pulse signal is sent out by HIFU transducer. Once the single pulse propagate across different mediums (e.g. tissue water), portion of the acoustic energy is reflected due to the impedance difference between mediums. The reflecting echo is captured by HIFU transducer and displayed on the oscilloscope. The time of flight between pulse and echo is used to estimate the distance between HIFU transducer and the target.

4. Adjust the position of HIFU transducer using pulse-echo method and move the HIFU focus on to the desired target (LV or RV) by comparing the time-of-flight with the calibrated HIFU focal length.

5. Fix both heart and HIFU transducer and set up HIFU ablation parameters through function generator and FPGA board.

Optical Mapping Procedure

1. Turn off the room light and slowly inject 20 μL di-4-ANEPPS solution into the perfusate. Wait roughly 10 mins for the VSD to load in before taking optical maps.

2. Turn on the LED excitation lights in a flashing mode (100 ms flash) and adjust the focus of the camera and check the signal quality from optical mapping. Adjust the excitation light intensities to the 80 % of the saturation intensity over 2 – 3 s test.

3. Set up the optical mapping parameters (frame rate, duration, triggering, and continuous excitation) and start designed experiment. During experimentation, if the signal-noise ratio is low due to photobleaching and wash out, add another 5 – 10 μ di-4-ANEPPS solution.

4. After finishing all the experiment, remove the heart from the cannula and perform TTC staining and leave it in 10 % formalin solution for further histological staining. Turn off the oxygen. Drain all the circulating solutions and wash the Langendorff system and tissue chamber by perfusing 70 % isopropyl alcohol, distilled water, and air in order.

5. Finally, clean up all the equipment and surgical tools and export data from optical mapping system for further analysis.

Preparation of Tyrode's Solution

A recipe of Tyrode's solution is shown in Table A1. Tyrode's solution for rabbit heart is prepared following a protocol described as following.

Table A1. Recipe of Tyrode's stock solution.

				Stock I	Stock II	
	mM	MW	g/L	25X g/2L	25X g/2L	g/2L
NaCl	128.2	58.44	7.49	374.60		
$CaCl_2 \cdot 2H_2O$	1.3	147.02	0.19	9.56		
KCl	4.7	74.56	0.35	17.52		
$MgCl_2 \cdot 6H_2O$	1.05	203.31	0.21	10.67		
NaH_2PO_4	1.19	137.99	0.16	8.21		
$NaHCO_3$	20	84.01	1.68		84.01	
Glucose	11.1	180.16	2.00			4.0

First, prepare two 2L bottles of Stock I solution and Stock II, which can be stored in the refrigerator. Then put 80 ml of Stock I solution in 2L volumetric flask. Add 1 L of distilled water (otherwise Stock I and Stock II solution will react and precipitate). Then add 80 ml of Stock II solution in the flask. Weight 4 g of glucose (dextrose) and add into the flask. Add distilled water to reach 2 L mark on the flask. Completely dissolve the glucose using magnetic stirrer.

Preparation of Cardioplegia Solution

St. Thomas No.2 solution is used as cardioplegic solution. The cardioplegia needs to be prepared no more than 2 hours before experimentation. The recipe of St. Thomas No.2 is shown as Table A2.

Table A2. Recipe of St. Thomas No.2 cardioplegia solution.

Ingredients	NaCl	KCl	$CaCl_2 \cdot 2H_2O$	$NaHCO_3$	$MgCl_2 \cdot 6H_2O$
mmol/L	100	16	1.2	10	16
g/L	5.85	1.19	0.18	0.84	3.25
Quantity in 2L solutions (g)	11.70	2.38	0.35	1.68	6.50

The procedure of preparing cardioplegic solution is described as following. First weight the ingredients in Table A2 and add into 2L beaker. Then add distilled water to reach the 2L mark on the beaker. Then adjust the osmolarity to 285 ~ 300 mosm/KgH_2O with glucose and osmometer (roughly 4g glucose in 2L solution). Dilute all the ingredients using magnetic stirrer. Transport the solution to the flask, seal the flask, and store in the refrigerator. Before use, adjust the pH value to 7.8 with O_2/CO_2 (95 %/5 %).

TTC Staining Procedure

TTC stock solutions are prepared using the recipe in Table A3. Mix the two different solutions with a volumetric ratio of 2:1. Use Na_2HPO_4 solution to adjust the pH value to be 7.4. First pull 40 ml stock solution in a container and add 400 mg TTC powder. Mix the solution with power completely. Warm up the stock solution before tissue staining process. Put the tissue in the container and keep the container in a warm waterbath for 20 mins. Take out the tissue and take pictures. (Do not leave the tissue in the TTC solution for more than 25 mins. Tissue volume will shrink.)

Table A3. Recipe of stock solutions for TTC staining.

Na_2HPO_4	NaH_2PO_4
1 L – 14.2 g	0.5 L – 6 g